SAIMM

THE SOUTHERN AFRICAN INSTITUTE
OF MINING AND METALLURGY

CAPACI OCCASIO
FOUNDED 1894

VOLUME 126 NO. 8 AUGUST 2026

Creating a **better future**

through the way we do business

Bringing long-term growth and opportunity
for all our stakeholders.

IMPLATS
EXCELLENCE IN PGMs

Typeset and Published by
The Southern African Institute
of Mining and Metallurgy
PostNet Suite #212
Private Bag X31
Saxonwold, 2132
E-mail: journal@saimm.co.za

Printed by
Camera Press, Johannesburg

SAIMM
THE SOUTHERN AFRICAN INSTITUTE OF MINING AND METALLURGY

CAPACI OCCASIO
FOUNDED 1894

VOLUME 126 NO. 8 AUGUST 2026

Contents

Honorary Legal Advisers
M H Attorneys

Auditors
Genesis Chartered Accountants

Secretaries
The Southern African Institute of Mining and Metallurgy
7th Floor, Rosebank Towers, 19 Biermann Avenue,
Rosebank, 2196
PostNet Suite #212, Private Bag X31, Saxonwold, 2132
E-mail: journal@saimm.co.za

ISSN 2225-6253 (print) · ISSN 2411-9717 (online)

Directory of Open Access Journals
INDEXED IN DOAJ

PROFESSIONAL TECHNICAL AND SCIENTIFIC PAPERS

Does geoscience face the same warning signal as metallurgy?

A response to "metallurgy's warning signal" — President's Corner, June 2026

In his June 2026 President's Corner, Gary Lane highlighted a disturbing picture emerging in metallurgical engineering: student numbers in one of South Africa's leading departments have declined by almost 70% over two decades, with fewer than ten metallurgical engineering graduates expected this year. The figures raise an important question about whether metallurgy is facing a problem unique to the profession, or whether it is the first visible warning signal of a broader challenge across the minerals capability ecosystem.

To explore whether similar signals are evident in geoscience, I turned to Associate Professor Grant Bybee, Head of School in the School of Geosciences at the University of the Witwatersrand, who has been tracking these trends semi-quantitatively over the past few years. His analysis provides useful context and suggests that the answer is more nuanced than a simple "yes".

Geoscience is exhibiting some of the same structural pressures as metallurgy, but the shape and severity of those pressures differ.

Where the parallel holds

Like metallurgy, global geoscience enrolments are under pressure. Grant's analysis shows declines across several major mining jurisdictions, including Australia, Canada, the USA and UK, while the recent upturn in exploration associated with critical minerals has not yet been accompanied by a comparable recovery in student numbers. The trend is not universal: Chile, for example, saw substantial growth in its graduate geology pool between 2010 and 2023, while South Africa, as is discussed below, presents a different picture.

There are also broader structural challenges. The extractive industries are not always seen as an attractive career choice by young people, and earth sciences often receive very little attention at school — if they are introduced at all. Some students therefore reach the point of choosing a degree without ever having encountered geology as a career or are swayed by negative perceptions about the profession.

The parallels are clear, but the South African data reveal a more complex picture.

Where geoscience differs

The CREST/DSI analysis, drawing on Higher Education Management Information System (HEMIS) data, tracks honours, master's and doctoral enrolments and graduates from 2010 to 2020, giving us a relatively detailed picture of the changing shape of the South African geoscience pipeline.

The first difference is one of scale. South African geoscience honours enrolments peaked at 343 in 2012 before falling to 225 in 2020 — a decline of roughly one-third. That is significant, but different in scale from the near-70% decline in metallurgical engineering numbers over two decades at the department highlighted by Gary.

The national geoscience data end in 2020, so some caution is necessary in interpreting the current position. More recent experience at some individual geoscience departments suggests undergraduate numbers may be steadying, with honours enrolments and graduations increasing and, in some cases, reaching capacity in 2025/26.

The second difference is the shape of the pipeline. Grant's tracking points to what he describes as an 'inverting pyramid'; a potentially thinning enrolment base with a growing postgraduate apex. Against the decline at honours level, doctoral enrolments increased from 133 to 234 between 2010 and 2020, and PhD graduates increased from 14 to 35.

Grant suggests this pattern is not entirely unexpected. Historically, downturns in commodity cycles and mining activity have been followed, typically after a two-to-three-year lag, by fewer bursaries and employment opportunities. More honours graduates consequently remain at university and progress into master's and later doctoral studies. The South African data show this effect in that master's enrolments increased from 318 in 2013 to 538 in 2016, following the sharp fall in exploration expenditure after the 2012 peak.

The transformation at doctoral level is equally significant. The black South African share of PhD graduates increased from zero in 2010 to 43% in 2020, while the black share of PhD enrolments reached 68%.

In other words, while the geoscience pipeline is under pressure at its base, there is evidence of resilience, growth, and

Journal Comment (continued)

transformation towards its apex. This is where the geoscience and metallurgy stories begin to diverge. The risk in geoscience lies not at doctoral level, which remains healthy and is transforming, but in the potential narrowing of the honours base that feeds both the profession and the future academic workforce.

What this tells us

This comparison raises another important question: how well are we measuring these trends?

We do not currently have this same level of national data across the minerals sector. In South African metallurgy, for example, Grant's review notes that there is no clean national enrolment or graduation series.

We therefore need to understand the health of the entire pipeline, rather than simply count graduates at the end of it.

Globally, geoscience enrolment has historically followed the exploration and commodity cycle, with a lag of two to five years. Non-ferrous exploration expenditure peaked at USD21.5 billion in 2012 before falling sharply, with graduations across the earth-resource professions declining in the years that followed. Exploration expenditure has since partially recovered, but student and graduate numbers have not responded to the same extent.

South Africa, however, does not follow exactly the same clock. Grant's research notes that the local geoscience pipeline has also been shaped by domestic transformation and the contraction of the gold and platinum sectors, rather than simply mirroring global commodity-price cycles.

Perhaps, then, metallurgy is not an exception. It may be the first profession in which the consequences of a broader contraction have become impossible to ignore. Its smaller size, limited cyclical buffering, and position further downstream from the exploration and mining environment may simply make the effects visible sooner.

In that sense, Gary's warning-signal metaphor is particularly apt:

The warning may be system-wide; metallurgy is simply the canary because it is the smallest bird in the mine.

The evidence from geoscience therefore cautions against assuming that every profession within the minerals sector faces the same crisis. Our priority should be to develop the shared measurement capability that allows us to identify where vulnerabilities lie, whether they are cyclical or structural, and where intervention is most urgently needed.

Ultimately, understanding the health of that pipeline means looking beyond whether we have enough geologists, metallurgists, mining engineers, or other specialists today. We need to know whether we are successfully attracting students, educating them, providing meaningful workplace exposure, developing professional capability, retaining experienced practitioners, and transferring knowledge to the next generation.

These early indicators may not look identical across the professions. But if we start looking at them together, we have a much better chance of seeing the bigger picture — and acting before the warning becomes a crisis.

N. Pauls
President, Geological Society of South Africa

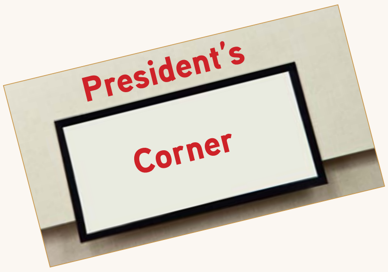

The capability constraint we can no longer ignore: An open letter to CEOs, boards and leaders across industry, academia, and government

To the CEOs, board members and leaders across industry, academia, and government who carry responsibility for the future of our minerals industry.

For the past 12 months, I have had the privilege of serving as President of the Southern African Institute of Mining and Metallurgy (SAIMM). As my term draws to a close, I feel a responsibility to write this open letter to the leaders who make decisions that will shape the capability of our industry for decades to come.

After a year spent listening to mining professionals, executives, regulators, academics, and students, I have reached a clear conclusion: what we commonly describe as a skills shortage has become a much broader capability challenge. This will accelerate over the next decade as our experienced and capable cohort retires. The Mining Qualifications Authority Strategic Plan, tabled in March 2026, recorded 113 hard-to-fill mine manager vacancies and 107 mining engineer vacancies, with insufficient structured experience identified as the principal reason for the latter.

Producing more graduates alone will not solve this problem. What matters is turning talented people into capable practitioners who can make ethical and sound decisions, carry responsibility and apply their knowledge in demanding operating environments. Right now, our biggest challenge is conversion. Soon it will be replenishment.

South Africa has shown what long-term capability investment can achieve. Anglo American's historical development programmes created a capability legacy that remains visible across mining and other industries, locally and internationally. In many of the rooms I enter today, I ask: "who has in some way been touched by an Anglo American development programme?" Generally, 50% of the people in the room put up their hands. Gold Fields is now establishing a ten-year capability-development programme on the West Rand through Siyakha Sonke. These examples are encouraging, but no single company can carry an industry-wide responsibility on its own.

Other mining jurisdictions have already recognised workforce capability as a strategic constraint on future growth. Canada has launched its Mining and Minerals Workforce Alliance. The United States has announced the nationwide PROSPECT initiative, supported by proposed funding of up to USD100 million. Australia has made workforce development a key element of its critical minerals strategy and established the government-funded Mining and Automotive Skills Alliance. South Africa needs a similar level of national focus through our critical mineral's strategy, supported by commitment, broad collaboration, and collective leadership to drive capability delivery and impact.

The engineering pool Is smaller than many realise

Although 88% of full-time candidates passed the 2025 NSC, fewer than 4% would have met the commonly applied minimum threshold of 60% in both mathematics and physical sciences for engineering study—and the proportion satisfying universities' complete admission requirements would be lower.

A recent analysis presented to our Minerals Education Ecosystem South Africa forum (MEESA) suggests that the annual figures equate to approximately 33 engineer-category matriculants per 10,000 public-school NSC writers. ECSA's 2022 report, based on a cross-sectional analysis of 2020 data, recorded 3,239 engineer-category graduates against 725,034 NSC writers—approximately 45 per 10,000 across all engineering disciplines. The figures use different datasets and methodologies and are not directly comparable. Neither represents a tracked cohort, but both point to the same reality: the engineering pool is small.

Mining depends on every engineering discipline while competing with every other engineering-dependent sector and even the financial sector for the same scarce talent. The challenge extends far beyond engineers. It affects technologists, technicians, artisans, supervisors, and operators. If we are serious about building a sustainable industry, we must strengthen the entire workforce pipeline—from the shop floor to specialist and leadership roles.

From student bottleneck to licence-to-operate risk

Thirty-three final-year mining-engineering students will not graduate this year unless they secure the vacation work required by their curriculum. A further 275 third-year students also require workplace exposure. AMMSA has stepped forward to coordinate placements, but this should not depend on annual intervention. It should become part of a permanent industry operating model.

President's Corner (continued)

The statutory-certification pipeline presents an equally serious concern. In 2025, only five Certificates of Competency for mine surveyors were issued while seven experienced surveyors left the industry through retirement or attrition. The Institute of Mine Surveyors of South Africa (IMSSA) reported in August 2026 that 52% of its professional mine surveyors were over the age of 60. Taken together, these figures indicate a significant succession challenge and a growing licence-to-operate risk.

Industry feedback suggests that rock engineering may be constrained in the future, as our highly skilled individuals are being poached internationally and the mine-ventilation talent pipeline is lean.

These are not optional competencies. They sit at the heart of mining's safety and legal framework.

The urgency is reinforced by ECSA's implementation and enforcement of the Identification of Engineering Work Rules gazetted in March 2026. At the same time, Mine Health and Safety Act certification pathways do not align neatly with ECSA registration requirements and our mining industry roles and levels of work. Greater alignment is needed between industry, regulators, and professional bodies if we are to expand supervised development opportunities and strengthen these pathways.

Capability cannot be manufactured on demand

A qualification marks the beginning of professional formation, not the end of it. Experience cannot be developed overnight. Capability is built gradually through practical work, good supervision, exposure to different situations, mentoring, and increasing responsibility. Even with a structured development programme, a student entering their first year today may only reach full professional competence around 2036.

What SAIMM Is building

The SAIMM is working to connect and strengthen many initiatives that already exist across our industry. Approximately 350 volunteers from mining companies, consulting firms, and OEMs currently contribute through council, committees, and various programmes. Through the Minerals Education Ecosystem South Africa forum, the SAIMM Academy, the Continuing Professional Development Committee, the Young Professionals Council and our technical communities, we will work alongside the Institute of Mine Surveyors of South Africa (IMSSA), the Mine Ventilation Society of South Africa (MVSSA), the South African National Institute of Rock Engineering (SANIRE), the Mine Education Trust Fund (METF), Minerals Council South Africa, the Engineering Council of South Africa (ECSA), the Mining Qualifications Authority (MQA), universities, and employers to build an industry-approved graduate capability-development programme.

The objective is straightforward: create a structured pathway that helps graduates develop workplace competence, achieve professional registration and, where relevant, obtain statutory certification, while continuing to grow throughout their careers through professional development.

Put capability on the strategic balance sheet

The mining industry invests heavily in resources, infrastructure, and technology. Yet investment in the people required to design, operate, and improve those systems is often insufficient, particularly when market conditions deteriorate.

South Africa's mineral endowment will only translate into sustainable value if we continue investing in the people who are responsible for turning mineral endowment into production and production into economic growth.

Boards should therefore look beyond annual training budgets and develop a clear view of a properly funded long-term capability strategy. Questions of succession, specialist depth, future demand, development capacity, and capability gaps deserve the same attention as other strategic risks.

My request Is specific

To CEOs and industry leaders: make capability development a strategic priority and an operating responsibility, investing in the full, integrated capability pipeline from education through work-integrated learning. Appoint an accountable executive to join MEESA, establish annual targets for workplace placements and mentoring, share workforce data, support multi-year funding commitments and align workplace skills plans and relevant SLP commitments with the long-term capability pipeline.

To boards: place capability on the strategic risk register and require annual reporting on pipeline conversion, specialist depth, professional registration, statutory certification, and succession, not only on training expenditure.

To government leaders: recognise mining as a pillar of economic growth and critical minerals as an opportunity of national significance and urgently create an enabling environment through aligned policy and incentives. Without deliberate intervention in STEM education, our country's engineering capability will be at risk. Teacher capability, the STEM education pipeline, and industry capability development are interconnected challenges that require coordinated action. Strengthen mathematics and science teaching and improve alignment between education, workplace learning, professional registration,

President's Corner (continued)

statutory certification, and workforce planning.

To the MQA: continue aligning the sector skills plan and SDL-funded grants with a demand-led capability pipeline. Prioritise workplace learning, technical and operator development, graduate programmes, and statutory competency pathways, while measuring placements, completions, certification outcomes, and employment.

To universities and TVET colleges: align curricula with current and future industry needs, identify workplace-learning requirements early, share pipeline and outcome data, and continue working with MEESA, employers, and professional bodies.

The SAIMM is changing its operating model and will invest in addressing this industry challenge as the steward of the professional capability ecosystem. We will continue bringing stakeholders together, helping to coordinate effort, track progress, developing the capability ecosystem, and reporting openly on both successes and gaps. Expect us to engage directly and to ask for measurable commitments around placements, mentoring, data sharing, and sustained support. This will also require an innovative funding model and collective leadership from the industry.

A responsibility that continues

This is my final President's Corner. Its message has been shaped by an extraordinary council, committee chairpersons, and volunteers, as well as leaders from industry, academia, and our secretariat. I remain deeply grateful for their support and commitment.

Although my role will change, my commitment will not. A presidency lasts twelve months. Rebuilding capability takes a generation. Our future depends on developing people who can transform mineral resources into safe, responsible, and sustainable value for society.

The question before us is simple: will we continue to treat capability as somebody else's problem, or will we accept collective responsibility for the people on whom the future of this industry depends?

G.R. Lane
President, SAIMM

A case study on the use of infrared thermography to assess seepage zones in mining operations

by M. Maoyi[1], J.L. van Rooy[1], A. Lotriet[2], R. Bush[3], M.A. Dippenaar[1]

Affiliation:
1 Engineering Geology, Department of Geology, University of Pretoria, South Africa
2 Yellow Technical Services (Pty) Ltd, Johannesburg, South Africa
3 SRK Consulting (Pty) Ltd, Johannesburg, South Africa

Correspondence to:
M. Maoyi

Email:
mampho.maoyi@up.ac.za

Dates:
Received: 26 May. 2025
Revised: 01 Dec. 2025
Accepted: 06 Jun. 2026
Published: Aug. 2026

How to cite:
M. Maoyi, van Rooy J.L., Lotriet A., Bush R., Dippenaar M.A. 2026. A case study on the use of infrared thermography to assess seepage zones in mining operations. *Journal of the Southern African Institute of Mining and Metallurgy*, vol. 126, no. 8, pp. 435 – 446

DOI ID:
https://doi.org/10.17159/2411-9717/3739/2026

ORCiD:
M. Maoyi
https://orcid.org/0000-0003-0737-6548
J.L. van Rooy
https://orcid.org/0000-0003-4708-6991
M.A. Dippenaar
https://orcid.org/0000-0002-6807-1353

Abstract

Effective management of unsaturated fluid flow in open-pit excavations is critical, as mining disturbances like blasting can enhance fracture connectivity, permeability, and water infiltration, thereby compromising slope stability. Thus, this study evaluates infrared thermography as a non-invasive tool for detecting seepage zones in a fractured rock highwall at an open-pit quarry in South Africa. Additionally, field-scale measurements as well as photogrammetry data, are used to gain a better understanding of unsaturated flow behaviour in fractured rock masses. Based on the results of this study, passive infrared thermography established baseline thermal anomalies associated with natural groundwater seepage, revealing distinct cooler surface patterns in highly fractured domains that aligned with geotechnical mapping. Active infrared thermography using controlled injection of cold water into the high wall, enabled real-time thermal monitoring revealing geotechnical domain thermal contrasts on the high wall, confirming preferential channelling along lithological contacts. This non-invasive technique provides valuable insights into the thermal response of highwalls, and highlights the role of fracture networks in controlling fluid movement within geotechnical domains. The findings demonstrate that infrared thermography is a powerful and reliable technique for remotely evaluating areas susceptible to seepage on high walls, based on thermal pattern variations that are imperceptible to the naked eye. This effectiveness as a remote rock monitoring tool for detecting seepage zones in fractured rock masses highlights infrared thermography as a promising strategy for improving hydrogeological risk assessment in mining operations.

Keywords

Unsaturated fracture flow, rock slopes, seepage zone, infrared thermography, photogrammetry

Introduction

Blasting activities in open-pit excavations compromise the structural integrity of jointed rock masses and actively alter their natural permeability (Li et al., 2024). As a result, blasting may increase the connectivity of fracture networks by enlarging existing fractures or creating new fractures, allowing groundwater and rainwater to infiltrate the fractures within the rock mass. For instance, the increased formation of these discontinuities due to blasting raises concerns regarding water flow behaviour and pore water pressures within the slope, which can have implications on slope stability and overall safety (Lu et al., 2024). The effects of blasting on rock mass permeability and groundwater dynamics vary considerably based on several interrelated factors, including the physical and mechanical properties of the rock mass, prevalence and nature of discontinuities, rock density, groundwater presence, type of explosives used, blast design, and intensity of stress waves produced during blasting (Silva et al., 2019; Kaveh Ahangaran et al., 2022; Xu et al., 2022). Collectively, these variables can induce changes in groundwater dynamics, potentially changing established flow patterns in geotechnical domains. The practical implication of these changes is that as mining progresses, it becomes imperative to continually update geotechnical models to reflect evolving rock mass conditions (Abdulai, Sharifzadeh, 2019; Yeh et al., 2021). Consequently, a thorough understanding of groundwater flow in fractured rock mass is essential, particularly in complex geological systems where discontinuities act as primary hydraulic pathways.

Previous studies have identified challenges in understanding the implications of excavations on rock mass behaviour, groundwater dynamics and flow patterns within these fractured systems (Li et al., 2014; Zhao et al., 2017). For example, Li et al. (2014) investigated groundwater trends in an open-pit mining area using a generalised large well method alongside a confined-unconfined flow model. Their study demonstrated the impacts of mining on local groundwater dynamics, which were crucial for environmental management. Similarly, Zhao et al. (2017) proposed a comprehensive methodology that integrated hydrological modelling with field data to assess the influence of open-pit mining on groundwater systems. Nonetheless, the accuracy of such models is often compromised by assumptions related to geological, hydrological, and hydraulic properties, where deviations from real-geological conditions can substantially affect the confidence interval of the data and reliability of the findings. Despite these advances, developing a representative model that accurately reflects fracture parameters still remains a challenge, as many parameters must be extrapolated or inferred due to the complex nature of geological and induced processes that create discontinuities of varying scales and orientations (Huang et al., 2019). These complexities result in fractured media exhibiting pronounced spatial variability and anisotropy, leading to intricate fracture networks. Therefore, effective rock mass characterisation must consider various influential factors that include lithology, structural features such as faults and discontinuities, and conditions such as fracture frequency and weathering (Zimmerman, Paluszny, 2023). These parameters play a crucial role in determining the rock mass ratings, which can be further categorised into distinct geotechnical domains for stability assessments within rock engineering and rock mechanics applications (Bieniawski, 1973; Barton et al.,1974; Bieniawski, 1989; Laubscher, 1990; Zhang et al., 2019).

For researchers and industry consultants, a thorough understanding of fluid movement is vital for assessing the connectivity of fractures, a key component in rock monitoring, especially amidst ongoing geological changes in mining environments (Li et al., 2024). Currently, a multifaceted approach is commonly employed to characterise fluid flow behaviours in fractured media. This encompasses aquifer characterisation, analysis of recharge areas, and monitoring of water levels in open pit environments (Liu et al., 2021). While these techniques yield valuable insights, there is often a predominance of reliance on quantitative values and assumptions regarding flow patterns in the absence of direct observations of flow path geometries within the rock mass. This limitation is particularly acute in unsaturated conditions, where an upscaling framework is needed to better address gaps in understanding fluid flow in fractured rock masses (Zhang et al., 2021). The primary challenge of managing unsaturated fluid flow within open-pit mining environments lies not merely in identifying major discontinuity sets with similar orientations, but this is also related to determining which of these sets are hydraulically active within a specific geotechnical domain. This is essential for mitigating issues related to rock stability, particularly in situations exacerbated by blasting and periods of heavy rainfall when water can flow through major discontinuity planes associated with potential slope failures. Therefore, developing a robust monitoring strategy is increasingly vital to reduce rock slope risks.

To address the aforementioned challenges, the use of infrared thermography offers a promising avenue in studying the identification of groundwater zones and regions susceptible to seepage in rock mass (Meola, 2012; Sass et al., 2023). This non-invasive imaging technique captures and processes thermal information through thermal images by detecting infrared radiation emitted by objects and converting the image into temperature values above absolute zero (Mineo, Pappalardo, 2021). For instance, Wu et al. (2005) assessed the integrity of rock masses in the context of shotcrete slopes, highlighting the technique's capability to identify eroded voids behind shotcrete applications. Similarly, Teza et al. (2012) utilised infrared thermography to remotely identify weaknesses in rock cliffs, showcasing its usefulness in characterising geotechnical properties by detecting features such as voids and material inhomogeneities. In a further step towards enhancing hazard detection, Gigli et al. (2014) proposed an integrated methodology that combines terrestrial laser scanning with terrestrial infrared thermography for monitoring stability and detecting instabilities on slopes. Their findings illustrate that thermal images collected during assessments can reveal unstable rock masses, highlighting the importance of employing advanced techniques in geological surveys to improve risk management. However, a notable gap exists in the literature surrounding the application of infrared thermography in hydrogeology, rock engineering, and rock mechanics.

According to the authors' knowledge, the work by Rosenbom and Jakobsen (2005) remains the only study linking infrared thermography with fracture analysis and groundwater flow in chalk formations in Denmark. Their experimental framework involved the injection of cold water into a fractured chalk high wall in a quarry, aimed at assessing hydraulic connectivity. However, the absence of a robust baseline and reliance on qualitative thermal image interpretation limited the study's conclusions. Thus, this study builds on the groundwork established by Rosenbom and Jakobsen (2005) and expands the application of infrared thermography to South African geological formations. Specifically, it focuses on the quartzitic sandstones of the Daspoort Formation of the Transvaal Supergroup. Field experiments involving passive monitoring under ambient conditions and active cold-water injection are conducted on an exposed quarry high wall. The resulting thermal imagery is analysed using complementary qualitative (visual anomaly detection) and quantitative (temperature differential) methods, with interpretations integrated against detailed geotechnical characterisation of the rock mass to elucidate seepage zones in fractured rock environments.

Aims and objectives

The aim of this study is to evaluate the effectiveness of infrared thermography as a non-invasive, remote monitoring tool for detecting seepage zones in fractured rock masses within mining operations. Through a field-based case study at a quarry site, the research seeks to demonstrate the technique's potential as a practical strategy for enhancing the understanding of unsaturated fluid flow behaviour in fractured rock environments.

The objectives of this study are as follows:

- Conduct passive and active infrared thermography (IRT) experiments on the quarry high wall to capture thermal signatures and anomalies indicative of unsaturated flow and seepage zones.
- Analyse thermographic data qualitatively and quantitatively to delineate areas susceptible to seepage.
- To integrate IRT findings with geotechnical characterisation of the high wall, assessing the overall effectiveness and limitations of IRT for non-invasive seepage detection in fractured rock.

Geological setting

This study was conducted at a quarry site in South Africa. The bedrock in this region forms part of the sedimentary rocks of the Daspoort Formation, Transvaal Supergroup (Figure 1). The open pit quarry lies in competent quartzitic sandstones of the late Archaean to early Proterozoic (2.65 – 2.05 Ga), with diabase sills and dykes intruding along weak discontinuities in the quartzitic sandstone (Eriksson et al., 2006). The later intrusion of the Bushveld Igneous Complex (2.05 Ga) resulted in contact metamorphism, producing quartzites from clastic protoliths (Eriksson, Reckzo, 1995). Weathering of the diabase occurs along the distinct contact zones directly above and below the sill. The Bushveld deformational event later affected the Transvaal Supergroup succession, which resulted in the development of folds and faults with a general northwest-southeast-to-north vergence (Eriksson et al., 2006).

The pit layout typically features high wall faces with an overall slope angle of 58°. Planar failure occurred at the contact between quartzite and diabase on the southwestern high wall of the quarry, as illustrated in Figure 2. During the quarrying process, the removal of overburden led to stress relief, causing the overlying quartzite to displace along the contact with the diabase. This displacement resulted in the formation of tension cracks at the crest of the open pit and intense rainfall during summer resulted in increased water ingress into the tension cracks. Due to the impermeable nature of the diabase, interflow occurred along the contact between the diabase and quartzite, ultimately appearing in the pit face. This probably caused a sudden rise in pore pressure and a corresponding decrease in effective stress, leading to a reduction in shear strength and the occurrence of localised planar slope failure.

Methodology

Study site - southwestern high wall

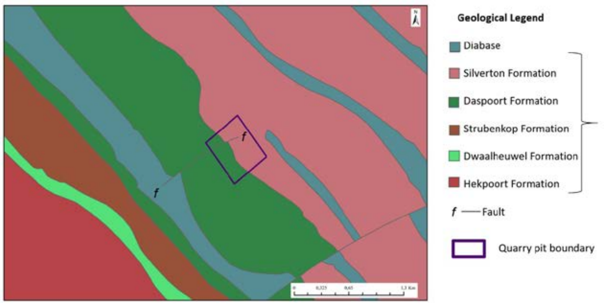

Figure 1—Geological map of the 2528 Pretoria Group Transvaal Supergroup, South Africa. Adapted from 1:250 000 Geological Map of 2528 Pretoria, 1978 (Council for Geoscience South Africa, 2020)

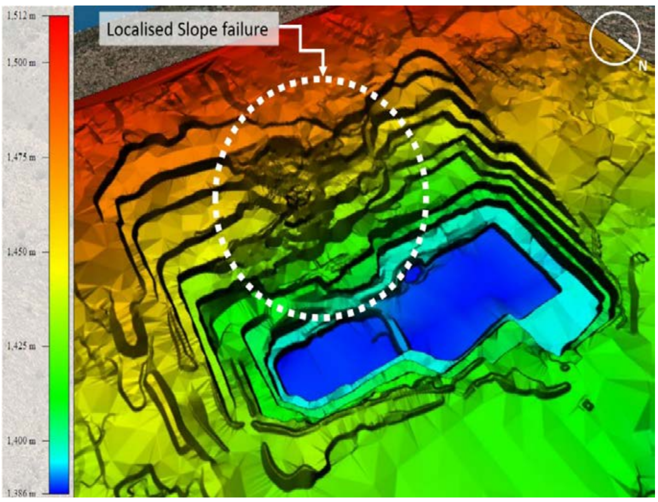

Figure 2—Digital terrain model of the quarry pit (~14 hectares)

The experimental site selected for infrared thermography monitoring is situated on the southwestern high wall of the open-pit mine, at the lowest accessible bench (Bench 1), where persistent groundwater seepage has been observed. This location was chosen due to the visible emergence of groundwater at the contact between highly weathered diabase and the quartzitic sandstone of the Daspoort Formation (Figure 3). The same section has previously experienced a localised slope failure, highlighting the significance of discontinuities in facilitating preferential flow pathways under both unsaturated and variably saturated conditions.

The selected Bench 1 extends laterally for approximately 60 m and has an average height of 10 m. Furthermore, a vertical uncased 18 m borehole was drilled approximately 3 m behind the high wall crest. It was positioned directly above the natural seepage zone and intersected the weathered diabase layer (refer to the cross-section, Figure 4). This borehole served as the primary injection point for controlled water flow tests, with the static water level measured at approximately 5 m below the collar. This section of the high wall was subdivided into two distinct geotechnical domains, designated as Domain A and Domain B, as illustrated in Figure 4. The chosen intermediate scale for the field test is optimal: sufficiently large to encompass spatial variability in seepage behaviour, yet compact enough to permit detailed, high-resolution monitoring using infrared thermography together with complementary field measurements.

Geotechnical mapping

Prior to the field experiments, an integrated site investigation was conducted to assess the geotechnical properties of the selected high wall. The characterisation combined field window mapping

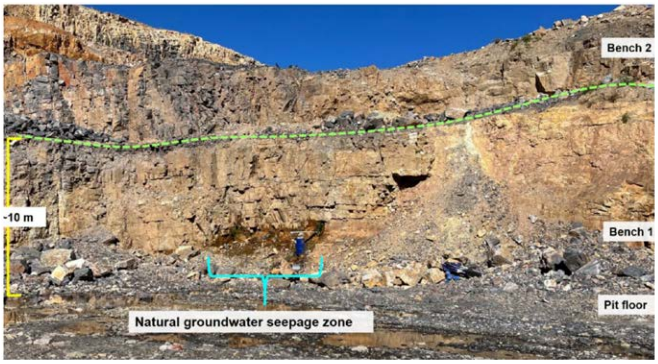

Figure 3—High wall study area (Bench 1) at ~1,400 m elevation for infrared seepage monitoring experiments

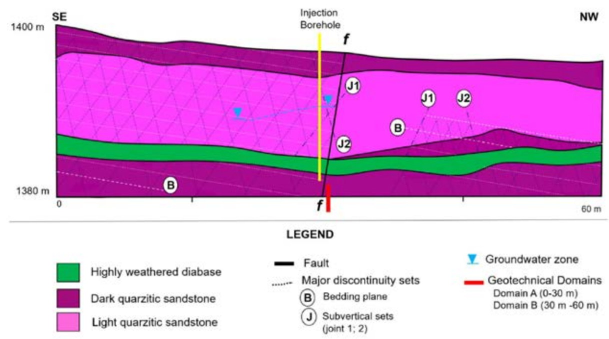

Figure 4—Geological cross-section of the southwestern high wall (Bench 1), showing geotechnical Domains A and B

with photogrammetry to improve the accuracy and detail of the geotechnical mapping. The mapping methodology followed the recommendations of the International Society for Rock Mechanics (ISRM, 1978), and further elaborated upon by Zangerl et al. (2022). This preliminary investigation provided the essential foundation for a detailed analysis of the lithological characteristics, structural features, and discontinuity orientations of the rock mass. Furthermore, key geotechnical features such as discontinuity sets and their persistence within the high wall, were also digitally extracted using Hive Map™ and 3GSM Shape Metrix™ (Rocscience®).

Thermal monitoring of the high wall

To identify areas on the southwestern high wall that could be susceptible to seepage and were not easily visible to the naked eye, surface temperature variations were monitored using the FLIR T1020® thermal camera. The camera was configured for time-lapse image acquisition, allowing continuous tracking of surface temperature distributions during experiments (Vollmer, Möllmann, 2018).

It is important to acknowledge that infrared thermography measurements are sensitive to several environmental and instrumental factors. This includes ambient conditions such as wind, precipitation, solar radiation, and camera calibration (Vollmer, Möllmann, 2018). These factors can introduce variability in surface temperature readings and affect measurement accuracy. Furthermore, accurate interpretation of thermal contrasts requires consideration of both meteorological conditions and the thermal properties of the rock mass, particularly surface emissivity and the presence of subsurface anomalies that may manifest as surface temperature differences. These parameters are critical, as they influence the transmission and detection of infrared radiation (Usamentiaga et al., 2014).

To minimise such effects, the camera was calibrated prior to data collection and experimental controls were implemented to improve the reliability of the temperature measurements (see Table 1). To complement infrared measurements and enable correction for atmospheric effects, ambient air temperature and relative humidity were continuously recorded using a pocket thermohygrometer.

Thermal images were acquired along the area of interest on Bench 1 of the southwestern high wall to ensure comprehensive spatial coverage, as depicted in the experimental setup (Figure 5). Both passive and active thermography techniques were employed to detect thermal anomalies associated with seepage zones by capturing emitted thermal radiation within the camera's field of view.

Passive thermography was conducted first to establish baseline surface temperature distributions under natural environmental conditions (Figure 5). This non-invasive technique relies on the detection of emitted thermal infrared radiation from the rock surface, which is directly related to its temperature (Vollmer, Möllmann, 2018). Thermal images were collected along the high wall to capture spatial variations in surface temperature for subsequent analysis.

To enhance detection sensitivity and delineate subsurface flow anomalies more effectively, active infrared thermography (IRT) was employed by applying a controlled thermal stimulus. Cold water (≈3 °C) was pumped into an uncased borehole to simulate seepage and induce a pronounced temperature contrast at the exposed rock surface relative to ambient conditions.

This setup included a water tanker as the cold-water source, fitted with a DN40 FlowVis® flow meter providing real-time flow rate monitoring, a non-return valve to prevent backflow, and a compatible discharge pipe for controlled delivery. The discharge pipe was inserted directly into the uncased injection borehole (Figure 5).

The field test started at 12:28 SAST by opening the control valve, pumping a total volume of 7000 L of water at a constant flow rate of 5 $m^3 h^{-1}$. Concurrent active IRT surveys monitored real-time surface temperature changes on the southwestern high wall until 14:00 SAST. This monitoring period permitted establishment of quasi-steady-state flow conditions in the fractured rock mass and development of a detectable thermal response at the exposed high wall face.

Post-processing of acquired thermal images

The captured thermal images were then transferred to FLIR Thermal Studio® for post-processing carried out in two steps. In the first step, qualitative analysis of the overall experimental data was performed, focusing on the visual observations of the entire high wall. This assessment utilised a colour-scaled palette thermogram, where each colour corresponds to a specific temperature measurement (Mineo et al., 2015). Therefore, target points were set within the thermograms, corresponding to temperature ranges based on the environmental conditions. This adjustment is necessary to accurately identify areas on the high wall that exhibited signs of moisture.

Following the qualitative assessment, the second step involved exporting the thermographic data for a more detailed quantitative analysis. Regions of interest (ROI) were defined to isolate geotechnical domains with differential surface temperatures. Temporal analysis tracked temperature changes throughout the acquisition sequence. Subsequently, minimum temperature values

Table 1
Transient field parameters

Parameters	
Emissivity	0.95
Ambient temperature	33 °C
Season in Southern Hemisphere	Autumn (April)
Camera distance from target point	~25 m
Camera resolution	1024x768
Camera lens	FOL21

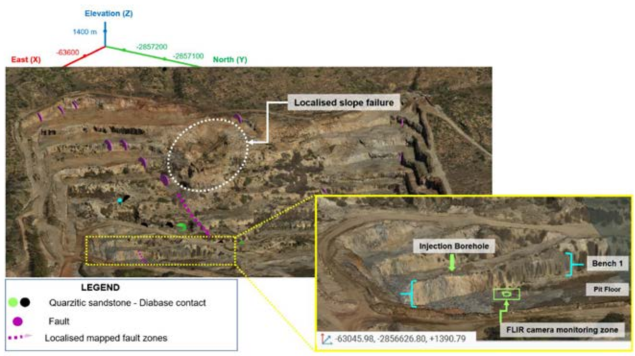

Figure 5—Experimental set-up

were extracted from each ROI to enhance detection of seepage-related thermal contrasts and improve anomaly identification. The final outputs were time-series temperature profiles for each ROI, focusing on key geotechnical subdomains. All processing parameters (e.g., emissivity, distance, palette) were kept constant to ensure comparability across datasets.

Results and analysis

Geotechnical domains within high wall

The high wall analysed in this study predominantly consists of quartzitic sandstones, which have been systematically classified into two distinct geotechnical domains.

Geotechnical Domain A (Figure 6a) features a 30 m wide window, primarily composed of slightly weathered, very hard quartzitic sandstone, which accounts for approximately 98% of the material. The remaining 2% is represented by weak, highly fractured soft rock, specifically weathered diabase, situated at the top of the slope. The photogrammetric model (Figure 6a) illustrates that this domain is characterised by rock mass exhibiting minimal discontinuities. Additionally, bedding planes and sub-vertical joints are prominent throughout the area, particularly within the lower 3 m of the pit. These discontinuities extend across a 20 m span but become less frequent in the upper 6 m of the high wall. Notably,

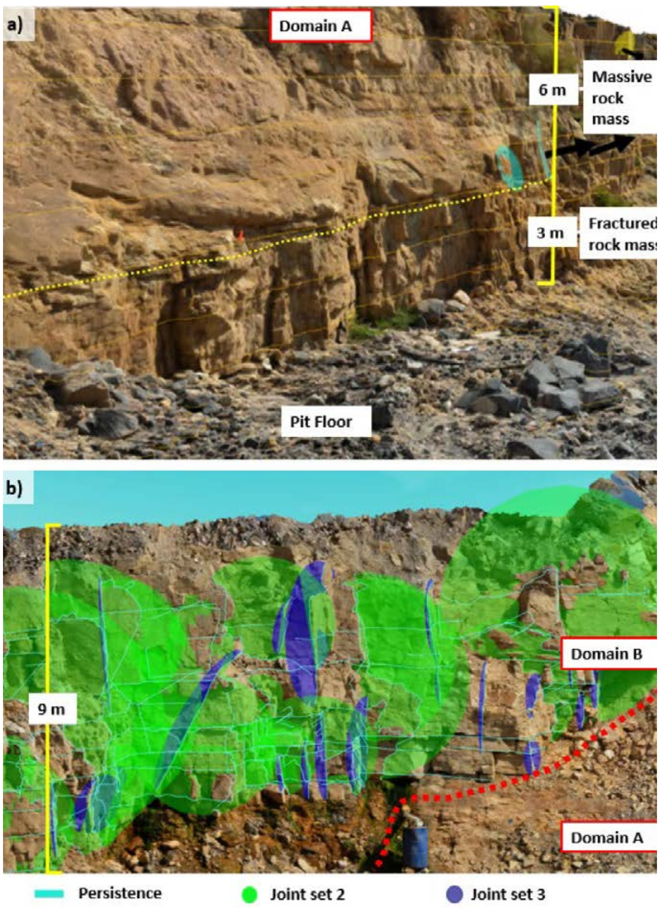

Figure 6—3D South western high wall photogrammetric model (a) geotechnical Domain A showing upper massive rock mass and bottom fractured rock mass - Shape Metrix™ (b) Domain B with the sub-vertical discontinuity sets and trace length for the persistence within the rock mass - Hive Map™

within the remaining 10 m width of this geotechnical domain, no discontinuities were observed, and the groundwater conditions in the rock mass are reported to be dry.

Geotechnical Domain B comprises a 30 m wide window featuring a 9 m high bench, characterised by a pronounced blocky nature throughout the mapped area (Figure 6b). Blasting operations have markedly intensified this blockiness by artificially fracturing existing discontinuities within the rock mass. This domain consists of approximately 95% slightly weathered hard quartzitic sandstone and 5% weathered diabase. The weathered diabase layer, which is about 300 mm thick, runs parallel to the bedding plane of the quartzitic sandstone and is distinguished by a slightly undulating surface and a yellowish-brown colour, indicative of highly fractured medium to soft rock. Notably, this area is the only location in the pit where continuous groundwater flow with estimated flow rates of 9 L/s is observed, occurring at the contact between the weathered diabase and quartzite. This consistent flow leads to the saturation of the area, creating a natural groundwater seepage zone as shown in Figure 7.

A distinct transition occurs between Domain A and Domain B (Figure 8), marked by the minimal discontinuities of Domain A, which shift abruptly to the blocky characteristics of Domain B, delineated by a sub-vertical fault. Analysis of the 3D photogrammetric model confirmed that the discontinuity sets prevalent in Domain B do not persist to Domain A. Despite marked differences in fracture frequency, with Domain A showing much lower discontinuity density than the highly fractured Domain B, both domains are characterised by the same three major discontinuity sets. These comprise bedding planes and two sub-vertical joint sets (Table 2).

Initial insights from passive thermography

During passive thermography monitoring, the high wall at Bench 1 showed distinct thermal signatures. The ambient air temperature was recorded at 33 °C, whereas the rock surface temperature in both geotechnical Domains A and B reached approximately 56 °C. This thermal contrast is consistent with solar heating of the high wall, which absorbs visible and infrared radiation (Vollmer, Möllmann, 2018). However, the natural groundwater seepage zone in geotechnical Domain B has a cooler thermal signature of approximately 21 °C, clearly distinguishable from the warmer (56 °C) surrounding drier rock mass. (Figure 9). These observations

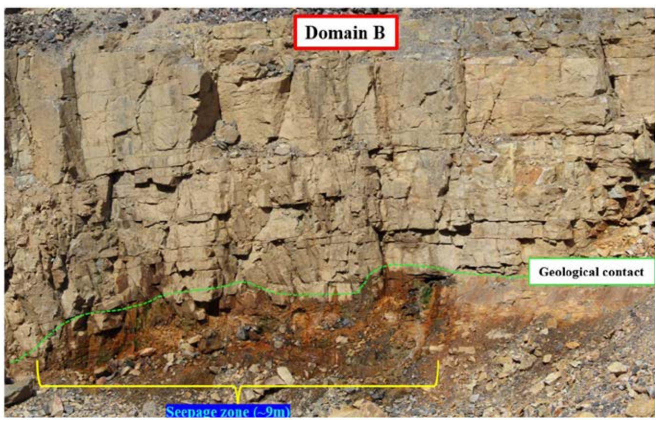

Figure 7—Geological contact between quartzitic sandstone (upper layer) and weathered diabase (lower layer), illustrating groundwater seepage zone

highlight the influence of environmental conditions on surface temperature distributions in open-pit high walls.

Active thermography for delineating seepage zones

During active thermography surveys of the high wall at Bench 1, introducing cold water (~3 °C) into a specific borehole acted as the main external thermal input to create measurable surface temperature differences. This controlled cooling resulted in distinct and spatially variable thermal anomalies across geotechnical Domain A and B.

In geotechnical Domain A (Figure 8), no detectable temperature contrasts or moisture related thermal signatures were observed during monitoring. Although the injection borehole was situated above the natural groundwater zone where downward or lateral spreading might be expected in this domain, the absence of cooling signatures suggests water migration was minimal or redirected. Moreover, the lack of thermal signatures in Domain A is likely due to its massive rock mass conditions and poorly developed hydraulic fracture network.

In contrast, spatially localised cooling was recorded along the exposed face in geotechnical Domain B, confirming rapid migration of the 3 °C injected water. To enable detailed analysis of the thermal response, Domain B was subdivided into two equal subdomains, B1 and B2. Each subdomain had a window width of 15 m and a bench height of 9 m (Figure 9). This subdivision facilitated closer examination of spatial variability in cooling patterns across the high wall.

Within Subdomain B1, qualitative thermal images did not reveal any additional thermal anomalies beyond the established natural groundwater temperature of approximately 21 °C (Figure 10). In contrast, quantitative time-series temperature measurements for this subdomain showed gradual declines and temporal fluctuations during the experiment (Figure 11). These quantitative trends indicate sustained migration of the cooler injected fluid within the high wall, even in the absence of prominent qualitative signatures.

Approximately 40 minutes into the field experiment, a new seepage zone emerged on the high wall face in Subdomain B2. Initially, no visible flow paths were present, and thermal contrast

Table 2

Discontinuity mapping data relating to major joint sets (average values)

Joint set	1	2	3	
Type	Bedding plane	Joint	Joint	Contact
Dip/dip direction	14°/040°	86°/322°	84°/054°	
Micro roughness	Rough undulating	Rough undulating	Smooth planar	Slickenside
Macro roughness	Straight	Slight undulation	Curved	
Infilling	Stained; sandy clay infill	Stained	Stained	Sandy silt
Alteration	Wall = rock	Wall = rock	Wall = rock	Wall < rock
Mean spacing	0.8 m	0.6 m	0.45 m	-
Aperture	3 mm	4 mm	2 mm	-
Minimum persistence	0.61 m	0.35	0.62	
Maximum persistence	16.34	6.41	3.66	> 20 m
Lithology	Quartzite	Quartzite	Quartzite	Quartzitic contact - highly weathered residual diabase

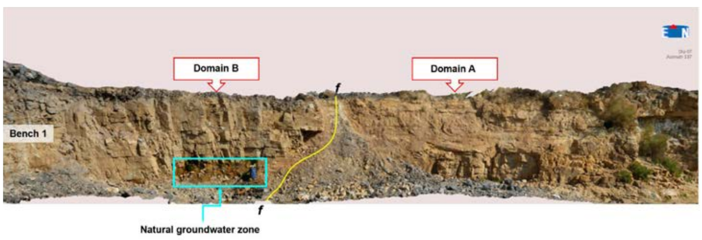

Figure 8—Photogrammetric model of Bench 1 illustrating the spatial transition from geotechnical Domain A to Domain B, delineated by a fault (Hive Map™).

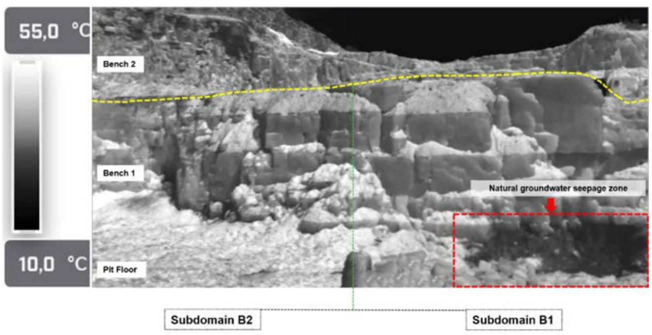

Figure 9—Thermogram of geotechnical Domain B before active thermography field experiment subdivided into Subdomain B1 and Subdomain B2

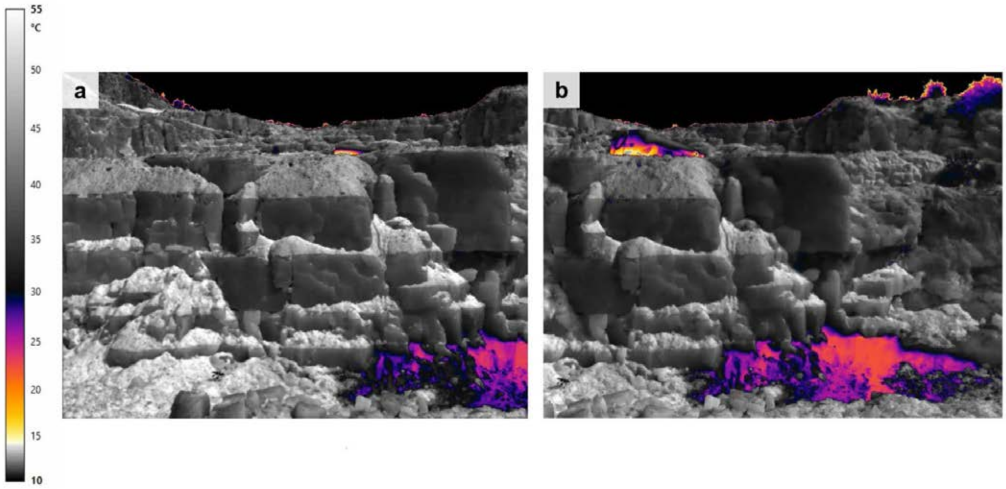

Figure 10—Thermograms of Subdomain B1 illustrating thermal characteristics at (a) the beginning and (b) the end of the experiment (with an adjusted viewing point for the subdomain)

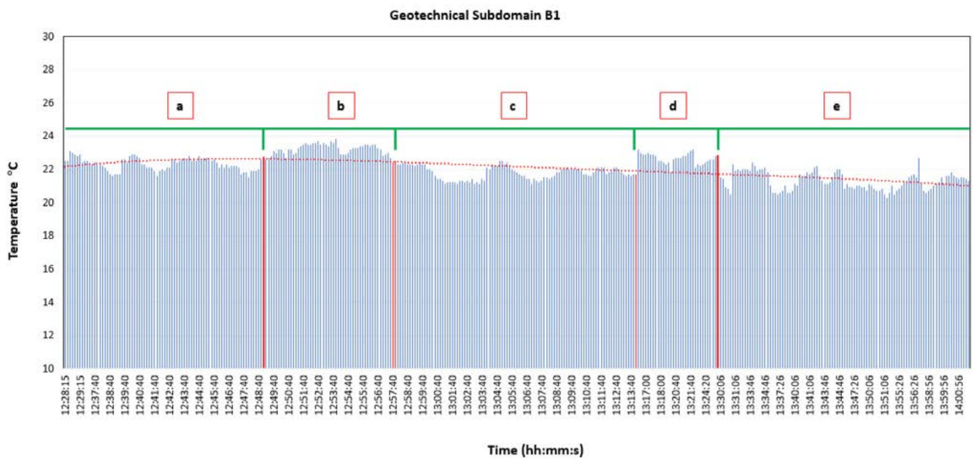

Figure 11—Subdomain B1 temperature versus time graph illustrating the temperature changes recorded at the beginning and end of the experiment

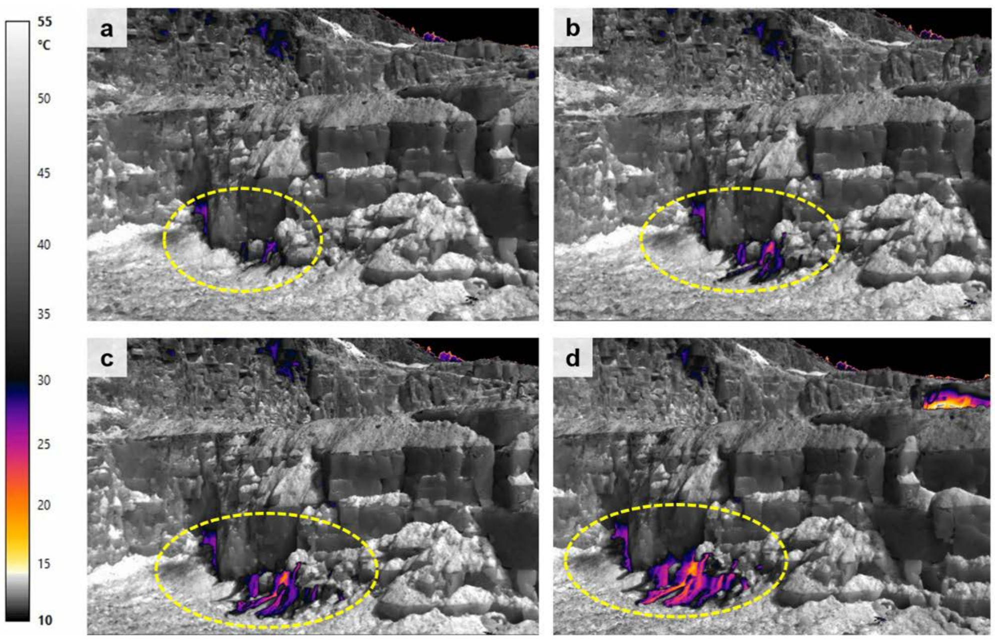

Figure 12—Thermograms of Subdomain B2 illustrating thermal characteristics at the beginning and conclusion of field test

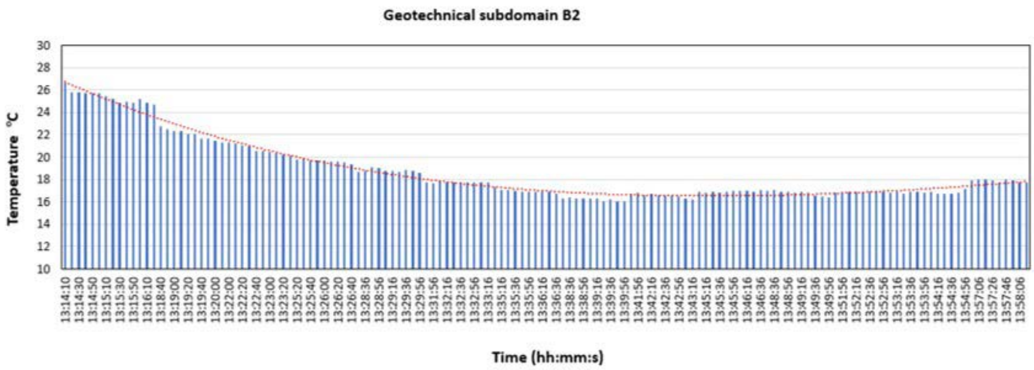

Figure 13—Subdomain B2 temperature versus time graph illustrating the temperature changes recorded at the beginning and end of the experiment

was minimal (Figure 12a). As the experiment continued, repeated wetting cycles during the injection test progressively expanded the wetting front on the rock surface, enabling the detection of subsurface flow through infrared radiation signatures (Figure 12b). The thermal images revealed the formation of new seepage zone governed by preferential flow paths that followed interconnected fracture networks and were oriented parallel or subparallel to bedding planes (Figures 12c – d). This new seepage outflow point coincided with the contact between quartzitic sandstone and weathered diabase, mirroring the location of the pre-existing natural groundwater seepage zone. In addition to this, quantitative analysis of surface temperatures in the Subdomain B2 seepage zone showed a progressive decline in minimum surface temperature throughout the monitoring period (Figure 13). This sustained decrease reflects the ongoing advection of cooler injected water through hydraulically active fractures.

Discussion

The primary aim of this study was to evaluate the capability of passive and active infrared thermography (IRT) as a non-invasive tool for visualising subsurface heterogeneity and preferential seepage patterns in unsaturated fractured rock masses within an open-pit high wall. The fundamental research contribution lies in providing direct, empirical evidence of flow localisation, time-dependent activation, and advective cooling along hydraulically active discontinuities. By combining ambient thermal monitoring with controlled thermal stimulation (cold-water injection), this approach successfully detected both natural and induced thermal anomalies. These results confirm the effectiveness of infrared thermography (IRT) for identifying seepage zones and provide valuable insights into flow behaviour in fractured rock environments.

Interpretation of passive and active thermal signatures

Passive infrared thermography (IRT) proved to be a reliable method for establishing baseline conditions and detecting natural thermal anomalies associated with groundwater seepage. Under ambient temperatures, the most pronounced thermal signatures appeared in Domain B, where water seepage from the high wall produced cooler surface patterns that matched geotechnical window mapping results (as shown Figure 9). The clear thermal contrast between moist (cooler) groundwater zones and adjacent dry rock highlights the effectiveness of passive IRT as an efficient, non-invasive tool for mapping seepage zones. These findings are consistent with those of Gigli et al. (2014), who observed that moisture zones exhibit distinct, cooler thermal signatures than drier areas on target objects during monitoring, due to evaporative cooling.

To simulate seepage infiltration in fractured rock mass, active infrared thermography was implemented by pumping cold water (~3 °C) into the borehole. This method enabled real-time monitoring of active flow pathways by detecting thermal contrasts between the water and the high wall. Geotechnical domains within the monitored high wall exhibited distinct preferential flow patterns determined by the extent of fracturing and connectivity of discontinuities (refer to Figure 8). In Domain A, where the rock is predominantly massive with low secondary permeability, no thermal contrasts were observed. These thermal results indicate that conditions within this domain were not conducive to rapid fracture controlled seepage. Thus, any minor infiltration that may have occurred was likely limited to matrix flow, progressing at rates insufficient to produce observable cooling anomalies during the monitoring period. In contrast, Domain B, featuring higher fracture density and well-interconnected discontinuities, promoted rapid preferential channelling of water within the high wall. This resulted in markedly stronger, more persistent, and spatially extensive thermal anomalies, reflecting enhanced advective cooling along dominant flow paths.

Furthermore, Domain B was subdivided into Subdomains B1 and B2 for a detailed thermal analysis. In Subdomain B1 (Figure 10), qualitative thermograms effectively identified the natural groundwater discharge zone but were unable to detect additional seepage areas, reflecting the inherent limitations of static thermal imaging under low thermal-contrast conditions. To overcome this, complementary quantitative time-series monitoring was employed, revealing cooling trends indicating subsurface connectivity within this subdomain. In contrast, thermal imaging in Subdomain B2 (Figure 12) revealed the emergence of a new seepage zone. Quantitative surface-temperature analysis further demonstrated a progressive decline in minimum temperatures throughout the monitoring period. Subsequently, reflecting ongoing advection of cooler water flow through hydraulically active fractures within the high wall.

Differences in thermal signatures between Subdomains B1 and B2 highlight the complementary benefits of combining qualitative and quantitative thermal results to improve the interpretation of active IRT data. Qualitative evaluation of thermal images reveals how water moves and localises along preferential flow paths within fractured rock, providing direct insight into fracture flow heterogeneity. This approach captures the initial formation and progressive expansion of cooling anomalies directly linked to active seepage zones, thereby offering important contextual information on flow localisation within the fractured rock mass. This represents a meaningful advance for unsaturated fracture flow as monitoring techniques are often inferred indirectly from geological knowledge and assumed connectivity patterns. While visual interpretation of thermal images may miss early signs of water infiltration, quantitative analysis excels at detecting the onset and precise timing of advective cooling in high walls. It offers superior sensitivity to subtle temperature drops that are frequently masked by environmental noise or too faint to discern visually, especially during the initial phases of water infiltration. Combining both qualitative and quantitative approaches prove valuable under changing environmental conditions, such as unsaturated flow into fractured rock mass.

Flow behaviour in fractured high wall

The observed behaviour provides important insights into unsaturated fracture flow. Subsurface heterogeneity arises from variations in fracture density, connectivity, aperture, roughness, and lithological contacts. These factors govern the development of preferential pathways under transient conditions. In Domain A, massive rock restricts flow to matrix-dominated processes and supports dual domain models that predict limited fracture matrix interaction in low permeability zones. In contrast, Domain B demonstrates rapid channelled advective cooling and delayed secondary seepage, which illustrates flow focusing along connected discontinuities. These findings align with established conceptual models of unsaturated flow in fractured rock. Dual-permeability frameworks describe fractures as the main conduits for rapid preferential flow, while the rock matrix allows for slower storage and imbibition, e.g., Gerke and Van Genuchten (1993) and Berkowitz (2002). This study extends these concepts by providing in situ empirical evidence of preferential pathway in fractured rock mass using infrared thermography.

Infrared thermography (IRT) revealed two distinct seepage zones on the high wall face. The first, a natural seepage zone, was detected during initial passive IRT surveys (Subdomain B1), while the secondary seepage zone emerged in Subdomain B2 during active IRT monitoring. Both seepage zones were located at the contact between quartzitic sandstone and weathered diabase, demonstrating the role of such lithological contacts as high-transmissivity horizons. In addition to this, variability in fracture aperture further controls where seepage zones develop, with larger apertures promoting focused channelling and higher flow rates, while narrower segments and asperities cause capillary bridges, local bottlenecks, and tortuous, pressure-dependent pathways (Berkowitz, 2002). At these contact zones, geometric alignment, bedding plane continuity, and connected fracture networks govern preferential flow and enable rapid pathway activation (Xu et al., 2021; Zimmerman, Paulsny, 2023).

Furthermore, active infrared thermography experiments indicate that seepage in this fractured rock mass is highly sensitive to transient hydraulic gradients. This sensitivity is evidenced by the delayed appearance of a secondary seepage zone, which emerged ~40 minutes after field tests began. The time-dependent delay suggests that fluid flow within the fractured rock mass at the study site is primarily controlled by discontinuity characteristics such as surface roughness, asperity distribution, and thin infills (refer to Table 2). As a result, these characteristics govern fluid pathways, transmissivity, and preferential channelling as highlighted in various studies (Chen et al., 2017; Luo et al., 2022). Moreover, fracture topography also influences seepage migration, as surface roughness may either impede or enhance flow depending on the configuration of discontinuities (Dippenaar, Van Rooy, 2016). Ultimately, seepage zones commonly form along bedding-plane parallel or sub-parallel pathways, shaped by surface morphology and variable wetting resistance under unsaturated conditions.

These observations highlight the limitations of relying on visual inspections or traditional methodologies for assessing fluid flow in fractured rock masses. As highlighted in this study, the principal challenge in managing unsaturated fluid flow in rock engineering is not merely identifying major discontinuity sets, but determining which of these are hydraulically active within specific geotechnical zones. This challenge is especially critical in open-pit environments, where unsaturated fracture flow during infiltration events can cause rapid pore pressure increases along hydraulically active discontinuities. This process reduces effective stress and shear strength, thereby promoting rock slope instability (Li et al., 2024).

Thus, the present study was carried out at a site with a known history of infiltration-induced slope failure, providing key context for unsaturated flow behaviour in fractured high walls. The application of infrared thermography (IRT) as a non-invasive monitoring tool demonstrated its practical utility for identifying zones of preferential seepage. By detecting thermal anomalies indicative of such zones, IRT enabled spatial delineation of areas most susceptible to seepage within the fractured rock mass. This technique offers an advantage over conventional methods, which generally do not provide direct evidence of active flow paths.

Limitations

Despite the proven effectiveness of both passive and active infrared thermography (IRT) in detecting seepage zones within fractured rock masses, several important limitations remain. While the use of a controlled setup, a single quarry bench with one injection source helped reduce experimental variables and enabled clear interpretation of thermal signals, it also restricted the scale of the investigation. Consequently, the findings serve primarily as valuable initial guidance for IRT based seepage visualisation studies. In addition, IRT is highly sensitive to environmental influences such as solar radiation, weather conditions, viewing angles, and variations in rock emissivity. These factors can easily obscure the subtle thermal contrasts required for reliable seepage detection. A further limitation lies in the need for IRT processing techniques. Translating two dimensional thermal images need to be inferred to complex fracture flow paths and subsurface seepage areas in high wall demand advanced post-processing methods. This step not only requires specialised expertise but also entails significant computational resources.

Conclusion

This study has demonstrated infrared thermography (IRT) as a promising, non-invasive method for detecting seepage zones in fractured rock mass. This was achieved by integrating geotechnical characterisation of the quartzitic sandstone intruded by diabase with temperature distribution analysis along the southwestern highwall of the quarry.

Passive IRT under ambient conditions revealed distinct thermal signatures linked to the natural groundwater seepage zone, making it clearly distinguishable from the surrounding rock mass. Complementary active thermography field tests, involving the controlled introduction of colder water, simulated flow dynamics. Domain A exhibited minimal thermal response, which is consistent with low-permeability massive rock. In contrast, Domain B displayed rapid and heterogeneous thermal changes. These changes indicate discontinuity-controlled, unsaturated flow along preferential pathways. Moreover, groundwater and infiltration-induced seepage zones were most evident at the contact between quartzitic sandstone and weathered diabase. This shows that these lithological contacts are the most hydraulically conductive features in the rock mass even during active IRT surveys.

Thus, routine integration of passive and active IRT could enable early detection of thermal anomalies linked to seepage zones in similar fractured environments. Unlike traditional techniques such as borehole monitoring, moisture sensors, or visual inspections, most methods provide only indirect signs of possible flow zones. In contrast, IRT offers direct visualisation of seepage, early anomaly detection, and real-time tracking of evolving subsurface flow processes based on thermal contrasts. These capabilities, often challenging to achieve with conventional methods alone, demonstrate the novelty and practical value of IRT as a monitoring tool. They support proactive geohazard management in open-pit mining environments by enabling early warning of seepage-induced slope instability or uncontrolled groundwater inflow during excavation.

To guide future work, several areas for further study can build on these advancements. Key research directions include:

- ➤ Scale monitoring to full highwall or open-pit levels, with multiple injection points to map flow heterogeneity in complex fracture systems.
- ➤ Develop real-time IRT systems incorporating machine learning for environmental noise reduction and automated anomaly alerting to support geotechnical decision-making.
- ➤ Integrate IRT with complementary tools (e.g., drone-based imaging, photogrammetry) for multi-modal, cost-effective monitoring.
- ➤ Undertake long-term studies across diverse local lithologies, structures, and climatic conditions to establish standardised IRT protocols for seepage detection and risk assessment.

Acknowledgements

The financial support from the National Research Foundation (NRF) through the Thuthuka programme, the Water Research Commission (Project No. C2020/2021-00581), and SRK Consulting, Johannesburg, is gratefully acknowledged.

Author contributions

The following authors contributed to the study conception and design Mampho Maoyi, Prof J Louis van Rooy (Supervisor) and Prof Matthys Dippenaar (Supervisor). Material preparation, data collection and analysis were performed by Mampho Maoyi, Rory Bush (photogrammetry) and Andre Lotriet (Thermographer). The first draft of the manuscript was written by Mampho Maoyi and all authors commented on previous versions of the manuscript.

References

Abdulai, M., Sharifzadeh, M. 2019. Uncertainty and reliability analysis of open pit rock slopes: a critical review of methods of analysis. Geotechnical and Geological Engineering, vol. 37, pp.1223-1247. https://doi.org/10.1007/s10706-018-0680-y

Barton, N., Lien, R., Lunde, J.J.R.M. 1974. Engineering classification of rock masses for the design of tunnel support. Rock mechanics, vol. 6, pp.189-236. https://doi.org/10.1007/BF01239496

Berkowitz, B. 2002. Characterizing flow and transport in fractured geological media: A review. *Advances in water resources*, vol. 25 no. 8-12, pp.861-884.

Bieniawski, Z.T. 1973. Engineering classification of jointed rock masses. Civil Engineering= Siviele Ingenieurswese, vol. 1973, no.12, pp.335-343.

Bieniawski, Z.T. 1989. Engineering rock mass classifications: a complete manual for engineers and geologists in mining, *civil, and petroleum engineering*. John Wiley & Sons.

Chen, Z., Qian, J., Zhan, H., Zhou, Z., Wang, J., Tan, Y. 2017. Effect of roughness on water flow through a synthetic single rough fracture. Environmental earth sciences, vol. 76, no. 4, p.186.

Council for Geoscience. 1978. 1:250 000 Geological Map of 2528 Pretoria. Data Management Portal. Category: Geology. Updated December 2020. https://maps.geoscience.org.za/portal/apps/sites/#/council-for-geoscience-interactive-web-map-1

Dippenaar, M.A., Van Rooy, J.L. 2016. On the cubic law and variably saturated flow through discrete open rough-walled discontinuities. *International Journal of Rock Mechanics and Mining Sciences*, vol. 89, pp.200-211.

Eriksson, P.G., Reczko, B.F.F. 1995. The sedimentary and tectonic setting of the Transvaal Supergroup floor rocks to the Bushveld Complex. *Journal of African Earth Sciences*, vol. 21, no. 4, pp.487-504. https://doi.org/10.1016/0899-5362(95)00111-5

Eriksson, P.G., Altermann, W., Hartzer, F.J., Johnson, M.R., Anhaeusser, C.R., Thomas, R.J. 2006. The Transvaal Supergroup and its precursors. *The Geology of South Africa*, pp.237-260.

Gerke, H.H., Van Genuchten, M.T. 1993. A dual-porosity model for simulating the preferential movement of water and solutes in structured porous media. *Water resources research*, vol. 29, no. 2, pp.305-319.

Gigli, G., Frodella, W., Garfagnoli, F., Morelli, S., Mugnai, F., Menna, F., Casagli, N. 2014. 3-D geomechanical rock mass characterization for the evaluation of rockslide susceptibility scenarios. *Landslides*, vol. 11, pp.131-140. https://doi.org/10.1007/s10346-013-0424-2

Huang, N., Jiang, Y., Liu, R., Li, B., Sugimoto, S. 2019. A novel three-dimensional discrete fracture network model for investigating the role of aperture heterogeneity on fluid flow through fractured rock masses. *International Journal of Rock Mechanics and Mining Sciences*, vol. 116, pp.25-37. https://doi.org/10.1016/j.ijrmms.2019.03.014

International Society for Rock Mechanics. 1978. Suggested Methods for the Quantitative Description of Discontinuities in Rock Masses. Rock Characterisation Testing and Monitoring.

Kaveh Ahangaran, D., Ahangari, K., Eftekhari, M. 2022. Numerical analysis of blast-induced damage in rock slopes. Innovative Infrastructure Solutions, vol. 7, no.1, p.83. https://doi.org/10.1007/s41062-021-00684-w

Laubscher, D.H. 1990. A geomechanics classification system for the rating of rock mass in mine design. *Journal of the Southern African Institute of Mining and Metallurgy*, vol. 90, no.10, pp.257-273. https://doi.org/10.1016/0148-9062(91)90830-F

Li, T., Song, H., Huang, G., Bi, Y., Li, X. 2014. Assessment of groundwater changing trends through the generalized large well method with confined–unconfined flow model in open-pit mine area. Environmental Earth Sciences, vol. 72, pp.4599-4606. https://doi.org/10.1007/s12665-014-3357-8

Li, X., Li, Q., Wang, Y., Liu, W., Hou, D., Zhu, C. 2024. Effect of slope angle on fractured rock masses under combined influence of variable rainfall infiltration and excavation unloading. *Journal of Rock Mechanics and Geotechnical Engineering*, vol. 16, no.10, pp.4154-4176. https://doi.org/10.1016/j.jrmge.2024.08.019

Liu, Q., Zhang, Z., Zhang, B., Mu, W., Zhang, H., Li, Y., Xu, N. 2021. Hydrochemical analysis and identification of open-pit mine water sources: A case study from the Dagushan iron mine in Northeast China. *Scientific Reports*, vo.11, no.1, p.23152.

Lu, Y., Jin, C., Wang, Q., Li, G., Han, T. 2024. Deformation and failure characteristic of open-pit slope subjected to combined effects of mining blasting and rainfall infiltration. *Engineering Geology*, vol. 331, p.107437. https://doi.org/10.1016/j.enggeo.2024.107437

Luo, Y., Zhang, Z., Zhang, L., Xue, K., Long, K. 2022. Influence of fracture roughness and void space morphology on nonlinear fluid flow through rock fractures. *The European Physical Journal Plus*, vol. 137, no.11, p.1288.

Meola, C. 2012. Origin and theory of infrared thermography. *Infrared Thermography Recent Advances and Future Trends, Bentham eBooks*, pp.3-28. https://doi.org/10.2174/978160805143411201010003

Mineo, S., Pappalardo, G. 2021. Rock emissivity measurement for infrared thermography engineering geological applications. *Applied Sciences*, vol.11, no.9, p.3773. https://doi.org/10.3390/app11093773

Mineo, S., Calcaterra, D., Zampelli, S.P., Pappalardo, G. 2015. Application of Infrared Thermography for the survey of intensely jointed rock slopes. *Rendiconti Online della Società Geologica Italiana*, vol.35, pp.212-215. https://doi.org/10.3301/ROL.2015.103

Rosenbom, A.E., Jakobsen, P.R. 2005. Infrared thermography and fracture analysis of preferential flow in chalk. *Vadose Zone Journal*, vol.4, no.2, pp.271-280. https://doi.org/10.2136/vzj2004.0074

Sass, O., Bauer, C., Heil, S., Schnepfleitner, H., Kropf, F., Gaisberger, C. 2023. Infrared thermography monitoring of rock faces–Potential and pitfalls. *Geomorphology*, vol. 439, p.108837. https://doi.org/10.1016/j.geomorph.2023.108837

Silva, J., Worsey, T., Lusk, B. 2019. Practical assessment of rock damage due to blasting. *International Journal of Mining Science and Technology*, vol.29, no.3, pp.379-385. https://doi.org/10.1016/j.ijmst.2018.11.003

Teza, G., Marcato, G., Castelli, E., Galgaro, A. 2012. IRTROCK: A MATLAB toolbox for contactless recognition of surface and shallow weakness of a rock cliff by infrared thermography. *Computers & Geosciences*, vol. 45, pp.109-118. https://doi.org/10.1016/j.cageo.2011.10.022

Usamentiaga, R., Venegas, P., Guerediaga, J., Vega, L., Molleda, J., Bulnes, F.G. 2014. Infrared thermography for temperature measurement and non-destructive testing. Sensors, vol.14, no.7, pp.12305-12348. https://doi.org/10.3390/s140712305

Vollmer, M., Möllmann, K.P. 2018. Infrared thermal imaging: fundamentals, research and applications. John Wiley & Sons.

Wu, J.H., Lin, H.M., Lee, D.H., Fang, S.C. 2005. Integrity assessment of rock mass behind the shotcreted slope using thermography. *Engineering geology*, vol. 80, no.1-2, pp.164-173.

Xu, P., Yang, R., Zuo, J., Ding, C., Chen, C., Guo, Y., Fang, S., Zhang, Y. 2022. Research progress of the fundamental theory and technology of rock blasting. *International Journal of Minerals, Metallurgy and Materials*, vol.29, no.4, pp.705-716. https://doi.org/10.1007/s12613-022-2464-x

Xu, Y., Liao, X., Li, J., Chen, L., Li, L. 2021. The Effects of Water Content and Dry–Wet Cycles of Weak-Interlayer Soil on Stability of Clastic Rock Slope. *Geotechnical and Geological Engineering*, vol. 39, pp.3753-3760. https://doi.org/10.1007/s10706-021-01722-1

Yeh, C.H., Dong, J.J., Khoshnevisan, S., Juang, C.H., Huang, W.C., Lu, Y.C. 2021. The role of the geological uncertainty in a geotechnical design–A retrospective view of Freeway No. 3 Landslide in Northern Taiwan. *Engineering Geology,* vol.291, pp.106233. https:/doi.org/10.1016/j.enggeo.2021.106233

Zangerl, C., Koppensteiner, M., Strauhal, T. 2022. Semiautomated statistical discontinuity analyses from scanline data of fractured rock masses. *Applied Sciences*, vol.12, no.19, pp.9622.

Zhang, Q., Huang, X., Zhu, H., Li, J. 2019. Quantitative assessments of the correlations between rock mass rating (RMR) and geological strength index (GSI). Tunnelling and Underground Space Technology, vol.83, pp.73-81. https://doi.org/10.1016/j.tust.2018.09.015

Zhang, X., Ma, F., Yin, S., Wallace, C.D., Soltanian, M.R., Dai, Z., Ritzi, R.W., Ma, Z., Zhan, C., Lü, X. 2021. Application of upscaling methods for fluid flow and mass transport in multi-scale heterogeneous media: A critical review. Applied energy, 303, p.117603. https://doi.org/10.1016/j.apenergy.2021.117603

Zhao, L., Ren, T., Wang, N. 2017. Groundwater impact of open cut coal mine and an assessment methodology: A case study in NSW. *International Journal of Mining Science and Technology*, vol.27, no.5, pp.861-866. https://doi.org/10.1016/j.ijmst.2017.07.008

Zimmerman, R.W., Paluszny, A. 2023. Fluid flow in fractured rocks. John Wiley & Sons. ◆

The Focus for SAMCODES in Q2 2026

During Q2 2026, SAMCODES continued to focus on the planned update of the SAMREC Code, including preparation for industry consultation and alignment with evolving international reporting standards. Work also progressed on the integration of ESG guidance, education and training initiatives, and broader stakeholder engagement.

The SSC also advanced its promotion and sponsorship activities, while preparing for upcoming CRIRSCO, SAMREC/SAMVAL and other SAMCODES-related events.

LinkedIn

The SAMCODES LinkedIn page continues to be used to share current developments, industry updates and recognition of contributors. Appreciation posts are being prepared for long-serving SSC contributors, including Annalie de Bruyn and Rob Ingram. https://www.linkedin.com/company/samcodessa/

SAMCODES App

- The App continues to provide a convenient platform for accessing current SAMCODES information.
- The updated SAMCODES App User Guide is being maintained on the SAMCODES website, with refreshed guidance to support users. Committee quiz questions are also being developed, with previous examples being circulated to help avoid duplication.

Committee updates

SAMREC – THE SOUTH AFRICAN CODE FOR THE REPORTING OF EXPLORATION RESULTS, MINERAL RESOURCES AND MINERAL RESERVES	The SAMREC Committee is preparing the pre-update survey and progressing the Code rewrite. Follow-up engagement with SAMESG is planned to resolve outstanding ESG Guideline matters.
SAMVAL – THE SOUTH AFRICAN CODE FOR THE REPORTING OF MINERAL ASSET VALUATION	Planning continues for a SAMREC and SAMVAL Advanced Workshop, with further details to be confirmed.
SAMOG – THE SOUTH AFRICAN CODE FOR THE REPORTING OF OIL AND GAS RESOURCES	The proposed SAMOG Governance and Mandate review submitted by Andy Clay is under review.
	Engagement between the SAMREC and SAMESG Committees is continuing to address outstanding matters relating to the SAMESG Guideline and its integration with the forthcoming SAMREC Code update. A follow-up meeting between the committees is planned to resolve outstanding issues.
SAMCODES – SAMCODES STANDARDS COMMITTEE THE SOUTH AFRICAN MINERAL REPORTING CODES	Annalie de Bruyn retired from the JSE in July 2026. Zakaria Rashid will succeed her as the JSE representative on the SSC. Rob Ingram has retired as Chair of the JSE Readers Panel, with Andy McDonald succeeding him.

Training and Development

Compliance and Reporting Rules Course, MINN7052A was offered from 20 - 24 July 2026 through Wits University and coordinated by Dr Tania Marshall. The aim of the course is to upskill and create awareness on compliance requirements and Mineral Reporting Codes.

International Liaison

UNECE Resource Management Week 2026 was held from 27 April to 1 May 2026, highlighting the importance of UNFC classifications and resource management frameworks.

The AMREC-PARC-UNFC Workshop was held on 12-13 May 2026, with Tania Marshall invited to present on SAMREC. The next CRIRSCO AGM is scheduled for 7-11 September 2026 in Türkiye and will incorporate an IMVAL event.

The SSC is also progressing engagement with key South African stakeholders, including the Council for Geoscience and Minerals Council South Africa, with meetings to be scheduled.

Management Update

The SSC Annual Report covering June 2025 to May 2026 has been completed. The SSC is also reviewing its Governance and Mandate documentation, confirming member representation, and preparing the October 2026 update to the GSSA and SAIMM. Joseph Mainama continues as SSC Chair, supported by Jacques Nel as Deputy Chairperson.

Dichloromethane-assisted phase separation for simultaneous recovery of oil and rare earth elements from oil-rich grinding sludge

by Z. Minglin[1], L. Xin[1], Y. Weilu[1], K. Htet Oo[1], C. Yu[1], Q. Wensheng[2], B. Dejun[3], K. Hua[3], Z. Suiyi[1,3]

Affiliation:
1 No. 102-Joint Lab, Zhongkai University of Agriculture and Engineering, Guangzhou China
2 Department of Biology, Lakehead University, Thunder Bay, ON Canada
3 Jilin Province Key Lab for Municipal wastewater treatment, Changchun Institute of Technology, Changchun China

Correspondence to:
Z. Suiyi

Email:
papermanuscript@126.com

Dates:
Received: 12 May. 2025
Revised: 18 Oct. 2025
Accepted: 26 Jun. 2026
Published: Aug. 2026

How to cite:
Minglin Z., Xin L., Weilu Y., Htet Oo K., Yu C., Wensheng Q., Dejun B., Hua K., Suiyi Z. 2026. Dichloromethane-assisted phase separation for simultaneous recovery of oil and rare earth elements from oil-rich grinding sludge. *Journal of the Southern African Institute of Mining and Metallurgy*, vol. 126, no. 8, pp. 447 – 454

DOI ID:
https://doi.org/10.17159/2411-9717/3726/2026

ORCiD:
Z. Minglin
https://orcid.org/0009-0004-2972-4472
L. Xin
https://orcid.org/0009-0002-8094-8485
Y. Weilu
https://orcid.org/0000-0003-3985-9093
K. Htet Oo
https://orcid.org/0009-0003-5792-8010
C. Yu
https://orcid.org/0009-0003-4062-2760
Q. Wensheng
https://orcid.org/0000-0003-2178-4003
B. Dejun
https://orcid.org/0000-0001-6188-6560
K. Hua
https://orcid.org/0000-0002-1093-3168
Z. Suiyi
https://orcid.org/0009-0005-9710-1151

Abstract

Grinding sludge is a gel-like hazardous waste generated in large quantities during metal cutting processes. Conventional calcination and hydrometallurgical treatment of oil-rich grinding sludges emit flue gases and generate insoluble residues. This study proposes CH_2Cl_2-assisted phase separation under mild conditions to enhance oil removal and metal recovery by overcoming encapsulation effects. Neodymium iron boron grinding sludge, containing 10.4% oil, 8.3% neodymium, 4.5% praseodymium), and 55.8% Fe was selected as a representative material. The dissolution efficiency of the sludge in hydrochloric acid alone or after dichloromethane pretreatment was less than 85%, whereas complete dissolution was achieved using a dichloromethane/hydrochloric acid mixed solvent. After that, phase separation produced an organic phase enriched with 10.44% oil, as well as carbon and grease, and an aqueous phase containing 10 g/L Nd, 3.75 g/L Pr, and 71 g/L Fe. The organic phase could be easily evaporated, allowing for the recovery of approximately 90% of the dichloromethane, with oil, carbon powder, and grease remaining as residues. The aqueous phase was subsequently processed to sequentially precipitate a double salt containing 98.58% Nd/Pr and an iron yellow product with 99.97% Fe. This approach provides an effective and economical strategy for the simultaneous recovery of oil and metallic products from grinding sludge, avoiding the need for harsh conditions or costly equipment. Consequently, it offers significant potential for practical on-site applications in industrial settings.

Keywords

Grinding sludge, oil-rich NdFeB waste, recycling, dichloromethane, rare earths

Introduction

Neodymium iron boron (NdFeB) is a significant magnetic material consisting of various rare earth elements (München, Veit, 2017). It demonstrates exceptional magnetic properties (Herbst, Croat, 1991), corrosion resistance, and thermal stability, which render it widely applicable in multiple fields, including electric motors (Bozkurt et al., 2021), generators (Rahman, Slemon, 1985), loudspeakers (Warren, 1995), and magnetic resonance imaging (Torresan et al., 2021). During the manufacturing process, NdFeB materials are typically processed into various geometries to meet diverse installation requirements or to enhance their performance characteristics. However, during processing, the generation of NdFeB waste is unavoidable. This waste not only depletes valuable resources but also poses potential environmental risks (Kumari, Sahu, 2023).

The hydrometallurgical process offers several advantages for recovering NdFeB waste, including the generation of high-purity products under mild conditions, reduction of gas emissions, and minimisation of secondary waste (Lin et al., 2019; Önal et al., 2017). A classic approach involves leaching NdFeB waste with hydrochloric acid, which facilitates the precipitation of rare earth elements using oxalic acid (Vander Hoogerstraete et al., 2014) or carbonate (Li et al., 2025). The resulting precipitates are then calcined to produce rare earth powders suitable for reuse in NdFeB magnet production (Kumari et al., 2018). To reduce impurity leaching, various pretreatment methods are employed, including high-temperature calcination (Cong et al., 2023; Erust et al., 2023; Jiang et al., 2020; Omodara et al., 2019; Yadav et al., 2024), hydrothermal leaching (Heo et al., 2024; Rabatho et al., 2013), and hydrogen peroxide/nitrate oxidation (Zhihan et al., 2022). For example, Jiang et al. (2020) calcined NdFeB waste at 800 oC and subsequently treated it hydrothermally at 120 oC, achieving leaching efficiencies of 96.3% for rare earth elements and 13.3% for iron; iron was then precipitated at pH 3.5 with the addition of hydrogen peroxide. The resultant waste typically appears as powder or fragments from dry cutting processes. However, in some manufacturing processes, the lubricants and auxiliary reagents were used to enhance machining accuracy, leading to the generation of abundant oil-rich NdFeB waste (Wang et al., 2022). The removal of oil from the waste is critical in the recovery process (Kang et al., 2024).

In some factories, the oil-rich NdFeB waste is often disposed of by direct combustion. During this process, metallic iron and rare earth powders are oxidised, while the oil components combust and decompose, resulting in significant smoke emissions (Gong et al., 2022). The oxidation of iron can lead to the formation of spinel crystals, which co-crystallise with rare earth elements (Zakeri, Tafaghodi, 2025), thereby reducing the leaching efficiency. Additionally, high-temperature pyrolysis is employed to decompose the oil and facilitate the in situ reduction of rare earth and iron oxides (Chu et al., 2023). In these processes, a layer of "carbon-coating" and "metallic-coating" is generated on NdFeB particles (Liu et al., 2023; Suiyi et al., 2025), leading to substantial leaching residues (Piyawit et al., 2018). To date, recovering oily sludge under mild conditions has not been reported.

This study presents a novel strategy for converting oily sludge into organic compounds, double salts, and akaganeite particles under atmospheric conditions. The corresponding parameters are optimised, and the underlying principles are also discussed.

Materials and methods

Sludge pretreatment

The oil sludge was acquired from Dongya rare earth company (Jilin, China). It was directly immersed into 6M HCl liquid at the solid to liquid ratio of 1:10 without drying, and then agitated at 400 rpm for 6 h. After that, it was collected by the high-speed centrifugation. A repeat experiment was also performed, in which the HCl liquid was replaced by H_2O, H_2SO_4, and NaOH, separately.

During the leaching tests, the hydrochloric acid was optimised in the leaching of rare earths and then used in the following steps (Figure 1). Firstly, 75 mL hydrochloric acid was mixed with 25 mL dichloromethane, to form a mixed solution. Secondly, 10 g sludge was added to the solution, and then agitated at 400 rpm for 6 h. Thirdly, the mixture was left to stand overnight for stratification. Thus, the water phase and the oil phase were collected separately. The experiment was repeated by replacing the dichloromethane by kerosene, and ethanol, respectively.

Leachate treatment

Rare earth separation

The water phase was rich in rare earths, and then simulated in the laboratory by using pure reagents. To separate the valuable rare earth, the water phase was mixed with 4.5 g Na_2SO_4, and then agitated at 200 rpm for 5 min. Correspondingly, the Na_2SO_4 was replaced by using $Na_2C_2O_4$, NaH_2PO_4, K_2SO_4, and $(NH_4)_2SO_4$, separately. In addition, the reaction conditions were also optimised in the range of 30 g/L – 100 g/L Na_2SO_4 dosage, room temperature to160 oC and at pH -0.2 – pH 1.5. After reaction, some precipitates were generated, and then collected. The supernatant was also collected for characterisation.

Fe separation

After the separation of rare earths, the resulting supernatant was treated to separate Fe in the following steps. The supernatant was mixed with 4.4 g nitrite, and then heated to 90 oC under atmosphere condition, and then stepwisely adjusted to pH 1.5, 2.0, 2.5, and 3.0. Accordingly, a portion of supernatant was sampled for characterisation.

Results and discussion

Leaching of rare earth from the sludge

The oil sludge was a black adhesive polymer, and did not show any special diffraction peaks in its XRD pattern (Figures 2a, b, and c). It contained 11.70% water, 10.44% oil, 55.82% Fe, 8.28% Nd, 4.48% Pr, and few impurities of Mn/Cu (Figure 2d).

When the oil sludge was washed by water and NaOH, no significant change was observed (Figure 3a). However, by using hydrochloric acid, the leaching efficiencies of Fe, Nd, and Pr were 84.82%, 55.35%, and 32.12%, respectively, higher than those when using sulfuric acid. This showed the benefit of hydrochloric acid in the leaching.

To increase the leaching efficiency, dichlormethane, kerosene, and ethanol were added to act as promoters in hydrochloric acid leaching (Figure 3a). By using dichloromethane, the Fe leaching did not change, but the Nd and Pr leaching became more efficient. The leaching efficiencies of Fe, Nd, and Pr were decreased to 58.03%, 44.41% and 25.26%, respectively, by adding ethanol, and decreased to 2.13%, 1.69% and 1.48%, respectively, by adding kerosene. These results demonstrated the advantage of hydrochloric acid and dichloromethane in leaching the oil sludge.

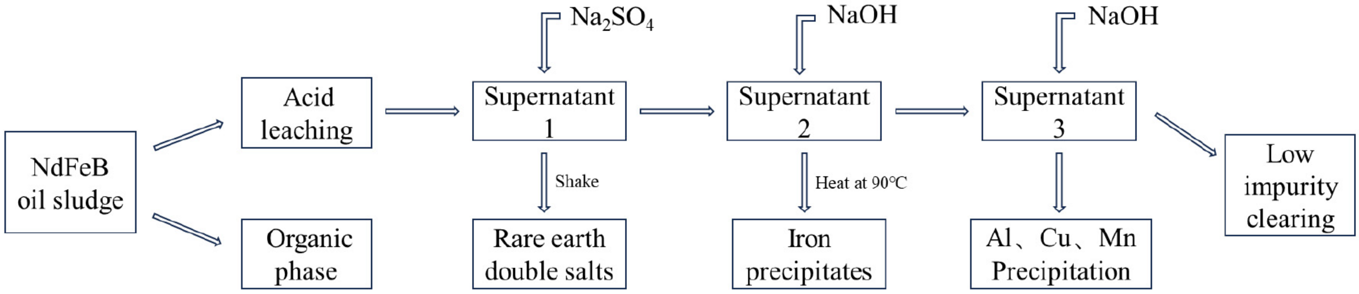

Figure 1—Flow chart of oil sludge treatment

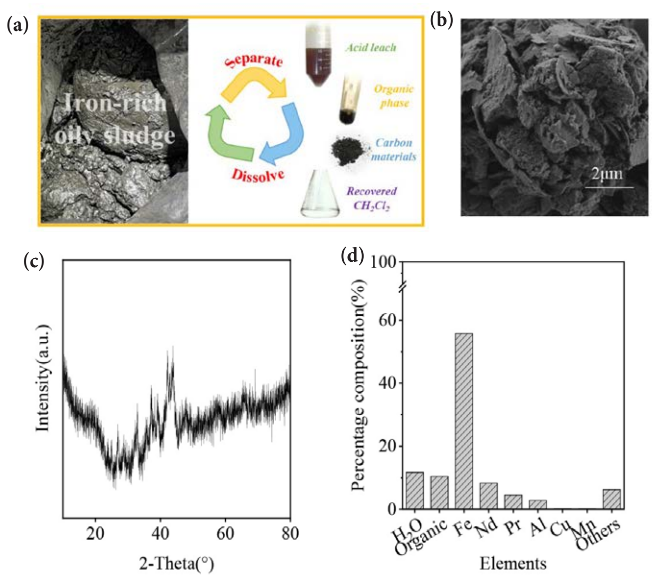

Figure 2—(a) Picture, (b) SEM, (c) XRD pattern, and (d) major composition of the oil sludge

When the ratio of hydrochloric acid and dichloromethane was varied from 1:3 to 3:1, the leaching efficiencies of Fe, Nd and Pr were also increased from 3.69%, 6.84%, and 9.73, respectively, to 97.89%, 95.93%, and 87.61% respectively; however, when the ratio was further varied to 5:1 the leaching efficiencies dropped to 26.18%, 12.45% and 12.83%, respectively (Figure 3b). The optimal ratio of hydrochloride acid and dichloromethane was 3:1, and the generated leachate contained 71 g/L Fe, 10.0 g/L Nd, 3.75 g/L Pr, 0.90 g/L Al, 0.34 g/L Cu, and 0.24 g/L Mn.

The resulting organic phase was yellowish and is further evaporated at 40 oC to separate dichloromethane, whilst the resulting component comprised 98.63% base oil, 0.13% carbon, and 1.24% grease (Figure 3c). The base oil mainly contained 2, 6, and 10-trimethyltridecane, tetradecane, butylated hydroxytoluene, nonadecane, eicosane, and 1 and 3-benzenedicarboxylic acid bis (2-ethylhexyl) ester (Figure 3d). The regenerated dichloromethane was purified to > 99.7% (Figures 3e and f). However, the base oil comprised 24.98% aromatic hydrocarbons and 75.02% long-chair alkanes (Figure 3e), and can be refined. During the organic phase recovery, about 12.21% dichloromethane was lost due to its rapid evaporation.

After leaching, a small portion of undissolved solid was also generated and attached onto the beaker wall. It is also blackish and sticky, and showed amorphous aggregates with porous surface (Figures 3g and h). After drying, its major composition included 28.98% Na, 43.65% Si, 6.57% Cl, and minor amounts of S, Ca, and Mg.

Rare earth separation and Fe recycling

Rare earth separation route

The leachate was treated by adding sodium salts. When the sodium sulphate was added at the dosage of 60 g/L, the removal of Nd and Pr achieved by 98.25% and 98.92%, with the co-removal of 1.79% Fe, 12.07% Al, 21.74% Cu, and 3.13% Mn (Figure 4a). But by adding sodium oxalate, the removal efficiencies of Nd and Pr were decreased to 93.70% and 93.84%, respectively, whilst these of

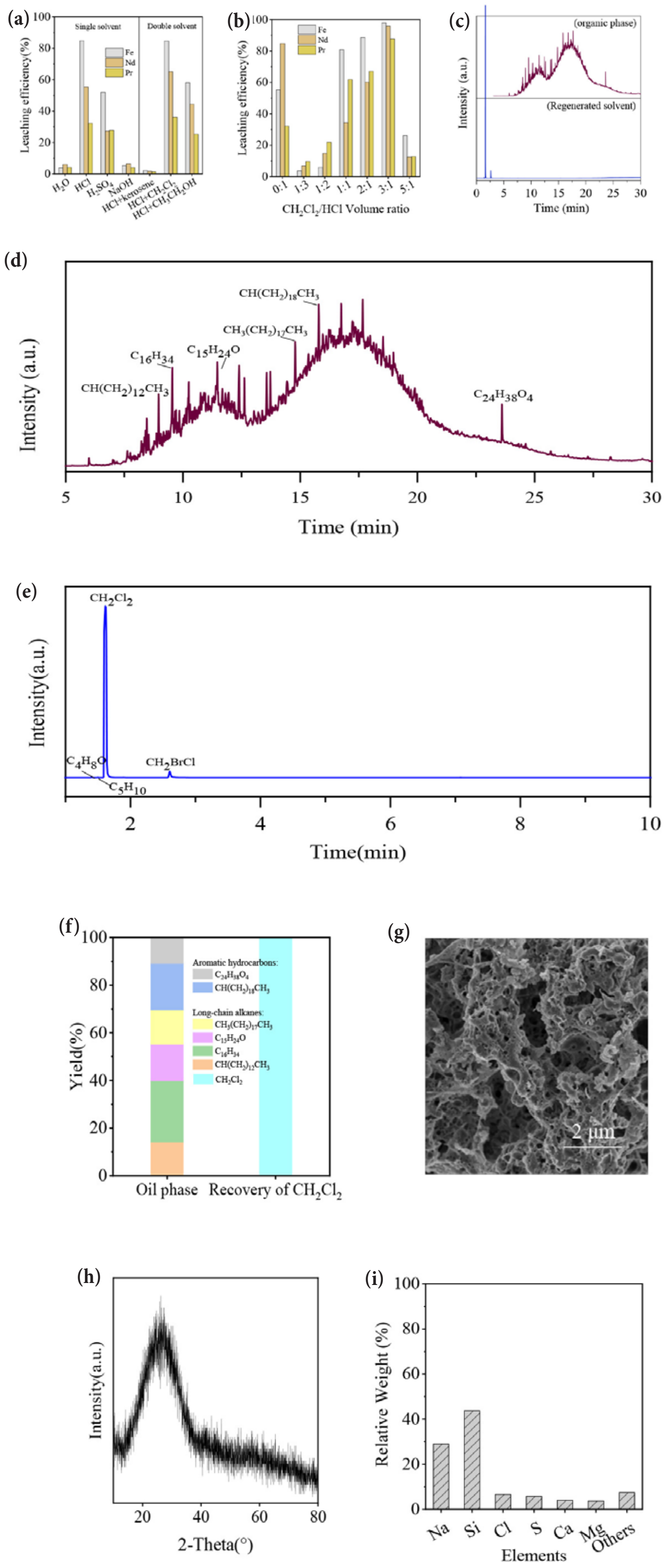

Figure 3—Dissolution of oil sludge. (a) method comparison, (b) ratio optimisation, (c) composition of the separated oil phase, GC-MS spectra of (d) oil phase and (e) the recycled dichloromethane, (f) composition of liquid base oil and regenerated dichloromethane, (g) SEM, (h) XRD pattern and (i) major composition of undissolved particles

Fe, Al, Cu, and Mn were increased to 35.73%, 21.06%, 78.85% and 16.88%, respectively. When the sodium oxalate was replaced by the sodium phosphate, the removal efficiency of Fe did not change, but these of Nd, Pr, Al, and Mn increased to 99.71%, 98.77%, 96.01% and 20.58%, respectively, whilst that of Cu dropped to 20.58%. After precipitation, only the leachate pH of sodium phosphate was increased to 1.94, whilst the others did not vary (Figure 4a). The sodium sulphate was cheap and then used in the following test.

When the dosage of sodium sulphate was increased from 30 g/L to 60 g/L, and 100 g/L, the removal efficiencies of Nd and Pr were increased from 75.10% and 80.18%, respectively (Figure 4b), to 98.25% and 98.92%, respectively, and further to 99.79% and 98.59%, respectively, whilst the removal of Fe, Al, Cu, and Mn did not vary apparently. Accordingly, the leachate pH was slightly increased from -0.2 to 0.47. When the reaction temperature was increased from room temperature to 120 oC, and further to 160 oC, the removal efficiencies of Nd and Pr were unchanged, and those of Fe, Al, Cu, and Mn showed similar variation (Figure 4c). In addition, when the leachate pH was adjusted from -0.2 to 0, 0.8 and 1.5, the Nd and Pr removal also did not vary, whilst the loss of Fe, Al, Cu, and Mn were slightly increased to 3.79%, 18.96%, 24.21%, and 15.61% (Figure 4d), respectively. The final pH also varied to 0.28, 0.84, 1.24, and 1.60. Thereby, the separation of Nd and Pr from the leachate was optimal at the initial pH -0.2 at room temperature with the addition of 60 g/L sodium sulphate. Under such condition, the generated precipitate was a mixture of Nd/Pr sulphate salt (Figure 4e) in the stick-shaped aggregates (Figure 4f). It contained 44.73% Nd, 14.12% Pr, 24.53% S, and 14.91% Na (Figure 4g), in accordance with the formation of Nd3Pr $(SO_4)_3 \cdot 3Na_2SO_4 \cdot H_2O$.

Fe removal route

After precipitating Nd and Pr, the resulting concentrations of Nd, Pr, Fe, Al, Cu, and Mn were 0.371 g/L, 0.117 g/L, 70.965 g/L, 0.834 g/L, 0.297 g/L and 0.207 g/L in the supernatant, respectively. The supernatant was further heated to 90 oC with the addition of 58 g/L nitrite, and then adjusted by NaOH. The removal efficiency of Fe was 74.69% at pH 0.5, and rapidly increased to 96.98% at pH 1, and further to 99.92% at pH 1.5, and nearly 100% at pH 2 and 3. Accordingly, the removal efficiencies of Al and Cu were only 5.62% and 7.17% at pH 0.5, respectively, but steadily increased to 15.59% and 10.94% at pH 1 and further to 67.23 and 23.96% at pH 3, respectively. However, the removal efficiencies of Nd, Pr, and

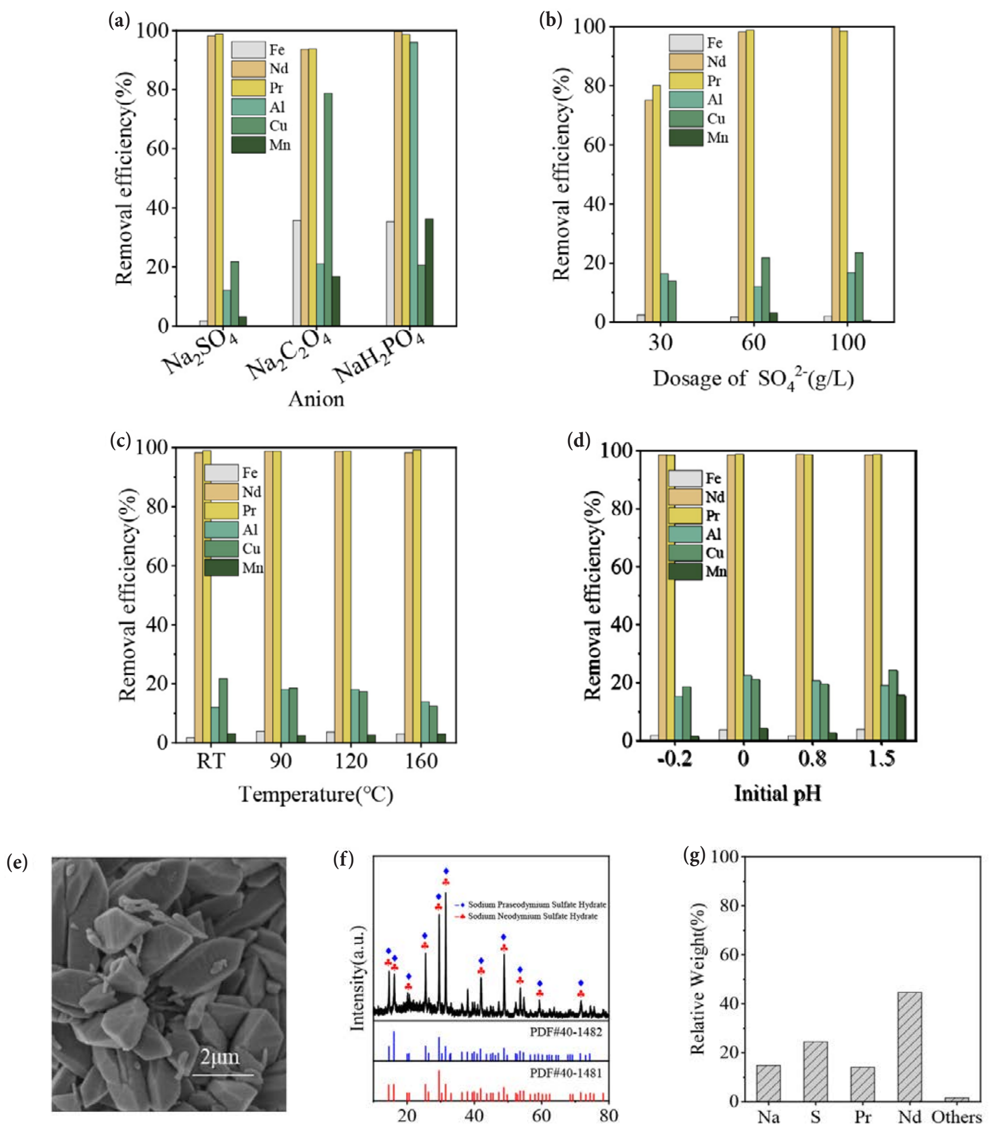

Figure 4—Separation of rare earth from the leachate. Comparison of (a) sodium salt, (b) effect of sodium sulphate dosage optimisation, (c) reaction temperature, (d) initial pH; (e) SEM, (f) XRD and (g) major composition of precipitates

Mn were 7.35%, 2.45%, and 15.92% at pH 0.5, respectively, and did not vary with the pH increasing to 1 and 3. The optimal pH for Fe removal is 3.0, and the removed Fe was in the form of akaganeite particles (Figures 5 b and c) and comprised of 68.34% Fe with the major impurities of 10.45% Na, 12.72% S, 3.187% Al, 4.26% Cl, and few Cu, Mn (Figure 5d). The generated akaganeite particles exhibited a high iron (Fe) content exceeding 65%, meeting the standard for high-grade iron ore concentrates. Consequently, these particles serve as a highly desirable raw material for smelting in the iron and steel market.

Major mechanism for recycling oil sludge

The oil sludge was a mixture of metallic particles/oxides, oil and carbon materials, which was then dissolved into the mixture of dichloromethane and hydrochloric acid, with the residual of Si-bearing undissolved solid. The metallic particles and oxides were dissolved in mineral acid, but not in pure water and alkaline liquid. By using hydrochloric acid, the dissolution of Fe, Nd, and Pr only achieved by 84.82%, 55.35% and 32.12%, due to the formation of oil-coated particles (Figure 6a). The oil layer stopped the diffusion of acid, so that large portions of Nd and Pr were not dissolved. The oil sludge comprised 10.44% organics, and showed a 128.22-125.11 contact angle (Figure 6b). It had a hydrophobic surface and was then washed by dichloromethane, to produce amorphous aggregates (Figures 6c and d). Such aggregates were also dissolved using hydrochloric acid. In order to produce a portion of undissolved particles twenty-four times greater, a mixture of dichloromethane and hydrochloric acid was used. This is attributed to the metallic layer and the oil layer. The metallic layer covered the organics and then inhibited the dissolution of organics into dichloromethane (Figure 6a). Subsequently, the metallic layer was dissolved by hydrochloride acid, and then the oil layer was exposed,

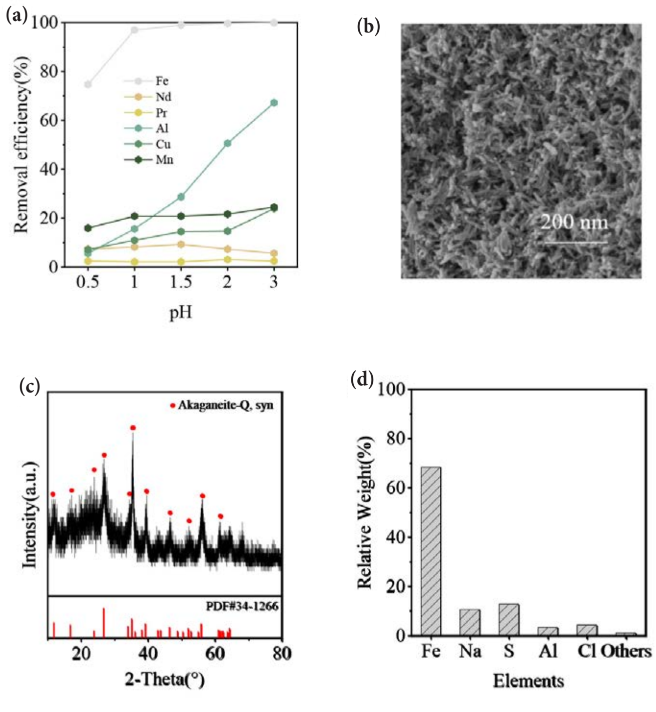

Figure 5—(a) removal efficiency of Fe and other elements, (b) SEM, (c) XRD pattern, and (d) major composition of generated deposit

to stop the following dissolution of hydrochloric acid. Thus, by using the mixture of dichloromethane and hydrochloric acid, the dissolution of oil layer and the metallic layer continued, into the dichloromethane phase and the acid liquid phase, separately.

The sulphuric acid also dissolved Nd and Pr from the oil sludge, to form $FeHSO_4$+, Fe^2+ and $FeSO_4$ (Figure 6e). This step did not precipitate the double salt due to the lack of sodium ion. Comparing with the sulfuric acid, the hydrochloric acid provided enough chloride to complex Nd and Pr to form Fe^2+ and $FeCl^+$ (Figure 6f), and thereby showed high dissolution efficiency of Nd and Pr. The dichloromethane was a good solvent that can efficiently dissolve oils, compared to ethanol and kerosene. Only a few organic-metal complexes were attached onto the sludge and then released into water, in accordance with the low dissolution of Fe, Nd, and Pr into the pure water and the alkaline liquid.

After dissolution, the dichloromethane became blackish, and was regenerated to a transparent via an evaporation route, with the separation of base oil. The obtained acid solution contained Fe, Nd, Pr and other metallic ions, and was precipitated by using sodium sulphate, to separate Nd and Pr prior to Fe (Equations 1 and 2). The separation of Nd and Pr as a double salt was only affected with a dosage of sodium sulphate, and not with the reaction temperature and the initial pH condition. The Nd/Pr double salt was small particles and revealed a surface to adsorb such metallic ions, including Fe, Al, Cu, and Mn. When the initial pH was adjusted to 1.5, a portion of Fe, Al, Cu, and Mn was also hydrolysed as hydrated ion. This enhanced the attachment/adsorption of Fe/Al/Cu/Mn on the Nd/Pr double salt. But when the sodium sulphate was replaced by sodium oxalate, the reaction of oxalate and Nd/Pr took place, along with the precipitation of ferrous iron oxalate and cupric oxalate (Klemettinen et al., 2023). The phosphate similarly reacted to precipitate Nd, Pr, Fe, and Al. This added more impurities into the Nd/Pr double salt(He et al., 2022).

$$Na^+ + Nd^{3+} + 2HSO_4^- + H_2O \rightarrow NaNd(SO_4)_2 \cdot H_2O + 2H^+ \quad [1]$$

$$Na^+ + Pr^{3+} + 2HSO_4^- + H_2O \rightarrow NaPr(SO_4)_2 \cdot H_2O + 2H^+ \quad [2]$$

$$NO_2^- + Fe^{2+} + 2H^+ \rightarrow Fe^{3+} + NO\uparrow + H_2O \quad [3]$$

$$Fe^{3+} + 3H_2O \leftrightharpoons Fe(OH)_3 + 3H^+ \quad [4]$$

$$Fe^{3+} + 2H_2O \rightarrow FeOOH + 3H^+ \quad [5]$$

$$FeOOH \rightarrow Fe_2O_3 + H_2O \quad [6]$$

$$3Fe^{3+} + 2SO_4^{2-} + Na^+ + 6H_2O \rightarrow NaFe_3(SO_4)_2(OH)_6 + 6H^+ \quad [7]$$

After the precipitation of Nd and Pr, the supernatant contained an abundance of ferrous iron and minor Al, Cu, and Mn. The ferrous iron was rapidly oxidised to ferric iron by adding nitrite (Equation 3), and then precipitated as Fe-rich oxyhydroxides (Equations 4 and 5) by adding sodium hydroxide. At room temperature, the ferric iron was hydrolysed as flocs, which flocculated and co-precipitated Al, Cu, and Mn. But the ferric iron was hydrolysed and rapidly crystallised as needle-sharp akaganeite particles at 90 oC (Figure 6g). The particles showed a small number of surface sites comparing with the flocs, and led to the decrease of the co-removal of Al, Cu, and Mn.

Application and perspectives

After Fe separation, the resulting supernatant also comprised 0.25

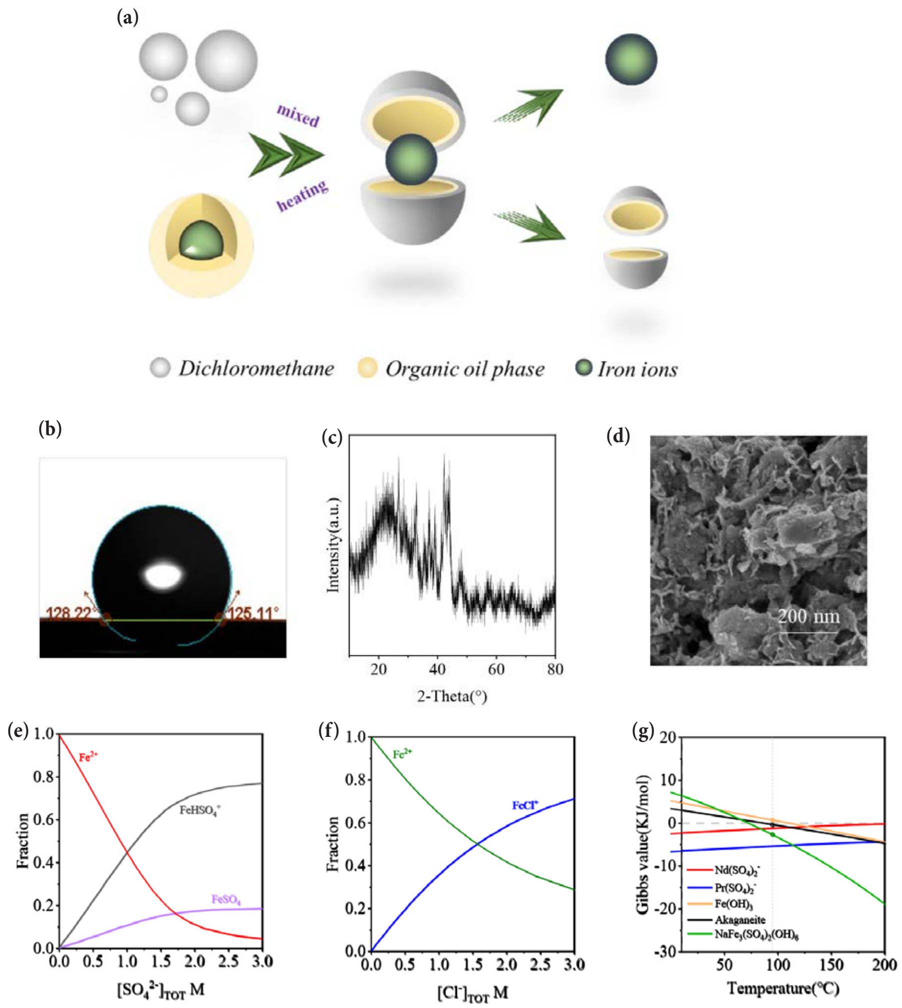

Figure 6—(a) Illustration graph of oil sludge dissolution and recycling. (b) Contact angle determination, (c) SEM and (d) XRD of particles after washing by dichloromethane; Fitted plot of (e) sulphate and (f) chloride versus pH; (g) thermodynamic analysis

g/L Fe, 0.33 g/L Nd, 0.19 g/L Pr, and few Al, Cu, and Mn (Figure 7a). The solution was directly adjusted to pH 12, and more than 99.51% Fe, Nd, Pr, Al, Cu, and Mn were co-precipitated as irregular particles (Figure 7b). The particles also showed a broad peak in their XRD patterns (Figure 7c), in accordance with the formation of amorphous Fe-rich oxyhydroxides. Such deposits can be collected and then re-dissolved in the hydrochloric acid. Thus, they can be mixed with the oil sludge and dissolved in the aforementioned step. However, with the precipitation treatment, the resulting solution was rich in sodium chloride and sodium sulphate, and often evaporated to produce waste salt that should be further treated by others.

With the aforementioned treatment, the oil sludge was completely recycled as products, including the base oil, the double salt and the Fe-rich particles. Figure 7d showed that nearly all organics were separated as base oil, carbon particles and grease. 98.25% Nd and 98.92% Pr were recycled as the double salt, and more than 98.13% Fe was separated as high-purity Fe oxyhydroxides. The base oil can be reused as fuel, in calcination or in the heating industry. The Fe-rich oxyhydroxides contained 65.12% Fe and can be used as raw materials in iron and steel smelting. The resulting rare earths and other metals were coprecipitated and then collected for dissolution in the next process.

The aforementioned recycling of oil sludge also has some defects. Firstly, the dichloromethane was used as solvent for dissolving the oil sludge, but it is volatile and carcinogenic, and harmful to the atmospheric environment. Secondly, the Fe removal was performed at 90 oC, and often consumed extra energy. Thirdly, sodium and sulphate ions were added to the leachate with the removal of Fe, Nd, and Pr. The leachate was salty waste and should be further treated.

Conclusion

A novel strategy was developed to recover organic products, double salts, and akaganeite particles from the oil-rich NdFeB waste under atmospheric conditions. The NdFeB sample was composed of 10.44% oil phase and 77.62% metallic components. It was effectively dissolved in a mixed reagent comprising 98.86% dichloromethane and 99.17% hydrochloric acid. Following stratification, this process resulted in the separation of an organic phase and an acid leachate, with a small amount of Si/Na-rich undissolved solids remaining. Moreover, over 85% of the dichloromethane was regenerated by evaporating the organic phase at 40 °C. The evaporation process also yielded three marketable products: carbon materials, grease, and base oil. The acid leachate, which demonstrated high concentrations of Nd, Pr, and Fe, was subsequently processed to precipitate Nd/Pr as double salts and Fe as akaganeite particles. This strategy facilitated the recycling of 98.25% Nd, 98.92% Pr, 99.97% Fe, and

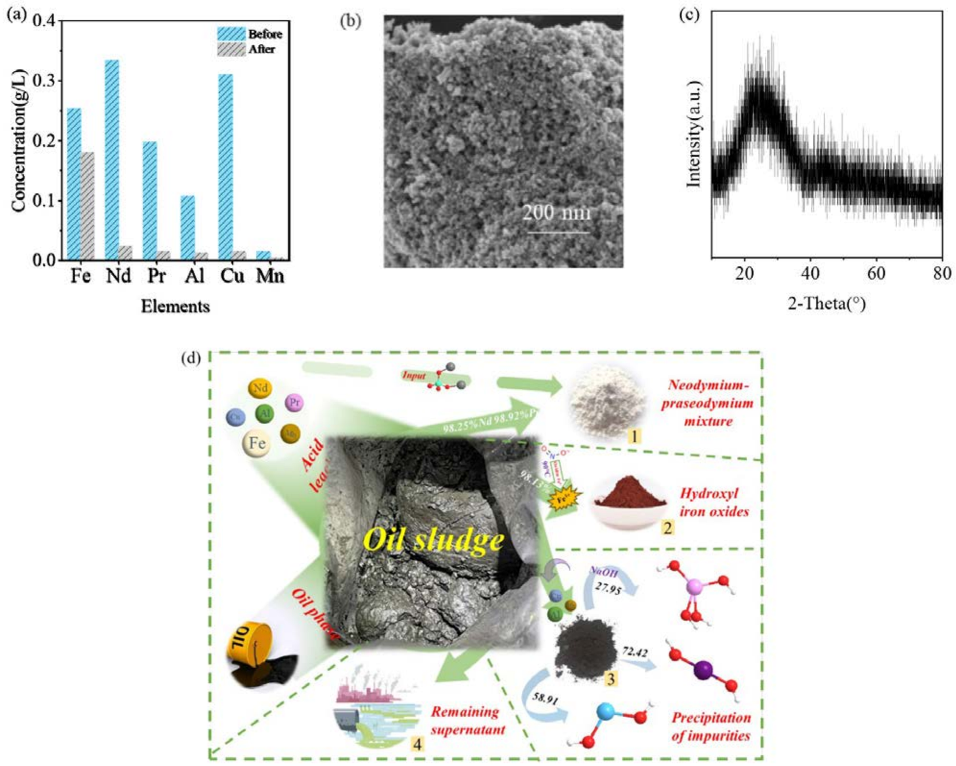

Figure 7—(a) Major composition of the residual solution, (b) SEM and (c) XRD pattern of deposits; (d) Mass balance of rare earth recycling from the oil sludge

nearly 100% of the organic components from the oil-rich NdFeB.

Credit authorship contribution statement

Minglin Zheng: Writing original draft. Xin Lan: Software. Weilu Yang: Supervision, project administration, formal analysis. Htet Oo Kaung: Software, data curation. Yu Chen: Software. Wensheng Qin: Supervision. Dejun Bian: Resources, validation. Hua Kang: Formal analysis. Suiyi Zhu: Writing - original draft, methodology, funding acquisition, conceptualisation.

Declaration of competing interest

The authors declare that they have no known competing financial interests or personal relationships that could have appeared to influence the work reported in this paper.

Acknowledgement

This work was supported by the National Natural Science Foundation of China (No. 52370158, 52470076 and 52070038), the Science and Technology Programme of Jilin Province (Grant No. 20240304153SF), the Featured Innovation Project of Guangdong Provincial Department of Education (No. 2023KTSCX050).

Data availability statement

All data supporting the findings of this study are included in this published article and its supplementary information files.

References

Bozkurt, A., Baba, A., Oner, Y. 2021, 2021. Design of Outer-Rotor Permanent-Magnet-Assisted Synchronous Reluctance Motor for Electric Vehicles. Energies. https://doi.org/10.3390/en14133739

Chu, Z., Li, Y., Zhang, C., Fang, Y., Zhao, J. 2023. A review on resource utilization of oil sludge based on pyrolysis and gasification. *Journal of Environmental Chemical Engineering*, vol. 11, no.3, pp. 109692. https://doi.org/https://doi.org/10.1016/j.jece.2023.109692

Cong, L., Yu, L., Zhou, Q., Lu, Q., Yue, M. 2023. Short-process recycling of Nd-Fe-B sintered magnet sludge wastes: Challenges and approaches. *Journal of Rare Earths,* vol.41, no.10, pp. 1467-1477. https://doi.org/https://doi.org/10.1016/j.jre.2023.04.019

Erust, C., Karacahan, M. K., Uysal, T. 2023. Hydrometallurgical Roadmaps and Future Strategies for Recovery of Rare Earth Elements. *Mineral Processing and Extractive Metallurgy Review*, vol. 44, no. 6, pp. 436-450. https://doi.org/10.1080/08827508.2022.2073591

Gong, Z., Zhang, H., Juan, Y., Zhu, L., Zheng, W., Ding, J., Tian, M., Li, X., Zhang, J., Guo, Y., Li, G. 2022. A review of application and development of combustion technology for oil sludge. *Journal of Environmental Science and Health*, Part A, vol. 57, no.5, pp. 396-412. https://doi.org/10.1080/10934529.2022.2071067

He, L., Xu, Q., Li, W., Dong, Q., Sun, W. 2022. One-step separation and recovery of rare earth and iron from NdFeB slurry via phosphoric acid leaching. *Journal of Rare Earths*, vol. 40, no. 2, pp. 338-344. https://doi.org/https://doi.org/10.1016/j.jre.2021.01.003

Heo, S., Kim, R., Yoon, H.-S., Kim, C.-J., Chung, K. W., Lee, S. 2024. Effect of pretreatment methods on the selective leaching of rare earth elements from NdFeB permanent magnets using deep eutectic solvents. *Hydrometallurgy*, vol. 226, pp. 106284. https://doi.org/10.1016/j.hydromet.2024.106284

Herbst, J.F., Croat, J.J. 1991. Neodymium-iron-boron permanent magnets. Journal of Magnetism and Magnetic Materials, vol. 100, no. 1, pp. 57-78. https://doi.org/https://doi.org/10.1016/0304-8853(91)90812-O

Jiang, Y., Deng, Y., Xin, W., Guo, C. 2020. Oxidative Roasting–Selective Pressure Leaching Process for Rare Earth Recovery from NdFeB Magnet Scrap. *Transactions of the Indian Institute of Metals*, vol. 73, no.3, pp. 703-711. https://doi.org/10.1007/s12666-020-01888-x

Kang, C., Guo, J., Kiyingi, W., Fei, D., Xiong, R. 2024. Sustainable treatment and recycling of oily sludge: Incorporation into gel -system to improve oil recovery. *Journal of Cleaner Production*, vol. 436, pp. 140640. https://doi.org/https://doi.org/10.1016/j.jclepro.2024.140640

Klemettinen, A., Adamski, Z., Chojnacka, I., Leśniewicz, A., Rycerz, L. 2023. Recovery of Rare Earth Elements from the Leaching Solutions of Spent NdFeB Permanent Magnets by Selective Precipitation of Rare Earth Oxalates. *Minerals*, vol. 13, no.7.

Kumari, A., Sahu, S.K. 2023. A comprehensive review on recycling of critical raw materials from spent neodymium iron boron (NdFeB) magnet. *Separation and Purification Technology*, vol. 317, pp. 123527. https://doi.org/https://doi.org/10.1016/j.seppur.2023.123527

Kumari, A., Sinha, M.K., Pramanik, S., Sahu, S.K. 2018. Recovery of rare earths from spent NdFeB magnets of wind turbine: Leaching and kinetic aspects. *Waste Management*, vol. 75, pp. 486-498. https://doi.org/https://doi.org/10.1016/j.wasman.2018.01.033

Li, S., Wu, S., Wang, S., Liu, G., Zhan, Y., Tong, J., Zhou, K., Xie, H. 2025. High-efficiency removal of rare earth elements from acid mine drainage by microbially induced carbonate precipitation process. *Journal of Water Process Engineering*, vol. 71, pp. 107134. https://doi.org/https://doi.org/10.1016/j.jwpe.2025.107134

Lin, X., Qu, Z., Chen, Y., Jin, R., Su, T., Yu, Y., Zhu, S., Huo, M., Peng, J., Wang, Z. 2019. A novel application of hematite precipitation for high effective separation of Fe from Nd-Fe-B scrap. *Scientific Reports*, vol. 9, no. 1, pp. 18362. https://doi.org/10.1038/s41598-019-54896-3

Liu, J., Ji, M., Qin, J., Zhu, J., Zhu, S. 2023. Catalytic Performance of Fe-Rich Sludge in Pyrolysis of Waste Oil Scum as Volatiles and Magnetic Char. vol. 15, no. 14, pp. 2637. https://www.mdpi.com/2073-4441/15/14/2637

München, D.D., Veit, H.M. 2017. Neodymium as the main feature of permanent magnets from hard disk drives (HDDs). *Waste Management*, vol. 61, pp. 372-376. https://doi.org/https://doi.org/10.1016/j.wasman.2017.01.032

Omodara, L., Pitkäaho, S., Turpeinen, E.-M., Saavalainen, P., Oravisjärvi, K., Keiski, R.L. 2019. Recycling and substitution of light rare earth elements, cerium, lanthanum, neodymium, and praseodymium from end-of-life applications - A review. *Journal of Cleaner Production*, vol 236, pp. 117573. https://doi.org/https://doi.org/10.1016/j.jclepro.2019.07.048

Önal, M.A.R., Borra, C.R., Guo, M., Blanpain, B., Van Gerven, T. 2017. Hydrometallurgical recycling of NdFeB magnets: Complete leaching, iron removal and electrolysis. *Journal of Rare Earths*, vol. 35, no. 6, pp. 574-584. https://doi.org/https://doi.org/10.1016/S1002-0721(17)60950-5

Piyawit, W., Sawananusorn, P., Srikhang, L., Buahombura, P., Akkarapattanagoon, N., Patcharawit, T., Khumkoa, S. 2018. Selective Extraction and Recovery of Rare Earth Metals (REMs) from NdFeB Magnet Grinding Sludge. Extraction 2018, Cham.

Rabatho, J.P., Tongamp, W., Takasaki, Y., Haga, K., Shibayama, A. 2013. Recovery of Nd and Dy from rare earth magnetic waste sludge by hydrometallurgical process. *Journal of Material Cycles and Waste Management*, vol 15, no. 2, pp. 171-178. https://doi.org/10.1007/s10163-012-0105-6

Rahman, M., Slemon, G. 1985. Promising applications of neodymium boron Iron magnets in electrical machines. IEEE *Transactions on Magnetics*, vol. 21, no. 5, pp. 1712-1716. https://doi.org/10.1109/TMAG.1985.1064113

Suiyi, Z., Xin, L., Minglin, Z., Yingzi, L., Siwen, L., Kaung, H.O., Weilu, Y., Wensheng, Q., Temuujin, J., Yang, Y., Jiancong, L., Wenjing, L., Yu, C. 2025. Hydrometallurgy recycling of heavy metals from electroplating sludge: Recent development and challenge. *Chemical Engineering Research and Design*, vol. 214, pp. 269-280. https://doi.org/https://doi.org/10.1016/j.cherd.2024.12.035

Torresan, V., Guadagnini, A., Badocco, D., Pastore, P., Muñoz Medina, G.A., Fernàndez van Raap, M.B., Postuma, I., Bortolussi, S., Bekić, M., Čolić, M., Gerosa, M., Busato, A., Marzola, P., Amendola, V. 2021. Biocompatible Iron–Boron Nanoparticles Designed for Neutron Capture Therapy Guided by Magnetic Resonance Imaging. vol. 10, no. 6, pp. 2001632. https://doi.org/https://doi.org/10.1002/adhm.202001632

Vander Hoogerstraete, T., Blanpain, B., Van Gerven, T., Binnemans, K. 2014. From NdFeB magnets towards the rare-earth oxides: a recycling process consuming only oxalic acid [10.1039/C4RA13787F]. *RSC Advances*, vol. 4, no. 109, pp. 64099-64111. https://doi.org/10.1039/C4RA13787F

Wang, Y., Sun, B., Gao, F., Chen, W., Nie, Z. 2022. Life cycle assessment of regeneration technology routes for sintered NdFeB magnets. *The International Journal of Life Cycle Assessment*, vol. 27, no. 8, pp. 1044-1057. https://doi.org/10.1007/s11367-022-02081-6

Warren, D.M. 1995. Neodymium iron boron and professional audio loudspeakers. *The Journal of the Acoustical Society of America*, 98(5_Supplement), pp. 2871-2871. https://doi.org/10.1121/1.413157

Yadav, J., Sarker, S.K., Bruckard, W., Jegatheesan, V., Haque, N., Singh, N., Pramanik, B.K. 2024. Greening the supply chain: Sustainable approaches for rare earth element recovery from neodymium iron boron magnet waste. *Journal of Environmental Chemical Engineering*, vol. 12, no. 4, pp. 113169. https://doi.org/https://doi.org/10.1016/j.jece.2024.113169

Zakeri, A., Tafaghodi, L. 2025. A Review of the Current Progress in High-Temperature Recycling Strategies for Recovery of Rare-Earth Elements from Magnet Waste. *Journal of Sustainable Metallurgy*. https://doi.org/10.1007/s40831-025-01010-9

Zhihan, Z., Dong, W., Chenghao, L., Wang, Z., Wanhai, X., Guoyu, Q., Guobiao, L. 2022. New insight into oxidative roasting and leaching for NdFeB waste. *Journal of Environmental Chemical Engineering*, vol. 10, no. 6, pp. 108946. https://doi.org/https://doi.org/10.1016/j.jece.2022.108946 ◆

Seismic hazard associated to mine planning strategies: A novel application of the Gutenberg Richter distribution and the extreme value theory illustrated in a deep mine case study

by J. Jarufe[1], L. Alfaro[1], E. Rubio[2], C. Morante[3], C. Gómez[4], R. Cuba[4]

Affiliation:
1 Universidad de Santiago de Chile, Chile
2 Redco Santiago, Chile
3 Redco Lima, Peru
4 Compañia Minera Raura, Peru

Correspondence to:
J. Jarufe

Email:
juan.jarufe@usach.cl

Dates:
Received: 03 Jan. 2025
Revised: 23 Mar. 2026
Accepted: 05 Jul. 2026
Published: Aug. 2026

How to cite:
Jarufe J., Alfaro, L., Gómez C., Cuba R. Rubio E., Morante C. 2026. Seismic hazard associated to mine planning strategies, A novel Applications of the Gutenberg Richter Distribution and the Extreme Value Theory Illustrated in a Deep Mine Case Study. *Journal of the Southern African Institute of Mining and Metallurgy*, vol. 126, no. 8, pp. 455 – 466

DOI ID:
https://doi.org/10.17159/2411-9717/3638/2026

ORCiD:
J. Jarufe
https://orcid.org/0000-0003-2373-785X
C. Gómez
https://orcid.org/0009-0005-6061-4965

Abstract

The increasing global demand for metals compels the mining industry to optimise production methods and planning to meet rising needs. However, as mining operations extend deeper, the risks associated with mining-induced seismicity and rockburst hazards become more critical. Effectively managing mining rates is essential for controlling induced seismicity and mitigating these risks.

This paper presents a novel and practical methodology for integrating seismic hazard considerations into mine production planning. By analysing historical seismic and mine production data, the methodology develops actionable guidelines for addressing short-term planning challenges. In contrast to traditional reliance on unwritten miner experience or time-intensive numerical modelling solutions, this approach offers a streamlined and timely framework for decision-making.

The proposed framework is applied to a case study of a Peruvian polymetallic mine utilising the sublevel stoping method with backfill. The results demonstrate the methodology's ability to optimise short-term operational decisions, striking a balance between production efficiency and safety standards, and highlighting its potential for broader application in the mining industry.

Keywords

Seismicity, mine planning, seismic hazard, rockburst

Introduction

The relationship between the volume of extracted rock and induced seismicity is a fundamental aspect of assessing the geomechanical effects of mining operations. As mining activities intensify and progress to greater depths, the frequency and magnitude of seismic events tend to increase, underscoring the need for a comprehensive understanding of the underlying mechanisms.

The extraction of rock alters the stress distribution within the surrounding geological structures. This redistribution of stress can trigger the reactivation of pre-existing faults (Potvin et al., 2010) or induce the formation of new fractures. These changes may result in seismic events that range from minor tremors to significant fault displacements, particularly in proximity to critical underground infrastructure.

A thorough understanding of the interplay between mined volume and seismicity is crucial for developing robust mitigation strategies. Such strategies aim to ensure operational safety, minimise the risk of damage to infrastructure, and maintain the long-term stability of mining operations.

Stress changes resulting from mining activities are inherently complex and influenced by multiple factors, including the depth of extraction, the chosen mining method, geological conditions, and the mining rate. Deeper mining operations are associated with more pronounced seismicity due to the elevated stress conditions characteristic of greater depths.

Mining methods that involve large-scale rock removal, such as block caving, typically cause significant stress redistributions when compared to more controlled methods like open stoping or room-and-pillar mining (Wagner, 2019; Wang et al., 2009). Furthermore, the mechanical properties of the surrounding rock mass are critical; brittle rocks, in particular, are more susceptible to sudden failure, potentially triggering seismic events (An, Mu, 2024).

Effective management of induced seismicity in mining environments involves a combination of real-time monitoring, predictive modelling, and engineering controls. Seismic monitoring networks are essential for detecting and analysing seismic events, providing valuable data that can be used to adjust mining operations and mitigate risks (Mendecki 2023). Additionally, understanding the relationship between mined volume and induced seismicity allows for the development of predictive models that can forecast seismic events based on mining activities and stress changes (Martinsson et al., 2020; Das Jennifer et al., 2022; Khalil et al., 2022). By integrating these approaches, mining companies can better manage the risks associated with induced seismicity, ensuring safer and more sustainable operations.

Mine planning and seismic hazard

The mine planning design process is a critical engineering stage that defines the appropriate mining units, such as stope size, block caving undercut area, and pillar size, as well as the rate at which the mine will be extracted. These two factors are closely related, as the size of the mining units and supporting infrastructure will determine the rate at which material can be drawn from the mine. Additionally, the mine must produce a predefined amount of ore to meet the capacity of the processing plant, ensuring the mine and plant operate at full production without bottlenecks in the overall process.

The mine plan design process begins with an initial approach generated by the planning department, which is guided by factors such as mineral grade distributions, the economic value of the mine sequence, and empirical geotechnical design guidelines. These guidelines include methods for determining stope dimensions, pillar design, and the minimum required cave area. While these empirical techniques help control the geometry of the excavations and pillars to achieve the desired production rate, they do not consider the potential for seismic activity and rockburst hazards. To address these risks, rock mechanics engineers analyse the planning sequence using numerical modelling and provide feedback to the mine planning team, leading to modifications of the initial design to mitigate the identified hazards that could not be evaluated using the standard empirical tools.

While the resulting mine sequence has the geotechnical and economical backup to satisfy project needs, it is common that during the operational stage of the mine, where the final results from the planning-geotechnical design are being implemented into the mine, some changes to the accepted planning scheme had to be made. These are usually related to unforeseen conditions such as variations in ore grades, geotechnical conditions or operational factors such as low availability of mining equipment among other reasons. All of these situations generate changes in the mine sequence that cannot always go through a detailed rock mechanics review due to the extensive response times that geotechnical analysis requires.

Based on the previous discussion, it would be more useful to the planning department to have design tools to allow the generation of planning decisions based on the expected seismic response of the rockmass.

Rockburst and seismic activity are inherent consequences of extensive mining deep underground (Cook, 1976). The relationship between mining activities and seismicity has been well-established through numerous historical examples from mining regions around the world. In the Upper Silesia mines in Poland and the Brezove Hoty district in Czechoslovakia, the rockburst phenomenon has been extensively studied and documented, with researchers elaborating on the relationships between extracted rock volume and seismicity (Gibowicz, 1963; Gibowicz, Kijko, 1994; McGarr, 1976; Głowacka, Kijko, 1989; Glowacka, 1993; Vatcher et al., 2019). These studies have demonstrated the inherent connection between the intensity of mining operations and the resulting seismic events (Figure 1), highlighting the need for careful planning and management to mitigate such risks.

In South Africa, the mining industry has a long history of dealing with seismic hazards, which have been extensively researched and documented (Cook, 1976; McGarr, 1976; Ortlepp, 1997; Gibowicz, Kijko, 1994), where the inherent relationship between mining and seismicity was recognised not only on the energy released but also in the temporal distribution of seismicity after blasting (Cook, 1976).

The relationship between mining activities and seismic hazards has been well-documented in Canadian mines as well. Hasegawa et al. 1989 and Blake and Hedley (2003) reviewed several case studies of rockbursts in Canadian mines, concluding that high extraction ratios were often associated with large seismic events and rockbursts.

For example, in the Sudbury mining district of Ontario, Canada, a long history of seismic events and rockbursts has been observed. The Creighton Mine, one of the deepest mines in the region, has experienced numerous seismic events over the years, some of which have resulted in significant damage and fatalities. Researchers have attributed these seismic events to the high extraction ratios and the deep, high-stress mining environment. Similarly, in the Timmins mining camp of northern Ontario, the Hollinger and McIntyre mines have also grappled with seismic hazards. These mines, which operated at depths exceeding 2,000 metres, experienced numerous rockbursts that were linked to the high stresses induced by the extensive underground excavations. An example of this relationship can be seen in Figure 2, where increases in the occurrence of rockbursts (continuous black line) is related to increments of the mined tonnes (dashed line).

Quantitative relationships between mined rock and seismic hazard were established by Glowacka and Kijko (1989), where the seismic energy (commonly used in Polish mines) was found to be directly proportional to the volume of rock extracted, following Equation 1.

$$\sum E = C * \Delta V^{B} \quad [1]$$

Where ΣE corresponds to the expected seismic energy, ΔV is the extracted rock volume, C and B are constants dependent of rockmass conditions.

The results from Equation 1 represent the most likely energy release value for a given volume of extracted rock. However, the authors suggest considering a normal distribution around the

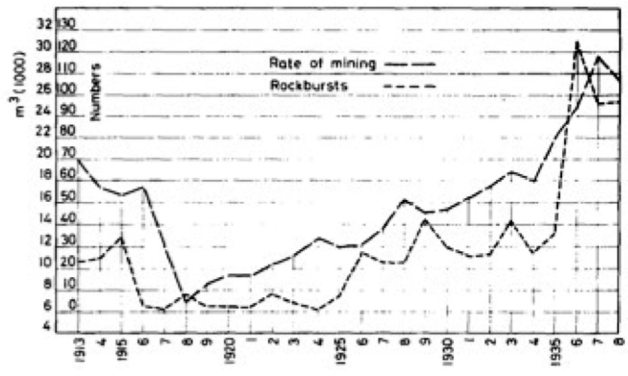

Figure 1—Relationship between rockburst incidence and mined volume for the Brezove Hoty mine district in Czechoslovakia (Cook, 1976)

calculated seismic energy (ΣE) value to account for the inherent variability in mining-induced seismic events. Following this concept, the probability P(Ej) of a seismic event with energy greater than a specific threshold P(ΣE > Ej) can be calculated using the cumulative normal distribution function, as shown in Equation 2. This quantitative relationship between mined rock volume and seismic hazard offers mine planners a valuable tool to incorporate seismic risk assessment into the mine planning process.

$$P(E_j) = 1 - \left(\frac{1}{\sigma\sqrt{2\pi}}\right) \int_0^{E_j} e^{-\frac{1}{\sigma^2}(E-\Sigma E)^2} dE \qquad [2]$$

A more in-depth analysis on the relationship between mining and seismicity is provided by Mendecki and Lötter (2011) and Mendecki (2013), where it is proposed to express seismic hazard in terms of the extracted rock volume or, as the "inter-event expected volume" defined as the average volume mined to produce a seismic event above certain size. This method in conjunction with the Gutenberg and Richter (1956) relationship allows the calculation of the probability of experiencing a seismic event with a seismic potency (Mendecki 2016) greater than a specific value for a given inter-event extracted rockmass volume (Figure 3).

The results from the method proposed by Mendecki and Lotter (2011) and Mendecki (2013) describe the probability of experiencing a seismic event based on the available data and the corresponding Gutenberg and Richter (GR) model. Since the same GR model can be present infinite realisations, the distribution of the maximum values of each realisation can be modelled through the extreme value theory, where the probability that a magnitude x will be the largest among n independent samples from a random variable X with distribution F(x) is given by Gibowicz and Kijko (1994), Mendecki (2016), and Wesseloo (2020):

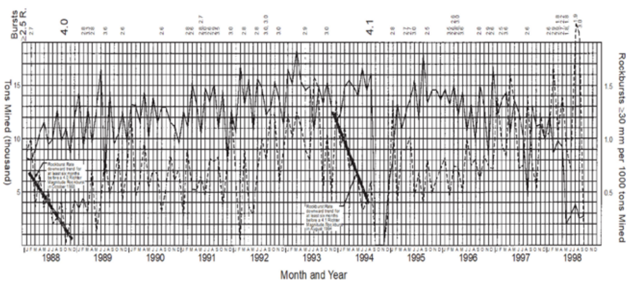

Figure 2—Seismicity and blasted volume (tonnes) in Lucky Friday Mine (Blake, Hedley. 2003)

$$F_{max}(x) = P(X_1 \leq x, X_2 \leq x, \ldots, X_n \leq x) = [F(x)]^n, \qquad [3]$$

The results from Equation 3 provide a probabilistic outcome from the GR model, as shown by Mendecki (2016) in Figure 4.

Creating empirical mine design guidelines

The previous section described methods to calculate seismic hazard based on the GR parameters. Also, it was established that in many mine operations a relationship between mined volume and seismicity can be determined, as shown in Figure 1 and Figure 2. Finally, as discussed previously, a method to evaluate the seismic hazard based on mine planning alternatives would improve short-term decision in mine planning and also be an improvement in the design process since the beginning of the design.

In the present work, a method to evaluate and compare the seismic hazard of different mine planning scenarios is proposed and discussed. The mine planning scenarios correspond to different monthly mining rates and the seismic hazard is calculated based on past induced seismic history.

To evaluate seismic hazard associated with a planning option there are several steps that need to be completed, corresponding to the relationship between mining and seismicity, the amount of total seismicity generated by each mine plan scenario and the evaluation of the seismic hazard for each plan. These steps are detailed in the following section, and illustrated through a case study later in this paper.

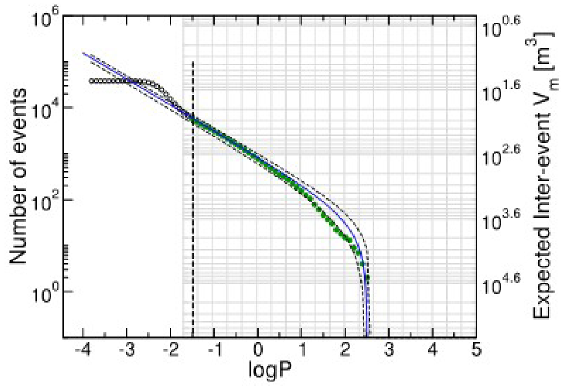

Figure 3—Frequency magnitude relationship with Gutenberg and Richter model and seismic potency (Log P) linked to the inter-event extracted volume on the right vertical axis (Mendecki, Lotter, 2011)

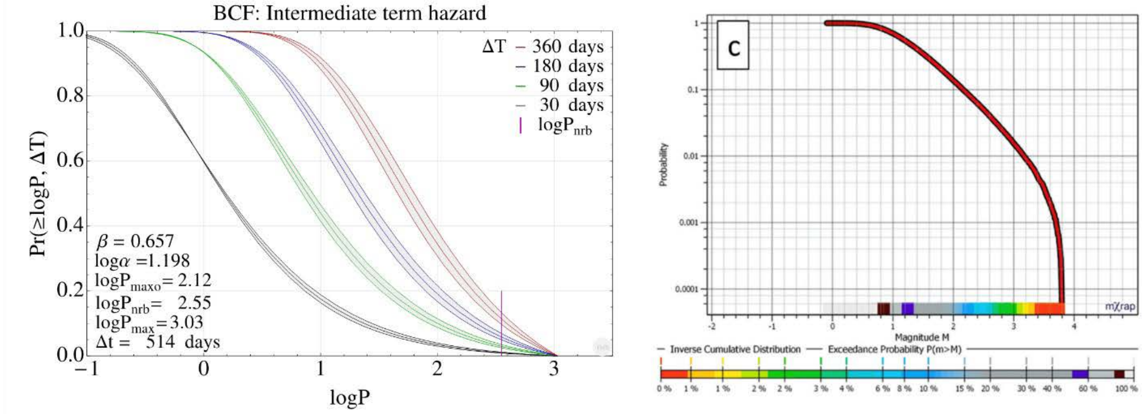

Figure 4—Seismic hazard estimation based on the GR parameters and the extreme value theory. Left: probability of exceeding a specific Log P value (Mendecki, 2016) Right: probability of exceeding a specific moment magnitude (Jarufe et al., 2022)

Identify failure mechanism associated with the future mine scenarios

As described by Hudyma and Potvin (2010) and in Hudyma (2010) (Figure 5), different mine environments react differently to the mine excavations, but also, variations in the mine sequences generate a different seismic response even for the same rockmass (Orlecka-Sikora et al., 2012; Malovichko, 2020). Of course, this occurs because of the different stress distribution caused by the different mine sequences. For the methodology considered in this paper, it is necessary to identify different failure mechanism domains, which may be defined by rockmass conditions or by the applied mining method.

Relationship between mined volume and seismicity

In this step, a relationship between mined rock volume and induced seismicity is established. Since seismic moment, representing the deformation at the seismic source, has been considered as one of the most reliable parameters (Glazer, 2016), it will be considered in this paper, however seismic potency (Mendecki, 2013) or apparent volume (Van Aswegen, Butler, 1993) can also be utilised. The relationship between mined volumes and seismicity can be calculated from the mine's existing data or utilising benchmarked values as the ones described by Vallejos and McKinnon (2011) or Mendecki (2012) among others (Figure 5).

It is important that, as described in the previous sections, relationships between mined volume and seismicity are based on the same rupture mechanism, considering a zonification of the seismic response domains to perform this analysis.

Calculate total seismicity for different mine planning scenarios

Applying the relationship between seismic response and mined volume, the total seismicity generated by different planning scenarios can be calculated. The planning scenarios are usually expressed as different daily production schemes in different mine sectors, however, to calculate the seismic hazard it is necessary to calculate the seismic moment associated to each planning scenario. This step is illustrated in Figure 7, where the mining rate for different stope scenarios, as described by Viljoen et al. (2021) has to be transformed into a monthly seismic moment for each planning scenario.

Develop probabilistic hazard model associated to each planned scenario

The total seismic moment is a representation of the total seismic deformation related to a specific mining scenario. This deformation does not occur as a single rupture but as a family of ruptures with an exponentially distributed failure radius, which is equivalent to a set of synthetic seismic events that, in total, generate the same fracturing as the total seismic moment calculated in the aforementioned step . The procedure to develop the synthetic distribution of events is described in Jarufe et al. (2022) but basically consists of generating a set of exponentially distributed seismic magnitudes of which the sum is equivalent to the total calculated seismic moment. This is done through an error minimisation procedure easily carried out with Excel Solver. Once the synthetic seismic data is generated, a and b values can be calculated and the Mmax distribution can be calculated as described through Equation 3 (Gibowicz, Kijko, 1994; Wesseloo, 2020).

The result from this methodology is the probability that the maximum magnitude will exceed a specific value, for each mine planning option.

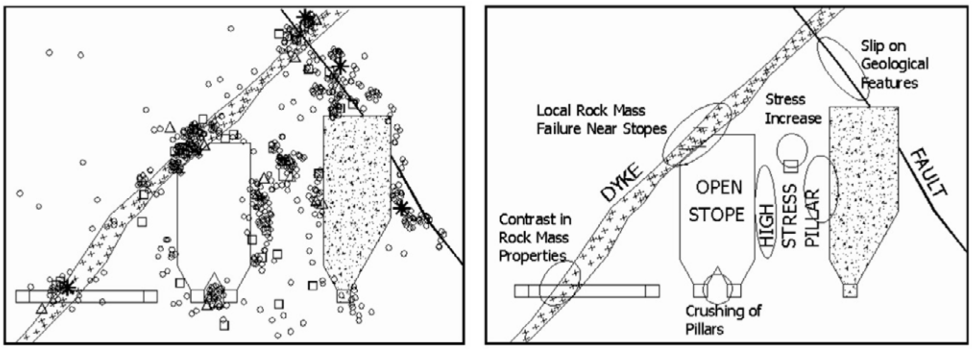

Figure 5—Different source mechanism around stope mines (Hudyma, 2010)

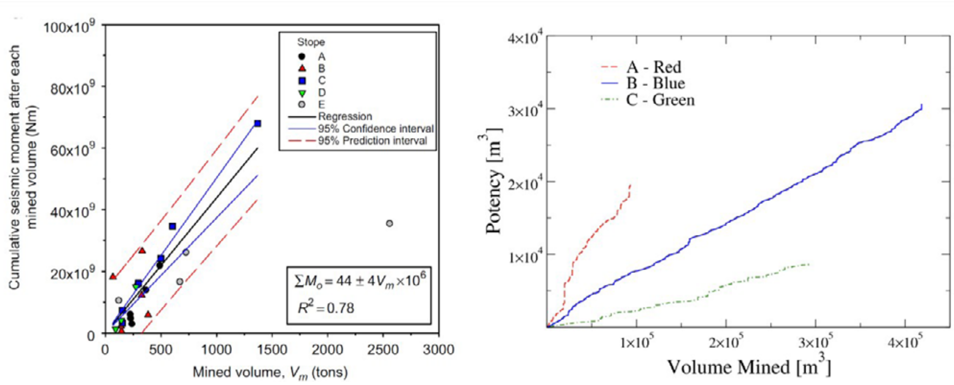

Figure. 6—Relationship between mined volume and seismic moment for Canadian mines (Vallejos, McKinnon, 2011) and mined volume with potency for South African mines (Mendecki, 2013)

The previous methodology will be illustrated through a case study of Raura mine in Peru, which during its deepening process faced relevant seismic events of increasing frequency as well as instabilities detected near blast sites. Faced with this situation, an analysis was done on the seismic rupture mechanisms, which can affect the deposit and the relationship between short-term production and rockmass seismic response.

Case study, open stope Raura mine 2023 backanalysis

Background information

Location and geological context

Raura mine is located in the Oyón district, 181 km northeast from the city of Lima, capital city of Peru. Geographically, the Raura mine lies on the peaks of the Raura Range, forming part of the watershed between the Pacific basin rivers and the Atlantic basin rivers, at a height ranging from 4300 to 5700 metres above sea level.

The Raura mining deposit has had a long industrial trajectory from colonial times with mine prospecting work along silver veins. Beginning in 1928, the mine underwent intense exploration until 1961, at which time the Compañía Minera Raura S.A. began its operations. The current plant capacity is 2,880 t/day.

The geological context of the Raura deposit is preceded by various geological events that took place within a complex structural framework, involving multiple tectonic repetitions. The Raura deposit is a skarn with polymetallic characteristics (Cu-Zn-Pb-Ag), and the mineral occurrences are associated with porphyritic stock of possible Miocene age and Cretaceous sedimentary units associated with the principal fault directions (Figure 8).

Mineralisation in veins is probably associated with a NE-SW longitudinal faults' direction, which have led to shear zones. The mineralisation has only moved to fill in faults with a NEE direction, because at the moment of mineralisation, the direction of maximum stress was NEE and the transversal fault jumps have not been played as extensional, but as transcurrent. In any case, mineralisation has circulated along the transversal faults, but the open spaces were small, and deposits have only been isolated or non-continuous. Silver, zinc, and copper appeared in lesser quantities, with more lead and zinc content in minerals towards the south (Figure 9).

The mine can be subdivided into three sectors: the Catuva zone located in the central part, which has several sectors that have already been mined; the Esperanza zone in the north, which includes several small-volume satellite structures; and the Hadas zone, which is the sector with the greatest reserve volume, the deepest sector, and where mining currently takes place.

Rockmass characteristics

The rock mass quality in various mineralised and sterile zones is assessed using diamond core samples, which include records of quality parameters for the rock mass. These records support geomechanical classifications such as the Bieniawski RMR and Barton's Q system. Additionally, geotechnical mapping across different zones evaluates rock mass quality and minor structural features (REDCO, 2021).

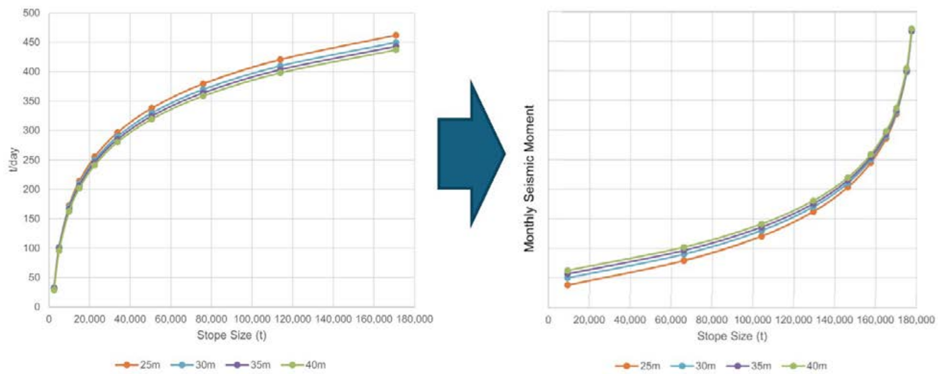

Figure. 7—Example of daily mined tonnes for different stoping options (as described by Viljoen et al., 2021) converted to an estimation of the seismic moment estimation for each planning scenario

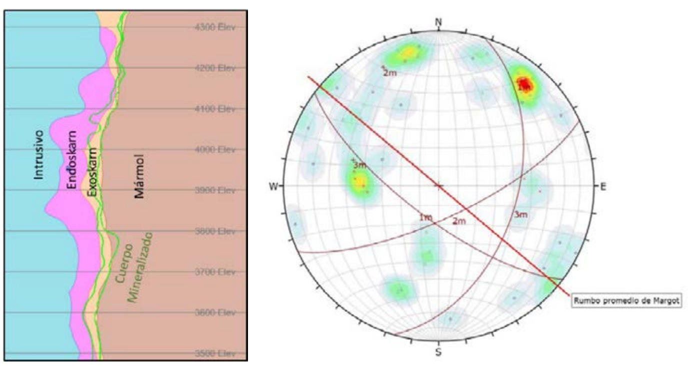

Figure. 8—Structural map of the Raura mining unit

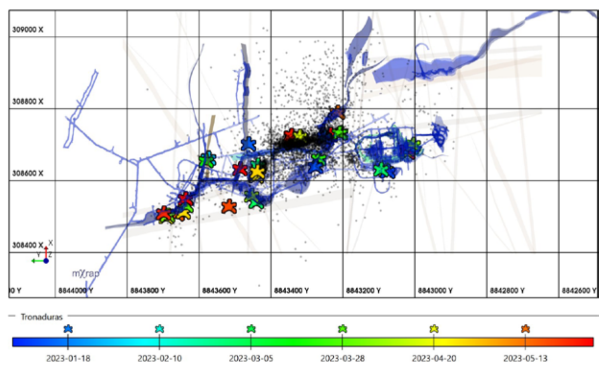

Figure 9—Plan view of the mineralised structures in the Raura mining unit. Dots indicate seismic events and stars corresponds to blast locations

To characterise the sectors of the Raura mine, the area can be subdivided into four distinct sectors according to Barton's classification (Figure 10). The Sur Alta zone comprises rock of fair to poor quality; the Norte Alta zone contains rock of fair to good quality; the Sur Baja zone features rock of fair to poor quality; and the Norte Baja zone includes rock of fair quality. It is noteworthy that the transition between the Alta and Baja zones occurs approximately at the 4100 elevation, while the boundary between the Sur and Norte zones varies gradually and is not defined by any specific structure. Seismicity is primarily observed within the mineralised bodies, likely due to mining operations activating pre-existing lithological and structural contacts within the mine.

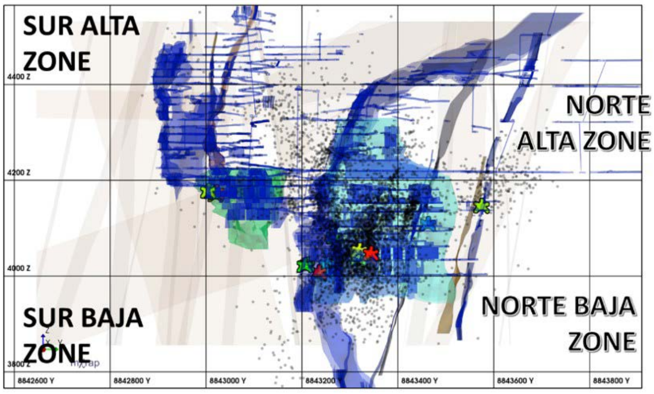

Figure 10—Raura geotechnical domains

Approximately 50 uniaxial rock tests were conducted to assess the strength characteristics of the rock samples, including intrusive, volcanic, porphyric, and limestones. The results of these tests showed a range of uniaxial compressive strength values, varying between 85 MPa and 120 MPa. This range indicates a moderate to high strength for the rock samples.

Mining method

Raura mine uses different mining methods depending on the geotechnical conditions. When the mineralised veins have low thickness (< 6m) and dipping up to 50°, bench and fill method is used (Figure 11a) for thicker sub vertical veins, pastefill stopes are considered, whereafter primary stopes are mined they are paste filled and secondary stope extraction occurs (Figure 11b).

Stress conditions derived from numerical modelling

Numerical finite element stress models have been developed and calibrated through back analysis in specific sectors of the mine where stress damage on excavations has been observed. This process enables the visualisation of stress anisotropy, as illustrated in Figure 12. Calibration results indicate that the induced principal stresses $\sigma 1$ and $\sigma 3$ are oriented with an azimuth of 130°, perpendicular to the tunnel direction in the evaluated section (Figure 12). The principal stress $\sigma 1$ exhibits a plunge of 65°, resulting in minor to moderate damage to the structural bending located on the eastern side of the excavation. This enhanced understanding of stress distribution is crucial for improving the design and safety of mining operations.

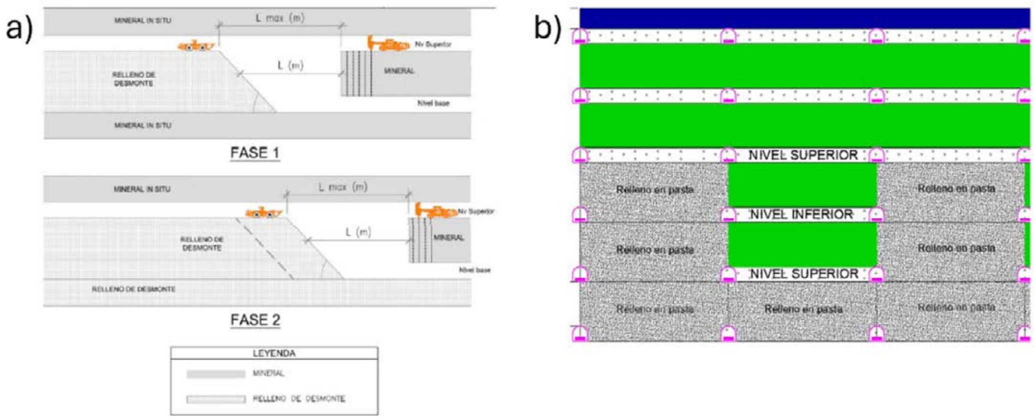

Figure 11—Mining methods used in Raura mine. a) Bench and fill method, b) paste-filled stopes for sub- vertical veins (REDCO, 2021).

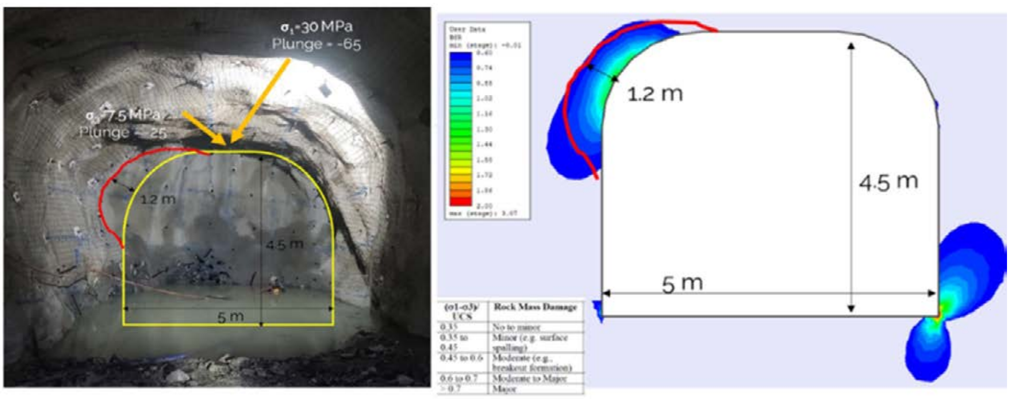

Figure 12—Principal stress calibration using 3D mine scale numerical modelling

This calibration of principal stresses was integrated into a comprehensive 3D global model of the mine, simulating the already mined and backfilled zones to determine the current induced stress conditions. The model also simulates the life of mine (LOM) mining sequence to predict future induced stress conditions according to the mining plan.

The magnitude of the maximum principal stress at the current mining levels, which are located between elevations 4000 and 4100, ranges from 24 MPa to 32 MPa in areas farther from the excavations. In contrast, in areas adjacent to the openings, the stress magnitudes range from 32 MPa to 40 MPa, as shown in Figure 12, which represents the Vanesa sector.

According to empirical rockburst assessment methods (Zhou et al., 2018, He et al., 2023) based on the maximum tangential stress and the intact rock strength, like the Russenes (1974) or Hou et al. (1992), the rockburst potential varies from medium to strong intensity.

When seismicity can be correlated with the volume of rock extracted in each productive blast, controlling the extracted volume can effectively manage seismic risk. In such scenarios, the extraction of rock induces stress intensification and redistribution around the opening. The excess stress generated must be dissipated to achieve a stable equilibrium within the rock mass. This dissipation occurs through brittle plastic failure manifested in the mine as induced seismicity and induced damage. Once the excess stress is fully dissipated, seismicity ceases. To correctly associate blasting and seismicity it is necessary to correctly define the seismic response associated with each blast, for each seismogenic domain.

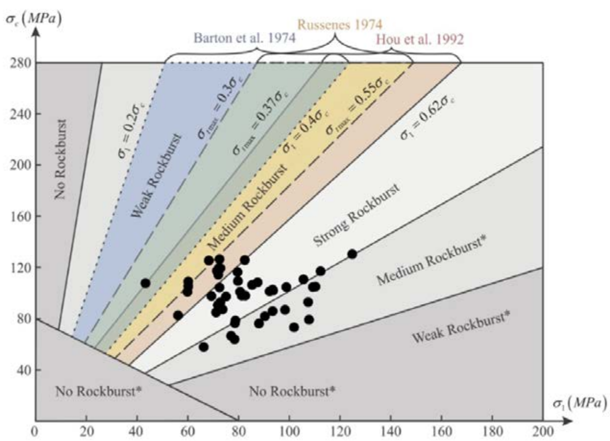

Figure 13—Empirical evaluation of rockburst potential based on the criteria proposed by Russenes (1974) and Hou et al. (1992) (Modified from Zhou et al., 2018)

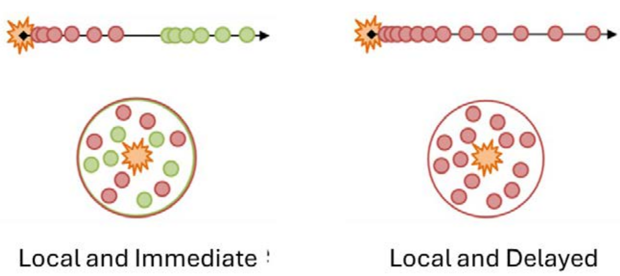

Figure 15—Graphical description of local-immediate and local-delayed seismic response, with a time scale in the upper part of the figure and a spatial diagram in the bottom part (modified from Woodward and Wesseloo, 2015)

Method application

Seismic source mechanism and relationship with mined volume

Because of the diversity of seismic responses (and mechanisms) observable in the Raura mine, it is necessary to differentiate different sectors based on the seismic response characteristics observed and their relation to mine production.

The definition of the failure mechanism

When seismicity is directly related to blasting, it is possible to generate a relation between the metric tonnes extracted and the seismic deformation, represented here by the cumulative seismic moment, which also allows one to obtain a seismic rate as a function of production. In this case, one can obtain the seismic moment generated (Nm) per metric tonne of rock extracted (t).

To achieve this relation, it is fundamental to consider blasts and seismicity for a rock volume with characteristic seismic responses. This is because there are zones in the massif with a strong seismic response, while others do not generate seismicity, together with intermediate situations. It is necessary to identify these zones to achieve a positive relation between seismicity and production. This selection of analysis volumes is grounded in three fundamental aspects:

Spatial location

Spatial groupings of events tend to be associated with the same rupture mechanism, which physically occurs in a position within space. This spatial location may be local and immediate after blasting, but also can be delayed after blasting, as described by Woodward and Wesseloo 2015, where it is identified that these seismic responses are related to the stress distributions after blast and to the aftershocks after large induced seismic events, as shown in Figure 15.

Source mechanism from Gutenberg-Richter model

After isolating a rupture mechanism, the seismic events of the frequency-magnitude relationship must align according to the Gutenberg-Richter model. Deviations from this linearity arise because different rupture mechanisms are being considered in the database, making a temporospatial subdivision necessary (Figure 16).

Seismic moment/production ratio

When mine production information is available with location, tonnage, and extraction dates, we seek to define a volume with the greatest correspondence between tonnage extracted and seismicity generated. Figure 17 shows an example of three zones used for this study, segregating the blasts and seismicity of each volume. It should be mentioned that the best volume segregation for analysis is achieved after an iterative process, where initial volumes are selected but are then modified as a function of the previously described steps, seeking the best relation between mining and seismicity in compromise with the geological characteristics of the deposit and the seismic events' locations.

Within each of these zones, we calculate the cumulative tonnes and compare them with accumulated seismic moment, making it likely that a similar response will arise in both behaviours. If the

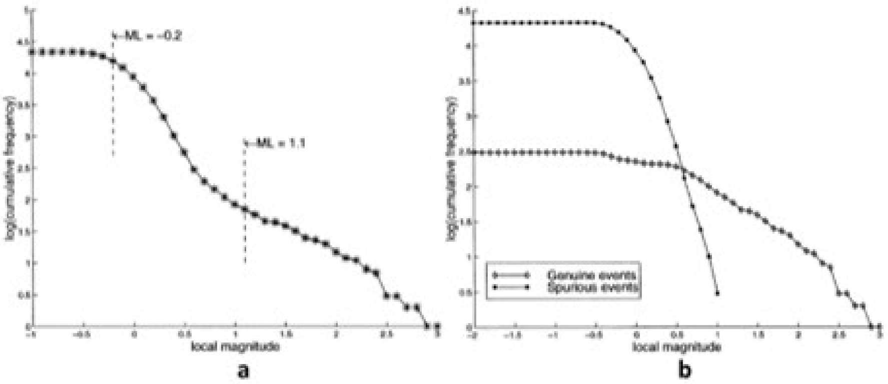

Figure 16—Example of mixed source mechanisms (a) and decomposition into two different frequency magnitude curves, one for each mechanism. Note that mixed mechanisms do not show a linear behaviour but isolated mechanism do behave linearly (After Woodward and Tierney, 2017)

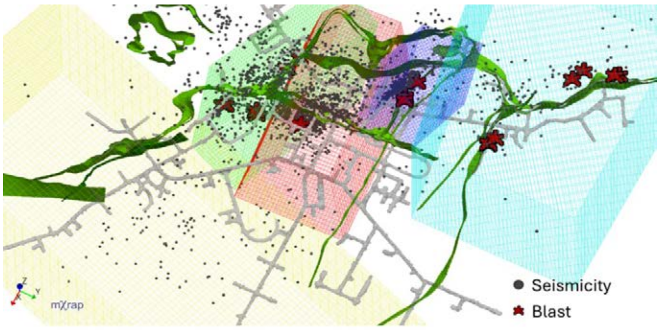

Figure 17—Example of several control volumes considering blasts and induced seismicity

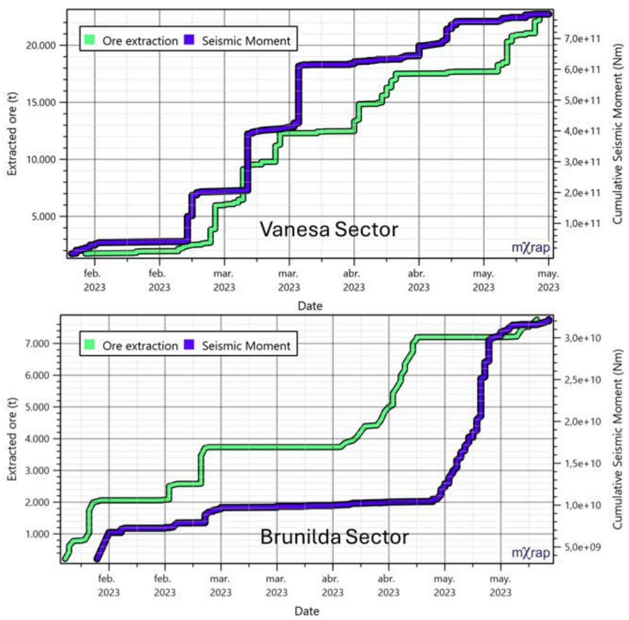

Figure 18—Example of temporal evolution within the Vanessa and Brunilda sectors: green line is production for each sector; blue line indicates cumulative seismic moment

response is not equivalent, the analysis volume must be redefined. To illustrate, we show the Vanessa and Brunilda sectors (Figure 18), indicating that cumulative seismic moment (blue line) increasing in close relation with blasting (green line).

Based upon this type of analysis, it is possible to obtain a linear relation between production in tonnes and seismic moment within

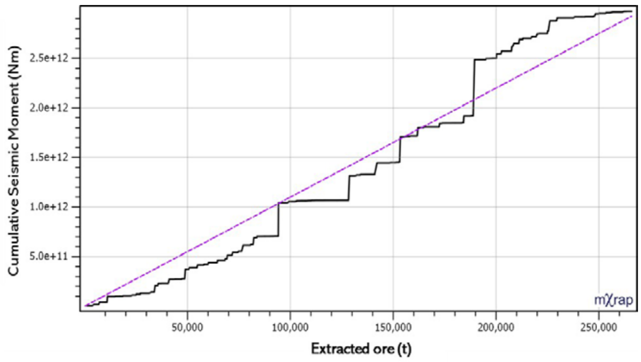

Figure 19—Relationship between seismic moment and extracted ore for all of Raura mine. This procedure has been replicated for all different seismogenic domains

the zone, which can be obtained for each mine sector. To illustrate, Figure 19 shows the relation obtained for the entire mine (all production vs all seismicity), obtaining the constants which define the line, so that:

$$MoEst = a + mP_{Min} \quad [4]$$

Where:

MoEst: Seismic moment (in Nm) estimate for a given production plan.

Pmin: mine production in tonnes.

a: Empirical constant for the line equation.

m: Empirically obtained slope of the linear trend.

When Equation 4 is defined for each control volume, one can obtain the production/seismicity relation for each sector, which can be shown as continuous lines, as indicated in Figure 20. This can be compared with historic information from mines in Canada (circles) and Australia (points) on the same graph, where one can conclude that only the Vanessa sector has a relatively high seismicity level.

The previously defined seismogenic domains (control volumes with distinctive characteristics) indicate that in the Raura mine, for the analysed timeframe, there are 4 sectors with a distinctive seismic behaviour (Hadas, Brunilda, Margot, and Vanesa). This characterisation of seismic behaviour is based on the inspection of the following seismic parameters:

For the current mine conditions, results show sectors with considerably low b-values, associated with high displacement in discontinuities (Wesseloo, 2014), particularly in reverse faults and

Table 1
Seismic characteristics measured based on recorded seismicity and current mine production

Seismogenic domain	b value (Gutenberg Richter)	Probability of seismic events greater than 2	Probability of events greater than 1 outside blasting hours	Seismic moment (Nm) per metric tonne extracted
Vanesa	0.85	46%	12%	36.000
Brunilda	1.0	5%	5%	3.100
Total mine	0.81	12%	15%	11.000

Table 2
Total expected momentum magnitude for each proposed seismogenic domain

	Monthly production (t)					Seismogenic domain
	100	1000	3000	5000	15000	
Total expected moment magnitude	0.3	0.9	1.3	1.4	1.7	Vanesa
	-0.2	0.5	0.8	1	1.3	Margot
	-0.4	0.2	0.5	0.7	1	Hadas
	-0.1	0.6	0.9	1.1	1.4	All mine

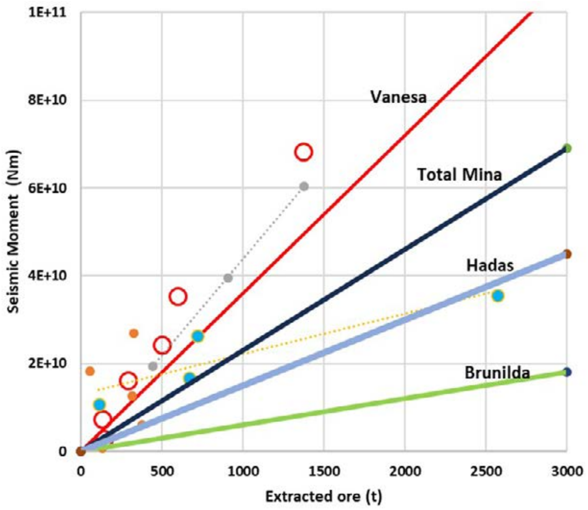

Figure 20—Relation between seismicity and mining for various productive sectors in the Raura mine

strike-slip faults (Vallejos, Estay, 2018), which can be associated with blocks displacement towards the interior of the generated cavities, as described in other cases worldwide by Linzer et al. (2020). Seismic events' time distribution also indicates that they mostly occur very close to blasting times, which is typical for a stress redistribution process after excavation. Given these elements, and considering the principal seismic rupture mechanisms accepted within the mining-induced seismicity area (Gibowcz, Kijko, 1994; Hoffman, Sheepers, 2011; Sjöberg et al., 2012; Potvin et al., 2010; Jarufe, 2020), one can conclude that seismicity in Raura is caused by the excavation-induced stresses, which mobilise structural planes near the open stopes, taking advantage of the loss of confinement by the excavations and the free face, which is generated in order to generate seismic rupture in the planes of pre-existing structural systems and mobilising blocks towards the volume generated by the open stopes, therefore timing backfill and limits to excavation rates should apply to assess seismic risk at Raura.

Calculate total seismicity for different mine planning scenarios

From the leftmost column in Table 1, one can calculate the amount of total seismic deformation (expressed as seismic moment) for a specific blasted in situ rock volume. In this exercise, several mine exploitation scenarios will be evaluated considering different monthly mining rates (Table 2).

The total co-seismic deformation is calculated for each planning scenario; however, since the total seismic moment for each scenario can be an unfamiliar value for most of rock mechanics and planning practitioners, the total seismic moment will be transformed to an equivalent moment magnitude following the relation proposed by Hanks and Kanamori (1979) where:

$$M_{We} = \frac{2}{3} * \log(Mo) - 6.01 \qquad [5]$$

Where Mwe is the equivalent moment magnitude and Mo the total seismic moment released during the period considered in the mine plan scenario. Following this idea, Mwe is a moment magnitude equivalent to all the ruptures that occur during one mining period (one month in this case). The equivalent moment magnitude for all the planning scenarios on the different seismogenic domains can be seen in Table 2.

The equivalent magnitude from Table 2 represents the total co-seismic deformation occurring during a one-month period, as a single equivalent seismic event. This situation may be practical to get an order of magnitude of the seismicity occurring in each mining scenario, but real seismicity occurs as a series of several hundreds of exponentially distributed seismic events with an inverse cumulative distribution described by the GR relationship. This GR relationship for each mining scenario is the base for the seismic hazard calculation described in Equation 3, leading to the calculation of the probability that the maximum event will exceed a specified magnitude.

Develop probabilistic hazard model associated with each planned scenario

The probabilistic distribution of the largest expected events, described in Equation 3 is based on the GR parameters obtained from the frequency magnitude relationship. To evaluate the seismic hazard for different planning scenarios, GR parameters need to be estimated based on the available data. In this case, b-value (related to source mechanism) is obtained from current seismic data and the a-value (related to the number of events) is obtained utilising the method described by Jarufe et al. (2022) where a simplex optimisation algorithm is utilised to calculate values that generate a distribution of seismic events that are equivalent to the Mwe for each planning scenario.

Following this method, the probability distribution of the largest event occurrence, for each planning scenario is calculated, as illustrated in Figure 21 where the GR distribution is plotted (black line) and the probability distribution of the largest expected magnitude is shown as a coloured line on the right axis.

The previous procedure produces the complete exceedance probability of the possible largest event, however, for most mines it is only necessary to evaluate the probability of exceeding only specific magnitudes. In this case study, we carry out the comparison with the existing energy dissipation capacity in current developments, allowing us to evaluate whether the proposed mining plan generates seismic events, which can be contained by the current support system, or if additional investment is needed for supports to avoid potential block collapses, which can impede mining operations and harm workers. The magnitude of interest corresponds to 0.5, which is related to a medium risk level according to the mine experience; 2.0, corresponding to a high risk according to the mine experience; while 2.5 is an extreme magnitude. While the probabilities can be calculated for each seismogenic domain, only the global mine seismic hazard will be presented in this illustrated example, considering the annual probability of exceeding a specific magnitude for a specific monthly production rate, as shown in Figure 22.

With the probabilistic data on maximum magnitude for each plan in each sector, we can carry out the comparison with the existing energy dissipation capacity in current developments, allowing us to evaluate whether the proposed mining plan generates earthquakes, which can be contained by the current system or if additional investment is needed in supports to avoid potential block collapses, which can impede mining operations and harm workers.

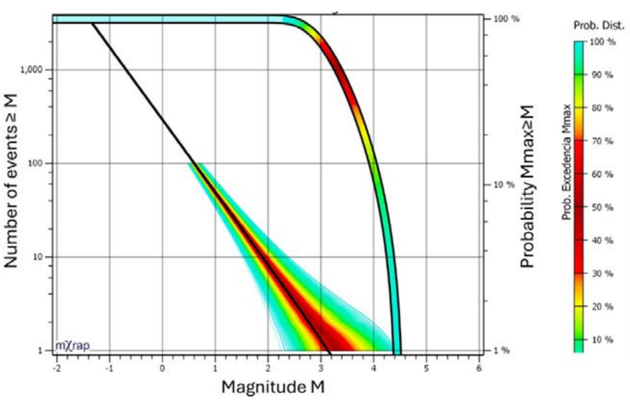

Figure 21—Probabilistic distribution of extreme magnitudes for one of the planning scenarios

Analysis and further work

This paper presents a method to evaluate the seismic hazard of different mining rates. While the evaluation of seismic potential has already been proposed by several authors, the practical relationship between a probability of exceeding a specific seismic magnitude associated with a mining plan has never been addressed directly. It is important to note that this paper addresses the seismic event occurrence, which does not necessarily become a rockburst. Therefore the probability of experiencing a rockburst will be lower than the results from this method. The method presented in this paper provides valuable insights regarding at which maximum rates each sector should be mined, and also provides guidelines to avoid areas without backfill. Furthermore, the use of mitigation techniques to reduce the rockburst consequences, as yielding support, post blast exclusion zones or rockmass preconditioning will reduce the rockburst probability even more.

Conclusions

This study has demonstrated a methodology for leveraging historical production and seismicity data from a mining operation to establish guidelines for mining rates and extraction strategies. The goal is to ensure operations are conducted within an acceptable risk level for the company. By applying extreme value theory and the classic Gutenberg-Richter relationship, the seismic hazard was probabilistically assessed. This approach was exemplified through a real-world application at the Raura mine in Peru.

We trust this methodology will be applied to other mining methods to further validate its utility, enabling the development of mining practices in a safe environment for workers while enhancing the economic value of mining operations.

Acknowledgments

The authors of this work would like to thank the Peru and Chile branches of REDCO and the Raura Mining Company for allowing this study to be published. Thanks is also due to the University of Santiago for funding.

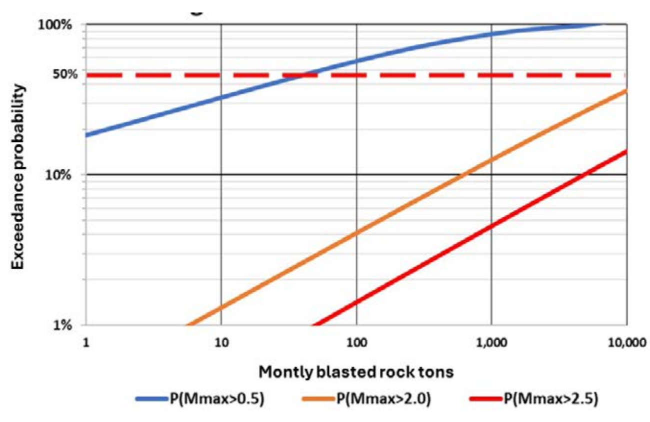

Figure 22—Exceedance probability for magnitudes 0.5, 2, and 2.5 for different monthly mining rates. This chart represents the average behaviour of the whole mine; however, specific charts for each seismogenic domain are recommended

References

An, H., Mu, X. 2024. *Contributions to Rock Fracture Induced by High Ground Stress in Deep Mining*: A Review. Rock Mech Rock Eng (2024). https://doi.org/10.1007/s00603-024-04113-z

Blake, W., Hedley, D.G. 2003. Rockbursts: case studies from North American hard-rock mines. Littleton: SME.

Cook, N. G. W. (1976). Seismicity associated with mining. *Engineering Geology*, vol. 10, no. 2-4, pp. 99-122. https://doi.org/10.1016/0013-7952(76)90015-6

Das Jennifer, P., Porchelvan, P., Naik, S.R. 2021. Numerical modelling of mining induced seismicity in deep closed mines: A case study. In International Conference on Geotechnical Challenges in Mining, Tunneling and Underground Infrastructures pp. 437-455. Singapore: Springer Nature Singapore.

Gibowicz, S. 1963. Magnitude and energy of subterrane shocks in Upper Silesia. *Studia Geophysica et Geodaetica*, vol.7, pp.1-37. https://doi.org/10.1007/BF02607768

Gibowicz, S.J., Kijko, A. 1994. *An Introduction to Mining Seismology*. Warsaw: Academic Press.

Glazer, S. N. (2016). *Mine Seismology: Data Analysis and Interpretation. Palabora Mine Caving Process as Revealed by Induced Seismicity*. New York: Springer International.

Glowacka, E. 1993. Probabilistic Seismic Hazard Evaluation in Underground Mines. *Natural Hazards*, vol. 7, no. 2, pp. 121-132.

Głowacka, E., Kijko, A. 1989. Continuous evaluation of seismic hazard induced by the deposit extraction in selected coal mines in Poland. In S. J. Gibowicz (Ed.), *Seismicity in Mines* pp. 523-533. Basel: Birkhäuser Basel.

Gutenberg, B., Richter, C.F. 1956. *Magnitude and Energy of Earthquakes. Nature*, pp. 176, 795. https://doi.org/10.1038/176795a0

Hanks, T.C., Kanamori, H. 1979. A moment magnitude scale. *Journal of Geophysical Research: Solid Earth*, vol. 84, (B5), pp. 2348-2350. https://doi.org/10.1029/JB084iB05p02348

Hasegawa, H.S., Wetmiller, R.J., Gendzwill, D.J. 1989. Induced seismicity in mines in Canada—an overview. *Pure and Applied Geophysics*, vol. 129, pp. 423-453. https://doi.org/10.1007/BF00874518

He, M., Cheng, T., Qiao, Y., Li, H. 2023. A review of rockburst: Experiments, theories, and simulations. *Journal of Rock Mechanics and Geotechnical Engineering*, vol. 15, no. 5, pp. 1312-1353.

Hou, F., Liu, X., Wang, M. 1992."Discussion on rockburst origin and degree." Proceedings of the 3rd Academic Conference on National Rock Dynamics. Technical University of Surveying and Mapping Press, Wuhan. 1992.

Hudyma, M. 2010. Applied Mine Seismology Concepts and Techniques. Technical notes for ENGR 5356. Mine Seismic Monitorting Systems, Laurentian Universtity

Hudyma, M., Potvin, Y.H. 2010. An Engineering Approach to Seismic Risk Management in Hardrock Mines. *Rock Mechanics and Rock Engineering*, vol. 43, pp. 891–906 (2010). https://doi.org/10.1007/s00603-009-0070-0

Jarufe, J. 2020. Fault slip seismicity in underground mining operations: asperity and barrier shear modelling. PhD Thesis, The University of Western Australia.

Jarufe, J., Perez, S., Hurtado, J.P., Cifuentes, C. 2022. Seismic hazard calculation using the equivalent magnitude obtained from numerical modelling. *International Journal of Rock Mechanics and Mining Sciences*, vol. 153, pp. 105081. https://doi.org/10.1016/j.ijrmms.2022.105081

Khalil, H., Chen, T., Xu, Y.H., Mitri, H. 2022. Effect of mining and geology on mining-induced seismicity–A case study. *Journal of Sustainable Mining*, vol. 21, no. 3, pp. 5. https://doi.org/10.46873/2300-3960.1361

Linzer, L.M., Hildyard, M.W., Spottiswoode, S.M., Wesseloo, J. 2020. Do stopes contribute to the seismic source? The Southern African Institute of Mining and Metallurgy, vol. 120, no. 1, pp. 81–90. http://doi.org/10.17159/2411-9717/954/2020

Malovichko, D. 2020. Description of seismic sources in underground mines: Theory. *Bulletin of the Seismological Society of America*, vol. 110, no. 5, pp. 2124-2137. https://doi.org/10.1785/0120200093

Martinsson, J., Törnman, W. 2020. Modelling the dynamic relationship between mining induced seismic activity and production rates, depth and size: a mine-wide hierarchical model. *Pure and Applied Geophysics*, vol. 177, no. 6, pp. 2619-2639. https://doi.org/10.1007/s00024-019-02378-y

McGarr, A. 1976. Seismic moments and volume changes. *Journal of Geophysical Research*, vol. 81, no. 8, pp. 1487-1494. https://doi.org/10.1029/JB081i008p01487

Mendecki, A.J. 2012. Size distribution of seismic events in mines. In Proceedings of the Australian Earthquake Engineering Society 2012 Conference, Queensland pp. 1-20.

Mendecki, A.J. 2013. *Characteristics of seismic hazard in mines*. 8th International Symposium on Rockbursts and Seismicity in Mines pp. 275-292, Russia.

Mendecki, A.J., Lötter, E.C. 2011. *Modelling seismic hazard for mines*. Australian Earthquake Engineering Society Conference pp. 18-20, Barossa Valley, South Australia.

Mendecki, A.J. 2016. Mine Seismology Reference Book, Seismic Hazard. Published by Institute of Mine Seismology.

Mendecki, A.J. 2023. Seismic ground motion alerts for mines. Journal of Seismology, vol. 27, no. 4, pp. 599-608.

Orlecka-Sikora, B., Lasocki, S., Lizurek, G., Rudziński, Ł. 2012. Response of seismic activity in mines to the stress changes due to mining induced strong seismic events. International Journal of Rock Mechanics and Mining Sciences, vol. 53, pp. 151-158. https://doi.org/10.1016/j.ijrmms.2012.05.010

Ortlepp, W.D. 1997. Rock Fracture and Rockbursts-An Illustrative Study. Monograph Series/South African Institute of Mining and Metallurgy.

Potvin, Y., Jarufe, J., Wesseloo, J. 2010. Interpretation of seismic data and numerical modelling of fault reactivation at El Teniente, Reservas Norte sector. *Mining Technology,* vol. 119, no. 13, pp. 175–181. https://doi.org/10.1179/174328610X12820409992453

REDCO. 2021. Reporte Tecnico, Dimensionamiento de Unidades Básicas de Explotación. Internal Report.

Russenes, B.F. 1974. Analysis of Rock Spalling for Tunnels in Steep Valley Sides (in Norwegian). Master's Thesis, Norwegian Institute of Technology, Department of Geology, Norway, 247.

Sjöberg, J., Perman, F., Quinteiro, C., Malmgren, L., Dahnér-Lindkvist, C., Boskovic, M. 2012. Numerical analysis of alternative mining sequences to minimise potential for fault slip rockbursting. Mining Technology, vol. 121, no. 4, pp. 226-235.

Vallejos, J.A., Estay, R.A. 2018. Seismic parameters of mining-induced aftershock sequences for re-entry protocol development. Pure and applied geophysics, vol. 175, pp. 793-811.

Vallejos, J.A., McKinnon, S.D. 2011. Correlations between mining and seismicity for re-entry protocol development. International Journal of Rock Mechanics and Mining Sciences, vol. 48, (no. 4, pp. 616-625.

Van Aswegen, G., Butler, A. 1993. Applications of quantitative seismology in South African gold mines. Rockbursts and seismicity in mines, vol. 93, pp. 261-266.

Vatcher, J., Boskovic, M., Sjöberg, J. 2019. Production-associated risk factors of seismicity in the Kiirunavaara mine. MGR 2019: Proceedings of the First International Conference on Mining Geomechanical Risk pp. 261-272, Perth.

Viljoen, N., Buss, B., Lafleur, C. 2021. Stope Dimension Evaluation Tool (SDET). CIM Conference, Canada.

Wagner, H. 2019. Deep mining: a rock engineering challenge. *Rock Mechanics and Rock Engineering*, vol. 52, pp. 1417-1446.

Wang, G., Kaiser, P.K., Vasak, P. 2009. Modeling of mining-induced seismicity migration. *ROCKENG09: Proceedings of the 3rd CANUS Rock Mechanics Symposium*, Toronto.

Wesseloo, J. 2014. Evaluation of the spatial variation of b-value. *The Journal of The Southern African Institute of Mining and Metallurgy*, vol. 114, no. 10, pp. 823–828.

Wesseloo, J. 2020. Addressing misconceptions regarding seismic hazard assessment in mines: b-value, Mmax, and space-time normalization. Journal of the Southern African Institute of Mining and Metallurgy, vol. 120, no.1, 67-80.

Woodward, K.R., Tierney, S.R. 2017. Seismic hazard estimation using databases with bimodal frequency–magnitude behaviour. In UMT 2017: Proceedings of the First International Conference on Underground Mining Technology (pp. 219-232). Australian Centre for Geomechanics.

Woodward, K., Wesseloo, J. 2015. Observed spatial and temporal behaviour of seismic rock mass response to blasting. *Journal of the Southern African Institute of Mining and Metallurgy*, vol. 115, no. 11, pp. 1044-1056.

Zhou, J., Li, X., Mitri, H.S. 2018. Evaluation method of rockburst: state-of-the-art literature review. Tunnelling and Underground Space Technology, vol. 81, pp. 632-659. https://doi.org/10.1016/j.tust.2018.08.029 ◆

Metallurgical bottlenecks in artisanal gold cyanidation: The impact of mercury amalgamation on percolation vat leaching

by O.P. Oladijo[1], V. Moyo[1], G. Danha[1], C. Lebudi[1]

Affiliation:
[1]Department of Chemical Materials and Metallurgical Engineering, School of Earth Sciences and Engineering, Botswana International University of Science and Technology, Palapye, Botswana

Correspondence to:
O.P. Oladijo

Email:
oladijop@biust.ac.bw
seyiphilip@gmail.com

Dates:
Received: 26 Jun. 2025
Revised: 29 Nov. 2025
Accepted: 27 Mar. 2026
Published: Aug. 2026

How to cite:
Oladijo O.P., Moyo V., Danha G., Lebud C. 2026. Metallurgical bottlenecks in artisanal gold cyanidation: The impact of mercury amalgamation on percolation vat leaching. *Journal of the Southern African Institute of Mining and Metallurgy*, vol. 126, no. 8, pp. 467 – 474

DOI ID:
https://doi.org/10.17159/2411-9717/3757/2026

ORCiD:
O.P. Oladijo
https://orcid.org/0000-0003-1650-6244
V. Moyo
https://orcid.org/0009-0004-1622-9616
G. Danha
https://orcid.org/0000-0001-6853-8112
C. Lebudi
https://orcid.org/0000-0001-7946-4788

Abstract

Percolation vat leaching offers mid-tier artisanal and small-scale gold mining a practical compromise between heap and agitated tank systems. However, the common practice of sequentially using mercury amalgamation and cyanidation causes severe metallurgical and environmental failures. This review demonstrates that static artisanal and small-scale gold mining vats suffer critical oxygen starvation, triggering cascading geochemical hazards. Residual elemental mercury (Hg0) acts as an aggressive reagent sink, rapidly exhausting localized cyanide to generate highly mobile, toxic mercury-cyanide complexes. Concurrently, oxygen depletion retards sulphide ore oxidation, precipitating elemental sulphur (S0) and polysulfides that passivate the native gold surface. To mitigate these bottlenecks, this paper proposes low-complexity interventions: solid oxygen-release compounds (CaO2), hypochlorite pre-oxidation, and trace lead nitrate to sequester sulphur. Ultimately, equipping fabricators and policymakers with this empirical data is crucial; formalising the sector requires the absolute decoupling of amalgamation from cyanidation and a transition toward modular, mercury-free vat systems.

Keywords

Artisanal and small-scale gold mining, percolation vat leaching, cyanidation, amalgamation, geochemical passivation, hydrometallurgy

Introduction

Gold extraction remains a cornerstone of the global economy, particularly in mineral-rich developing regions across Southern Africa. Traditionally, the academic and industrial focus has been directed towards large-scale, formal mining operations that utilise highly optimised, continuous processing circuits involving gravity separation, flotation, and agitated tank cyanidation. However, a massive proportion of global gold output is currently driven by the artisanal and small-scale mining (ASGM) sector (Perks, et al., 2025). Because this sector operates largely within the informal economy, it relies on fundamentally different, low-cost extraction methods (Lay, Tafese, 2024). The choice of downstream processing technology is therefore not just a matter of ore mineralogy, but also a direct reflection of an operations scale, capital, and regulatory oversight.

Within this context, gold cyanidation via percolation vat leaching occupies a critical middle ground. Unlike heap leaching, which commonly treats run-of-mine or coarsely crushed ore over long irrigation cycles, percolation vat leaching generally processes finer crushed or milled material in a contained batch vessel. This finer feed improves gold liberation and solid–liquid contact, allowing potentially higher recoveries and shorter leach times than coarse-ore heap leaching, while avoiding the higher capital expenditure and energy demands of agitated tanks. Consequently, vat leaching has become a dominant chemical extraction method for mid-tier and small-scale operators. While it is a metallurgically viable technique when strictly controlled, its informal and unregulated application present severe operational and environmental challenges. In countries such as Zimbabwe, vat leaching is frequently applied to tailings that have already been processed with mercury (PACT, 2015; Tychsen, 2022).

Formalising the ASGM sector and eliminating mercury use requires both high-level policy and on-the-ground engineering solutions. The United Nations Environment Programme (UNEP) provides the critical international guidelines for reducing mercury reliance (UNEP, 2021). To practically implement these environmental goals, organisations such as PACT strongly advocate for the local manufacturing of safe, alternative extraction equipment (PACT, 2015). However, stimulating local equipment manufacture is practically impossible without a deep, fundamental understanding of the actual processes involved. Local engineers and workshops find it difficult to safely design, scale, or optimise percolation vats without a thorough understanding of the underlying fluid mechanics, mass transfer limitations, and geochemical reactions that dictate the extraction.

While existing literature thoroughly covers the optimised routes of formal industrial gold production, there is a distinct lack of critical analysis regarding the mechanistic realities of rudimentary technologies like percolation vat leaching as they actually operate in the field. Therefore, this paper provides an in-depth technical evaluation of the ASGM vat leaching flowsheet, specifically focusing on the widespread sequential use of mercury amalgamation and cyanidation. By systematically analysing the restrictive hydrodynamics of static vats and the cascading geochemical hazards introduced by residual amalgamation tailings, most notably aggressive reagent consumption, sulphur passivation, and the formation of highly toxic, highly mobile mercury-cyanide complexes (Seney, et al., 2020), this review exposes the critical metallurgical failure points of current artisanal operations. Synthesising these technical challenges is essential in equipping local equipment fabricators, metallurgical engineers, and policymakers with the empirical foundation required to design targeted process interventions, rehabilitate legacy mine sites, and successfully transition the mid-tier ASGM sector toward safer, formalised, and mercury-free extraction practices.

Gold processing in the ASGM sector: a Zimbabwean context

The metallurgical flowsheet utilised in the artisanal and small-scale gold mining (ASGM) sector diverges significantly from formal industrial operations. Driven by capital constraints and the need for immediate economic returns, informal miners follow a hybridised extraction process that sequentially uses mercury amalgamation and percolation vat leaching. This is shown in Figure 1, which illustrates a typical gold process flow-diagram utilised by artisanal miners in Zimbabwe. The standard ASGM process is distinctly divided into primary recovery via gravity concentration and mercury amalgamation, followed by secondary recovery via percolation vat cyanidation.

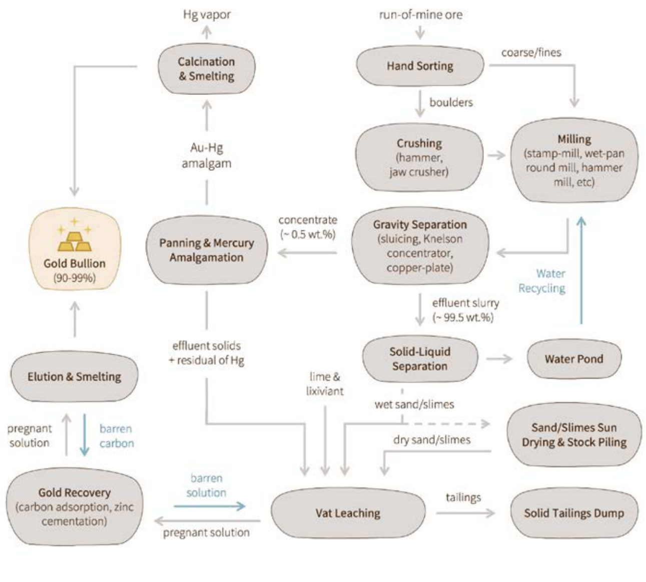

Figure 1—Standard ASGM extraction circuit in Zimbabwe, detailing the sequential integration of uncontrolled comminution, primary recovery via mercury amalgamation, and secondary recovery via percolation vat cyanidation

The process initiates with the extraction of run-of-mine (ROM) ore, which undergoes preliminary manual classification through hand sorting to remove oversized boulders. The remaining ore is then subjected to primary crushing utilising basic hammer or jaw crushers to produce a coarse-fines mixture. This crushed material is fed into secondary comminution circuits. In Zimbabwe, this stage is heavily dominated by the use of locally manufactured stamp-mills, although wet-pans, round mills, or hammer mills are also often utilised. Unlike industrial closed-circuit grinding, these rudimentary milling techniques lack precise classification, producing a slurry with a highly uncontrolled particle size distribution that often leaves fine gold partially encapsulated within the host rock.

Following milling, the ore slurry is routed to primary gravity separation. Zimbabwean miners typically utilise sluicing techniques, copper-plates, or occasionally centrifugal devices such as Knelson concentrators. This step physically splits the process stream. The vast majority of the processed material, approximately 99.5 wt.%, is discharged as an effluent slurry. The remaining heavy concentrate, which contains the liberated free-milling gold, is isolated for immediate primary recovery. This high-grade concentrate is subjected to panning and direct amalgamation with liquid elemental mercury (an older and highly environmentally damaging method). The resulting gold-mercury (Au-Hg) amalgam is manually recovered and thermally decomposed through calcination and smelting. This vaporises the mercury (releasing highly toxic Hg-vapor into the atmosphere) and yields a primary gold bullion with a purity of 90% –99%. This localised amalgamation step is, however, inefficient as panning effluents usually contain unrecovered fine gold, reactive solids, and significant droplets of residual macroscopic mercury.

To maximise total extraction, miners usually employ a secondary vat cyanidation step to process the amalgamation waste. The residual panning effluents, which are heavily contaminated with elemental mercury, are recombined with the 99.5 wt.% effluent slurry from the initial gravity separation. This combined stream undergoes basic solid-liquid separation. The recovered water is recycled back to the milling circuit via a water pond, while the resulting wet sand and slimes are diverted for preparation. Before cyanidation, these wet slimes are spread for sun drying and stockpiling, a common sight at mid-tier Zimbabwean processing centres. Once converted to dry sand/slimes, the material is manually loaded into percolation vats. An alkaline lixiviant, balanced with lime for protective alkalinity, is applied to the vat to dissolve the remaining gold. The process generates a pregnant leach solution (PLS) that is transferred to a gold recovery circuit utilising either carbon adsorption or zinc cementation, followed by final elution and smelting to produce a secondary gold bullion.

However, this specific processing introduces a significant metallurgical limitation. By recombining the panning effluents with the bulk tailings stream, residual elemental mercury is directly incorporated into the wet/dry slimes. Introducing this mercury-laden material into the static, unagitated environment of a percolation vat establishes the competing geochemical reactions and mass-transfer constraints that ultimately inhibit overall gold recovery within the ASGM sector.

Cyanidation and percolation leaching methods

Once gold is liberated from run-of-mine ore through communition, cyanidation is usually employed to dissolve it into a pregnant leach

Table 1
Comparison of industrial and artisanal cyanide percolation leaching methods

Parameter	Heap leaching	Vat leaching	Agitated tank leaching
Particle size distribution (PSD)	Coarsely crushed; fines (< 150 µm) limited to < 15% to ensure bed permeability (Peterson, Van Staden, 2025).	Moderately fine (typically ~250 µm); often utilises unclassified stamp-mill product (Veiga et al., 2009).	Fine grind; typically, 80% passing 75 µm for maximum gold liberation (Stange, 1999; Snyders et al., 2017).
Process hydraulics	Unsaturated flow: solution is applied via drip/spray and percolates through air-filled voids (Surimbayev et al., 2025).	Saturated flow: vessel is flooded, creating a stagnant environment with no internal mixing (Gonah, Makoni, 2026).	Agitated slurry: continuous mechanical mixing keeps solids in suspension for optimal contact (Ellis, Senanayake, 2004).
Lixiviant concentration	Low (0.1 – 0.6 g/L NaCN); managed for long-term, high-volume irrigation (Peterson et al., 2010).	High (above 1g/L NaCN); used to compensate for lack of agitation and poor diffusion (Veiga et al., 2009; Manzila et al., 2009; Manzila, et al., 2022).	Moderate (approx. 0.6g/L NaCN); optimised for rapid kinetics and controlled consumption (Stange, 1999; Ellis, Senanayake, 2004).
Mass transfer and aeration	Passive atmospheric diffusion through porous ore bed; slow but consistent oxygen supply (Petersen et al., 2010).	Severely restricted; oxygen supply is limited to the dissolved content of the stagnant lixiviant (Veiga et al., 2006).	High efficiency; forced aeration and mechanical turbulence maximise oxygen and cyanide transfer (Stange, 1999; Snyders, et al., 2017)
Residence time	21 – 60 days(Veiga et al., 2006).	3 – 7 days(Veiga et al., 2006; Tychsen et al., 2022).	24 – 48 hours (Veiga et al., 2006; Snyders et al., 2017).
Gold recovery	35 – 65% (Veiga et al., 2006).	45 – 70% (Veiga et al., 2006).	Above 90% (Veiga et al., 2006).
Operational context	Preferred for large-scale, low-grade deposits with high porosity.	Common in mid-tier ASGM due to low CAPEX and moderate footprint (John, 2011).	Standard for high-grade or refractory ores requiring intensive processing and high CAPEX/ OPEX (John, 2011).
Environmental impact	High risk of solution containment failure affecting ecosystems; generates massive permanent waste-rock dumps (Ghorbani et al., 2015)	Severe ecological risks including mercury-cyanide co-contamination, land degradation, and waterway siltation (Mukono et al., 2018; Tychsen et al., 2022).	Lower long-term liability; standard circuits incorporate dedicated cyanide detoxification prior to tailings disposal (Demopoulos, Cheng, 2004).

solution (PLS). This process has remained the global industry standard for both ASGM and industrial gold mining for over a century due to its efficiency and relative selectivity (Marsden, House, 2006; Adams, 2016). Although some artisanal miners still rely solely on direct mercury amalgamation, cyanidation has become increasingly dominant within the informal sector to extract residual values. Cyanide solutions are exceptionally effective leaching agents due to their ability to form stable water-soluble gold-cyanide complexes, specifically $[Au(CN)_2]^-$ and $[Au(CN)_4]^-$ (Marsden, House, 2006). During cyanidation, a dilute alkaline sodium cyanide (NaCN) solution is used to dissolve the solid gold into the PLS, under high pH conditions and in presence of dissolved oxygen. The overall stoichiometry of this reaction is universally described by Elsner's equation (Fleming, 1992).

$$4Au(s) + 8CN^-(aq) + O_2(g) + 2H_2O(l) \rightarrow 4[Au(CN)_2]^-(aq) + 4OH^-(aq) \qquad [1]$$

Subsequent thermodynamic studies have demonstrated that this cyanidation mechanism actually proceeds through two primary stages. Initially, oxygen is reduced at the cathodic gold surface, leading to formation of hydrogen peroxide (H_2O_2) as an intermediate (Equation 2). This is followed by reduction of the hydrogen peroxide itself, which acts as a facilitator to drive further gold dissolution as described by Equation 3. (Senanayake, 2005; Senanayake, 2008).

$$2Au(s) + 4CN^-(aq) + O_2(g) + 2H_2O(l) \rightarrow 2Au^-(aq) + 2OH^-(aq) + H_2O_2(aq) \qquad [2]$$

$$2Au(s) + 8CN^-(aq) + H_2O_2(g) \rightarrow 2Au(CN)^{2-}(aq) + 2OH^-(aq) \qquad [3]$$

In industrial agitated tank cyanidation, continuous mechanical aeration ensures a steady supply of oxygen (O_2) to sustain both stages of this reaction. However, the reality is vastly different in ASGM. Because introducing active air aeration or chemical oxidants during on-site cyanidation is economically and logistically impractical for artisanal miners in remote locations, ASM vat leaching operates under severe O_2-limited conditions as it only depends on atmospheric O_2 dissolved into the ore bed. In a flooded, static percolation vat, the initial dissolved O_2 within the lixiviant solution is rapidly consumed by the first stage of the reaction mechanism (Equation 2), as well as by competing reagent sinks like residual mercury during cyanidation of amalgamation tailings. Because there is no mechanical agitation or chemical supplies to replenish O2 concentration in the vat, it (i.e., O_2 concentration) quickly falls below stoichiometric requirements, thus limiting Elsner's reaction. Consequently, the generation of the critical H_2O_2 intermediate halts, and the entire dissolution mechanism is severely hindered, leaving significant unrecovered gold in the tailings.

Ultimately, the efficiency of this two-stage gold dissolution mechanism depends on how much O_2 can be delivered to the gold metal interface. While agitated tanks actively pump air to sustain O_2 demands, static percolation in vats and heaps rely entirely on the natural permeability (hydraulic conductivity) of the ore bed, creating severe limitations in lixiviant and oxygen distribution. Because the physical design of the leaching system directly dictates these chemical kinetics, the choice of leaching equipment is critical. Depending on the ore grade, particle size distribution, and available capital, cyanidation is formally conducted using one of three primary methods: heap leaching, percolation vat leaching, or agitated tank leaching. Table 1 provides a critical technical comparison of these methods, highlighting how percolation vat leaching occupies a middle ground between the low-capital requirements of heap leaching and high-recovery rates of agitated tank leaching, justifying its wide-spread adoption in the ASGM sector (Tychsen et al., 2022).

The operational differences between heap, vat, and agitated tank leaching are primarily governed by feed particle size distribution (PSD), system hydrodynamics, and mass transfer efficiency. Specifically, heap leaching requires coarsely crushed ore to maintain bed permeability, whereas vat leaching utilises a moderately finer feed, and agitated tank systems require a fine grind to ensure the complete mechanical suspension of solids (Stange, 1999; Veiga et al., 2009; Petersen, Van Staden, 2025). This progressive reduction in particle size directly enhances both gold liberation and the available solid-liquid interfacial area. Consequently, this drives a significant reduction in necessary residence times, decreasing from 21 – 60 days in heap leaching to 24 – 48 hours in agitated tanks.

Both heap and vat leaching rely on the percolation of lixiviant through a packed, porous ore bed. The static hydrodynamic conditions in these systems inherently generates localised oxygen and pH gradients. However, these gradients diverge based on fluid saturation. While the flooded environment of vat leaching partially mitigates extreme pH gradients compared to heaps, it severely restricts the incorporation of atmospheric oxygen in the bed (Gonah, Makoni, 2026). In contrast, agitated tank systems eliminate these spatial gradients entirely through continuous mechanical mixing, which ensures a homogeneous suspension of solids and maximises mass transfer (Stange, 1999).

Despite their lower extraction efficiencies, heap and vat leaching remain strategically viable for low-grade deposits, smaller ore bodies, or regions characterised by high geopolitical risk, owing to their substantially lower capital (CAPEX) and operating (OPEX) expenditures. They frequently function as initial, low-barrier processing pathways to generate early cash flow prior to transitioning toward more capital-intensive agitated leaching circuits (John, 2011).

However, these economic advantages are offset by distinct environmental risks that depend strongly on the level of containment, reagent control, and effluent treatment incorporated into the overall flowsheet. Heap leaching presents risks associated with massive, open-air solution inventories that are vulnerable to containment failure and adjacent hydrological contamination, particularly where liner systems, solution collection ponds, and closure controls are inadequate. (Ghorbani et al., 2015). Furthermore, the widespread adoption of vat leaching within the informal ASGM sector frequently correlates with unregulated reagent handling, the co-contamination of circuits with residual mercury, and severe land degradation, including the siltation of local waterways (Tychsen et al., 2022). Conversely, the lower environmental liability commonly associated with industrial agitated tank circuits does not arise from cyanidation chemistry itself, but from the broader engineered plant context in which such circuits normally operate. Formal tank-leaching operations typically include containment systems, reagent monitoring, cyanide destruction, effluent treatment, and regulated tailings management. In principle, similar control units could be added to heap or vat leaching operations; in practice, they are rarely implemented in informal ASGM settings because of cost, weak regulation, and limited technical capacity (Demopoulos, Cheng, 2004).

Hydrodynamics and mass transfer limitations in vat systems

While industrial precious metal heap leaching utilizes controlled agglomeration to bind fine ore particles (slimes) into stable and permeable pellets, ASM operations frequently bypass this pre-treatment, leading to severe bed compaction and stratification (Bouffard, 2005; Tychsen et al., 2022). In industrial heap leaching, agglomeration with cement is fundamental to maintain structural integrity and prevent bed blinding (Bouffard, 2005). However, in the context of ASM percolation vats, such specialised equipment and binders are almost entirely absent. These vats, constructed from brick-and-mortar or high-density polyethylene (HDPE)-lined earthen ponds, behave primarily as static saturated batch reactors (Marsden, House, 2006). During the flooded holding period, the dominant limitation is not continuous bulk flow through the ore bed, but the absence of convective renewal of cyanide and dissolved oxygen. As gold, residual mercury, and reactive sulphide minerals consume these reagents locally, concentration gradients develop within the stagnant pore solution. Ore-bed permeability becomes critical mainly during vat filling, drainage, intermittent aeration, or when operators attempt to actively recirculate lixiviant through the bed to overcome these diffusion and reagent-renewal limitations.

In the absence of these industrial preparations, poor particle-size control and high slime contents reduce the hydraulic performance of the ASGM ore bed. Preferential flow and solution channelling are well established in percolating ore beds, particularly in heap leaching and other systems where solution is actively moving through a packed bed (Ghorbani et al., 2015). In a fully flooded static vat, however, the holding period is better described as a stagnant saturated system rather than a continuously flowing percolation system. Under these conditions, the dominant limitation is poor convective renewal, which allows cyanide and dissolved-oxygen gradients to develop as reagents and are consumed locally by gold, residual mercury, and reactive sulphide minerals. Channelling becomes important mainly during drainage, re-flooding, intermittent aeration, or active lixiviant recirculation, especially where high slime contents reduce bed permeability and leave fine-rich zones poorly contacted. Under drainage or recirculating conditions, preferential flow can also be aggravated by fine particles migrating downward and reducing permeability around the drainage media at the base of the vat.

To overcome these hurdles without industrial agglomerators, artisanal miners often resort to manually removing slimes before charging the vats or blending the slimes with river sand to increase porosity. While these practices improve the percolation rate, they significantly increase manual labour costs and lead to inadvertent loss of fine-grained gold typically associated with the discarded slimes (Veiga et al., 2014). Furthermore, sand blending dilutes the head grade of the material, requiring higher volumes of lixiviant for lower gold returns.

Beyond ore bed permeability, the saturated nature of the flooded vat environment imposes severe oxygen shortage, which is often the primary bottleneck in gold extraction kinetics. According to the stoichiometry of Elsner's equation (Equation 1), the dissolution of gold is an aerobic process requiring the simultaneous presence of cyanide (CN-) and dissolved O2; however, the solubility of O2 in aqueous solutions is remarkably low, typically peaking at approximately 8 mg/L – 9 mg/L under ambient conditions (Bouffard, 2005; Marsden, House, 2006). In industrial agitated tanks, this limitation is mitigated through continuous mechanical aeration or introduction of pure oxygen to maintain concentrations above required levels; however, in a static ASM vat, the dissolved O2 within stagnant waterbed is rapidly depleted upon onset of the cyanidation reaction. Because the vat is operated as a fully saturated (flooded) bed as shown in Figure 2, there is no natural atmospheric diffusion of O2 into the lower depths of the ore bed, creating an anaerobic environment where gold dissolution ceases regardless of cyanide concentrations (Kondos et al., 1996; Adams, 2016).

Consequently, the leaching process in these vats becomes strictly diffusion-controlled, where the rate of extraction is limited by the speed at which fresh, oxygenated solution can penetrate the compacted ore (Ghorbani et al., 2015). To mitigate this, artisanal miners often use extended leach times before draining the vats in order to improve recoveries. These leach cycles often involve manually (i.e., with shovels and wheelbarrows) draining the vats completely to draw atmospheric air into the dead zones of the ore bed, allowing for surface oxidation of gold particles and replenishment of oxygen levels before reintroducing the cyanide solution. While this "intermittent aeration" can theoretically improve leaching kinetics, the lack of standardised equipment and

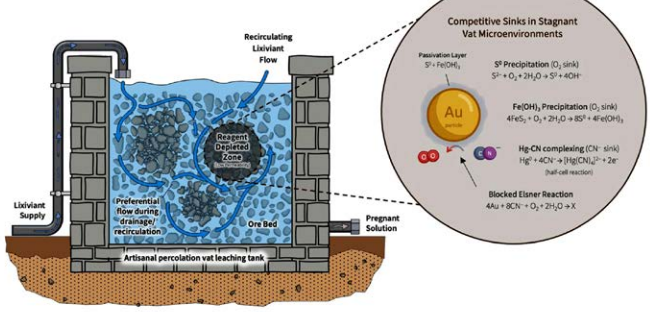

Figure 2—Schematic overview of mass-transfer limitations and geochemical failures in a flooded ASGM mercury-cyanide vat leaching system. During the static holding period, the ore bed behaves as a stagnant saturated reactor with limited convective renewal of cyanide and dissolved oxygen. Residual elemental mercury competes with gold for cyanide and oxygen, forming soluble mercury-cyanide complexes, while reactive sulphur species may contribute to surface passivation. Preferential flow becomes important mainly during drainage, re-flooding, intermittent aeration, or active lixiviant recirculation, particularly where fine-rich zones reduce bed permeability

timing in unregulated ASM sites means cycles are often too short or infrequent to overcome the mass transfer resistance (Tychsen et al., 2022). [R2.1]A more controlled approach, suggested by Manzila, et al. (2022), is bottom-to-top lixiviant recirculation, where solution is drained from the base of the vat and reintroduced at the top. If the returning stream is splashed, sprayed, or aspirated with air, recirculation can improve oxygen transfer compared with a purely static flooded system. However, this approach remains dependent on adequate bed permeability, as high slime contents may still promote preferential flow and leave fine-rich zones poorly contacted. As a result, gold particles remain in an O2-deprived state for much of the leaching duration, which explains the high amounts of unrecovered gold frequently reported in ASGM tailings (UNEP, 2021).

Geochemical hazards of the mercury-cyanide treatment sequence

The most profound technical failure and environmental risk associated with ASGM processing is the sequential use of mercury amalgamation and cyanidation. To secure immediate return, miners initially process crushed ore through gravity concentration followed by direct amalgamation with elemental mercury (Hg^0). This method leaves significant fine gold encapsulated within solid tailings, alongside residual macroscopic mercury droplets lost through poor handlings (Spiegel, Veiga, 2010). When these contaminated tailings are loaded into a cyanidation vat, the introduction of the alkaline cyanide lixiviant triggers a competitive dissolution reaction involving both gold and residual elemental mercury. Under alkaline cyanidation conditions, elemental mercury can be oxidised and complexed by cyanide according to a reaction analogous to gold cyanidation:

$$2\mathrm{Hg}(l) + 8\mathrm{CN}^-(aq) + \mathrm{O}_2(aq) + 2\mathrm{H}_2\mathrm{O}(l) \rightarrow 4[\mathrm{Hg(CN)}_4]^{2-}(aq) + 4\mathrm{OH}^-(aq) \quad [4]$$

This reaction (Equation 4) shows that residual mercury is not merely a contaminant, but a direct competitor for the same free cyanide and dissolved oxygen required for gold dissolution. In the stagnant pore solution of the flooded vat, residual mercury and reactive sulphur species introduce competing geochemical reactions that reduce reagent availability at the gold surface. Mercury acts primarily as a reagent sink through cyanide complexation, while sulphur species may contribute to surface passivation, thereby limiting effective lixiviant access to gold particles, as illustrated in Figure 2.

Interestingly, hydrometallurgical literature presents an apparent paradox regarding mercury's role in gold cyanidation. Studies have demonstrated that the presence of trace mercuric ions (Hg^{2+}) at micro-molar concentrations (10^{-5} M) can actually intensify gold cyanide leaching. At these trace levels, mercury ions prevent the formation of insoluble AuCN and $Au(OH)_x$ membranes, roughening the gold surface and catalytically enhancing dissolution rates (Li et al., 2010; Zhong et al., 2018). However, these controlled industrial findings cannot be easily extended to ASGM. While mercury concentrations can be controlled to trace levels in industrial cyanidation, the ASGM vat is flooded with massive, macroscopic quantities of unreacted elemental mercury (Hg^0) due to the prior amalgamation step. This bulk residual mercury can consume cyanide and dissolved oxygen through mercury-cyanide complexation, creating localised reagent depletion even where cyanide is added at relatively high bulk concentrations. The stagnant nature of the flooded vat does not cause mercury dissolution directly; rather, it prevents rapid replenishment of cyanide and dissolved oxygen after they have been consumed (Figure 2) (Seney et al., 2020). Consequently, gold dissolution may stall because the available reagents are preferentially consumed by mercury and other reactive species before they can effectively sustain cyanidation of the remaining gold.

The interference of reactive sulphur species

This chemical failure is ultimately finalised by the specific mineralogy of the ore. The processing of sulphide-bearing ores introduces reactive sulphur species, such as sulphide ions (S^{2-}) and polysulphides (S_n^{2-}), into the alkaline pore water. Ab-initio quantum modelling using density functional theory (DFT) reveals that the tendency of sulphur species to passivate gold is fundamentally governed by the ratio of their hydration energies to their binding energies (Zia et al., 2019). Research indicates that reactive sulphide ions, polysulphides, and sulphite (SO_3^{2-}) exhibit exceptionally strong interaction energies with the gold surface, directly contributing to the formation of passivating films.

In a well-aerated and well-controlled industrial system, reactive sulphur species may be progressively oxidised towards more stable sulphate species, depending on pH, redox potential, dissolved oxygen availability, mineralogy, and residence time (Marsden, House, 2006; Liu, Yen, 1995). However, within the static, oxygen-depleted microenvironments of an ASGM vat, this oxidation pathway is limited by poor reagent renewal and the competing consumption of oxygen by mercury and other reactive species. Under prolonged alkaline cyanidation conditions, partially oxidised sulphur species, elemental sulphur, and polysulphide-type surface species may accumulate near reactive mineral and gold surfaces. These species can chemisorb onto gold or contribute to surface films that restrict access of cyanide and dissolved oxygen, thereby slowing the Elsner dissolution reaction (Liu, Yen, 1995; Zia et al., 2019).

In a well-aerated and well-controlled industrial system, sufficient dissolved oxygen is available to progressively oxidise these reactive sulphur species into more stable sulphates (SO_4^{2-}) species, depending on pH, redox potential, dissolved oxygen availability, mineralogy, and residence time (Liu, Yen, 1995; Marsden, House, 2006). However, within the static, oxygen-depleted micro-environments of an ASGM vat, this critical oxidation step is severely retarded, which is also aggravated by both poor physical diffusion and the massive mercury reagent sink (Figure 2). Instead of oxidising fully to sulphate, the sulphide-containing ions undergo intermediate decomposition. Under prolonged alkaline cyanidation conditions, this incomplete oxidation leads to the direct precipitation of elemental sulphur allotropes (S0) and the chemisorption of polysulphide layers directly onto the anodic gold surface (Liu, Yen, 1995; Zia et al., 2019). This forms a dense, insulating film that completely covers the finely dispersed gold metal. Once this sulphur layer forms, it acts as a strict physical and electrochemical barrier, permanently blinding the gold from further contact with the cyanide lixiviant, consequently halting the Elsner reaction.

Furthermore, sulphur species with lower interaction energies with gold, such as thiosulphate ($S_2O_3^{2-}$) and thiocyanate (SCN^-), should not be treated as purely deleterious, since both can participate in gold complexation under suitable chemical conditions. Thiosulphate-based systems, in particular, are used as alternative non-cyanide lixiviants for gold. However, in an uncontrolled ASGM cyanidation circuit, their formation still indicates diversion of oxidant and sulphur chemistry away from the intended cyanide-based dissolution pathway. Without controlled pH, redox potential, reagent dosage, and solution monitoring, these species are unlikely to provide a stable and selective leaching environment comparable to engineered thiosulphate systems, and may still contribute indirectly to reduced cyanidation efficiency (Marsden, House, 2006; Zia et al., 2019).

Furthermore, even sulphur species that exhibit lower interaction energies with gold, such as thiosulphate ($S_2O_3^{2-}$) and thiocyanate (SCN^-), should not be treated as purely deleterious, since both can participate in gold complexation under suitable chemical conditions. Thiosulphate-based systems, in particular, are used as alternative non-cyanide lixiviants for gold. However, in an uncontrolled ASGM cyanidation circuit, their formation still indicates diversion of oxidant and sulphur chemistry away from the intended cyanide-based dissolution pathway. Without controlled pH, redox potential, reagent dosage, and solution monitoring, these species are unlikely to provide a stable and selective leaching environment comparable to engineered thiosulphate systems, and may still contribute indirectly to reduced cyanidation efficiency (Marsden, House, 2006; Zia et al., 2019).

ASGM technological interventions

The catastrophic failure mechanisms inherent to the artisanal percolation vat, i.e., oxygen starvation, mercury-driven reagent sinks, and sulphur passivation, cannot be resolved through simple increases in lixiviant concentration or retention time. However, transitioning the informal sector directly to capital-intensive, agitated tank leaching is rarely socio-economically feasible. Therefore, mitigating these losses requires ASGM-friendly, low-complexity technological interventions that specifically target the disrupted mass transfer and hostile geochemistry of the static vat environment.

Hydrodynamic and mass transfer optimisation

To overcome the physical oxygen starvation in static ASGM vats, interventions must improve both oxygen supply and the vat's solution flow dynamics without relying on continuous mechanical agitation. Passive or low-pressure aeration networks, such as perforated PVC pipes placed at the base of the vat prior to ore loading can dramatically improve the upward diffusion of atmospheric oxygen, however, the effectiveness of this approach depends strongly on bed permeability. Where the ore contains excessive fines or slimes, air and solution may move through preferential pathways rather than uniformly through the bed. Therefore, aeration should be coupled with feed preparation measures such as fines control, screening, blending, or low-cost agglomeration to maintain permeability. A more effective low-complexity option is bottom-to-top lixiviant recirculation with air aspiration, as suggested by (Manzila et al., 2022). In this approach, solution is drained from the base of the vat and returned to the top through a splashing, spraying, or venturi-type arrangement that entrains atmospheric oxygen into the recirculating stream. This improves reagent renewal compared with a purely static flooded system, although adequate bed permeability remains essential to prevent preferential flow and poor contact with fine-rich zones. From a chemical perspective, the use of solid oxygen-release compounds (ORC) such as alkali and alkali-earth metal peroxides offers a viable strategy for vat oxygenation. The localised addition of solid peroxides, particularly calcium peroxide (CaO_2), which is inexpensive and readily available, to the agglomerated ore bed provides a slow, sustained release of highly soluble and reactive oxygen directly into the stagnant dead-zone regions (Ball et al., 1988). Unlike direct hydrogen peroxide (H_2O_2) injection, which decomposes too rapidly in alkaline environments and presents significant handling challenges, CaO_2 bypasses the physical diffusion limitations of the static ore bed by steadily supplying oxygen to revive the stalled Elsner reaction, especially where the dead-zones occur.

However, the implementation of these oxygen-release compounds must be coupled with rigorous alkalinity control. ASGM operators frequently overdose lime (CaO or $Ca(OH)_2$) to maintain protective alkalinity and prevent the volatilisation of hydrogen cyanide gas. While controlled calcium peroxide functions as an excellent, slow-release oxidant, an excess of free calcium ions from over-liming can fundamentally alter the system's precipitation kinetics. Improper control of lime (CaO) addition can lead to the precipitation of dense CaO2 films alongside calcium carbonate ($CaCO_3$) directly onto the cathodic regions of the gold surface (Han et al., 2024). This creates a secondary physical passivation layer that negates any benefits gained from the added oxygen. Therefore, proper stoichiometric control of lime addition is strictly necessary to minimise the formation of these localised films, in order to ensure that the CaO_2 remains a beneficial dissolved oxygen provider.

Mitigating geochemical passivation through chemical pre-treatment

Addressing severe sulphur passivation requires targeted chemical interventions that neutralise reactive sulphur species before they can chemisorb onto the gold surface. One highly accessible and scalable intervention is chemical pre-oxidation using sodium hypochlorite (NaOCl). Hydrometallurgical literature on mildly refractory sulphide ores demonstrates that hypochlorite acts as a potent oxidant capable of aggressively degrading passivating sulphide films prior to cyanidation (Hasab et al., 2014). For the ASGM and mid-tier sectors, this is particularly advantageous; rather than relying on the prohibitive logistics of importing unstable industrial oxidants, sodium hypochlorite can be reliably synthesised on-site from brine or seawater via localised, pilot-scale electrolytic plants.

Flooding the vat with a hypochlorite wash prior to cyanidation may promote oxidation of reactive sulphides (S^{2-}) and polysulphides towards more stable sulphate (SO_4^{2-}) species, thereby reducing the tendency of sulphur species to passivate the gold surface. However, oxidation of reduced sulphur species to sulphate is not automatically beneficial in calcium-rich alkaline systems. Where excess Ca^{2+} is present from lime addition or calcium peroxide use, sulphate formation may promote gypsum precipitation:

$$Ca^{2+}(aq) + SO_4^{2-}(aq) + 2H_2O(l) \rightarrow CaSO_4 \cdot 2H_2O(s) \qquad [5]$$

Such precipitation could reduce bed permeability, coat reactive surfaces, or obstruct drainage media. Therefore, sulphur pre-oxidation strategies must be coupled with controlled lime dosing and small-scale vat or column trials before field implementation.

Furthermore, the controlled application of heavy-metal chemical intensifiers, such as lead nitrate ($Pb(NO_3)_2$), has been reported to reduce sulphur-related passivation during the cyanidation of some sulphide-bearing gold ores (Deschenes et al., 2000). In an ASGM context, doping the lixiviant with trace lead salts allows the lead to act as a sacrificial precipitant. As established by Deschenes, et al. (2000), under controlled alkaline leaching conditions, lead ions (Pb^{2+}) may react with dissolved sulphur species to form stable, insoluble lead sulphide (PbS), thereby reducing the availability of reactive sulphur species that can passivate the gold surface. However, $Pb(NO_3)_2$ should not be presented as an uncontrolled field additive for informal ASGM operations, because its effectiveness and environmental safety depend on controlled dosing, reagent monitoring, and effluent management. In the ASGM context, lead nitrate is therefore better considered as a potential option for formalised modular plants or controlled pilot-scale operations, rather than as a simple artisanal remedy.

Conclusion

While percolation vat leaching offers a practical transition toward higher extraction efficiencies for artisanal and small-scale gold mining (ASGM), its effectiveness in the field is heavily restricted by informal processing practices. This review highlights that the widespread underperformance of ASM vats is driven by a combination of severe mass-transfer limitations and competing geochemical reactions. Specifically, the cyanidation of amalgamation tailings introduces macroscopic elemental mercury (Hg^0) into the vat, creating a primary reagent sink that rapidly depletes localised cyanide and dissolved oxygen. This oxygen starvation is worsened by the static hydrodynamics of the ore bed. Under these oxygen-deprived conditions, reactive sulphide minerals fail to oxidise completely, resulting in the chemisorption of sulphur and polysulphide layers that physically and chemically passivate the native gold.

To improve recovery rates and mitigate the environmental toxicity of these operations, interventions must target these specific chemical bottlenecks using accessible, low-complexity technologies. Practical strategies include controlled oxygenation through solid oxygen donors such as calcium peroxide (CaO_2), improved lixiviant renewal through bottom-to-top recirculation with air aspiration, and feed preparation measures that maintain bed permeability. Chemical pre-oxidation may also help reduce sulphur-related passivation, but it must be coupled with controlled lime dosing because sulphate formation in calcium-rich systems may promote gypsum precipitation. Lead nitrate should not be treated as a simple informal ASGM additive; rather, it is better considered only for formalised modular or pilot-scale systems where reagent dosing, monitoring, and effluent management can be properly controlled.

However, chemical intensification alone is insufficient if the foundational flowsheet remains flawed. The absolute decoupling of amalgamation from cyanidation is an engineering necessity. By eliminating elemental mercury from the vat circuit and transitioning toward standardised, modular leaching systems, the mid-tier ASGM sector can move toward a more formalised, efficient, and environmentally responsible metallurgical standard. Ultimately, the successful adoption of these interventions requires more than just metallurgical proof. Future research and policy initiatives must prioritise rigorous techno-economic feasibility assessments, evaluating the critical balance between local capital expenditure, reagent supply chain logistics, and projected increases in gold recovery to ensure these intensified systems are genuinely viable for artisanal communities.

References

Adams, M. 2016. Gold Ore Processing: Project Development and Operations. Amsterdam: Elsevier.

Ball, S., Monhemius, J., Wyborn, P. 1988. The use of inorganic peroxides as accelerators for gold heap leaching. In: M. Jha & S. Hill, eds. Proceedings of Precious Metals '89. Warrendale: The Minerals, *Metals & Materials Society*, pp. 149–164.

Bouffard, S.C. 2005. Review of Agglomeration Practice and

Fundamental in Heap Leaching. *Mineral Processing and Extractive Metallurgy Review*, vol. 26, no. 3-4, pp. 233-294.

Demopoulos, G., Cheng, T. 2004. A case study of CIP tails slurry treatment: comparison of cyanide. *The European Journal of Mineral Processing and Environmental Protection*, Volume 4, pp. 1-9.

Deschenes, G. et al. 2000. Effect of lead nitrate on cyanidation of gold ores: progress on the study of the mechanisms. *Minerals Engineering*, vol. 13, no. 12, pp. 1263–1279.

Ellis, S., Senanayake, G. 2004. The effects of dissolved oxygen and cyanide dosage on gold extraction from a pyrrhotite-rich ore. *Hydrometallurgy*, vol. 72, no. 1-2, pp. 39–50.

Fleming, C. 1992. Hydrometallurgy of precious metals recovery. Hydrometallurgy, vol. 30, no. 1-3, pp. 127-162.

Ghorbani, Y., Franzidis, J.-P., Petersen, J. 2015. Heap Leaching Technology-Current State, Innovations, and Future Directions: A Review. Mineral *Processing and Extractive Metallurgy* Review, vol. 37, no. 2.

Gonah, T., Makoni, T. 2026. Some Notes on Gold Extraction: A practical Guide on Gold Processing for the African Small Scale Miner. Raleigh: Lulu Press.

Han, J. et al. 2024. Technology for Aiding the Cyanide Leaching of Gold Ores. Separations, vol. 11, no. 8, pp. 228.

Hasab, M.G., Rashchi, F., Raygan, S. 2014. Chloride–hypochlorite leaching and hydrochloric acid washing in multi-stages for extraction of gold from a refractory concentrate. *Hydrometallurgy*, vol. 142, pp. 56–59.

John, L.W. 2011. The art of heap leaching - the fundamentals. *The Southern African Institute of Mining and Metallurgy*, pp. 17–43.

Kondos, P., Griffith, W.F., Jara, J.O. 1996. The Use of Oxygen in Gold Cyanidation. Canadian Metallurgical Quarterly, vol. 35, no. 1, pp. 39–45.

Lay, J., Tafese, T. 2024. Decent Work in Global Supply Chains (Sustainable Global Supply Chains Annual Report 2024), Hamburg: Research Network Sustainable Global Supply Chains.

Li, Q. et al. 2010. Co-intensification of cyanide leaching gold by mercury ions and oxidant. *Transactions of Nonferrous Metals Society of China*, vol. 20, no.8, pp. 1521–1526.

Liu, G., Yen, W. 1995. Effects of sulphide minerals and dissolved oxygen on the gold and silver dissolution in cyanide solution. *Minerals Engineering*, vol. 8, no. 1-2, pp. 111–123.

Manzila, A.N., Moyo, T., Petersen, J. 2022. A Study on the Applicability of Agitated Cyanide Leaching and Thiosulphate Leaching for Gold Extraction in Artisanal and Small-Scale Gold Mining. Minerals, vol. 12, no. 10.

Marsden, J., House, C. 2006. The Chemistry of Gold Extraction. Littleton: Society for Mining, Metallurgy, and Exploration.

Mukono, T. et al. 2018. Strategies for sustainable gold processing in the artisanal and Small-scale mining sector in Zimbabwe, Harare: The Chamber of Mines of Zimbabwe.

PACT. 2015. A golden opportunity: Scoping Study of artisanal and small-scale gold mining in Zimbabwe, Washington: Twenty-First Century Schools.

Perks, R. et al. 2025. Achieving Sustainable and Inclusive Artisanal and Small-Scale Mining (ASM): A Renewed Framework for World Bank Engagement, Washington: The World Bank.

Petersen, J., Van Staden, P. 2025. Heap Leaching: Process, Principles, and Practical Considerations. In: Treatise on Process Metallurgy. Oxford: Elsevier, pp. 333–345.

Petersen, J., Minnaar, S., Plessis, C. d. 2010. Carbon dioxide and oxygen consumption during the bioleaching of a copper ore in a large isothermal column. Hydrometallurgy, vol. 104, 3-4, pp. 356–362.

Senanayake, G. 2005. Kinetics and reaction mechanism of gold cyanidation: Surface reaction model via Au(I)–OH–CN complexes. *Hydrometallurgy*, vol. 80, no. 1-2, pp. 1–12.

Senanayake, G. 2008. A review of effects of silver, lead, sulfide and carbonaceous matter on gold cyanidation and mechanistic interpretation. *Hydrometallurgy,* vol. 90, no. 1, pp. 46–73.

Seney, C.S. et al. 2020. Reaction of Cyanide with Hg0-Contaminated Gold Mining Tailings Produces Soluble Mercuric Cyanide Complexes. *Chemical Research in Toxicology*, vol. 33, no. 11, pp. 2834–2844.

Snyders, C., Akdogan, G., Bradshaw, S., Wyk, A.V. 2017. Gold CIP and CIL process optimization in a capital constraint environment. *Journal of the South African Institute of Mining and Metallurgy*, vol. 117, no. 8, pp. 8119–828.

Spiegel, S.J., Veiga, M.M. 2010. International guidelines on mercury management in small-scale gold mining. J*ournal of Cleaner Production*, vol. 18, no. 4, pp. 375–385.

Stange, W. 1999. The process design of gold leaching and carbon-in-pulp circuits. *The South African Institute of Mining and Metallurgy*, pp. 13–26.

Surimbayev, B. et al. 2025. Technology Development of Gold Heap Leaching in Kazakhstan: An Overview. Mineral Processing and Extractive Metallurgy Review, vol. 4, no. 2, pp. 226–253.

Tychsen, J.B.M.J., C.J. 2022. Artisanal and Small-Scale Mining Handbook for Southern African Region. Copenhagen: Geological Survey of Denmark and Greenland & Geological Survey of Portugal.

Tychsen, J., Batista, M. Carvalho, J. 2022. Artisanal and Small-Scale Mining Handbook for Southern Africa Region. Maputo: BDQ Grafica. Maputo. Mozambique.

UNEP. 2021. Sound Tailings Management in Artisanal and Small-Scale Gold Mining, Nairobi: United Nations Environment Programme.

Veiga, M.M. et al. 2006. Manual for Training Artisanal and. Global Mercury Project.

Veiga, M.M. et al. 2009. Mill leaching: a viable substitute for mercury amalgamation?. *Journal of Cleaner Production*, vol. 17, 15, pp. 1373–1381.

Veiga, M.M., Angeloci-Santos, G., Meech, J.A. 2014. Review of barriers to reduce mercury use in artisanal gold mining. *The Extractive Industries and Society,* vol. 1, no. 2, pp. 351–361.

Zhong, Q. et al. 2018. Intensification Behavior of Mercury Ions on Gold Cyanide Leaching. Metals, 8(1), p. 80.

Zia, Y., Mohammadnejad, S., Abdollahy, M. 2019. Gold passivation by sulfur species: A molecular picture. Minerals Engineering, Volume 134, pp. 215-221. ◆

Modelling the induction error in the Bøckman method for measuring furnace hearth voltages

by M. Sparta, V.K. Risinggård, U. Thisted

Affiliation:
NORCE Research, Universitetsveien 19, 4630 Kristiansand, Norway

Correspondence to:
V.K. Risinggård

Email:
veri@norceresearch.no

Dates:
Received: 27 Jun. 2025
Revised: .4 Apr. 2026
Accepted: 26 Jun. 2026
Published: Aug. 2026

How to cite:
Sparta M., Risinggård V.K., Thisted U. 2026. Modelling the induction error in the Bøckman method for measuring furnace hearth voltages. *Journal of the Southern African Institute of Mining and Metallurgy*, vol. 126, no. 8, pp. 475 – 482

DOI ID:
https://doi.org/10.17159/2411-9717/3761/2026

ORCiD:
M. Sparta
https://orcid.org/0000-0003-4218-5229
V.K. Risinggård
https://orcid.org/0000-0002-4841-6027
U. Thisted
https://orcid.org/0009-0008-3158-7402

Abstract

The Bøckman method is regularly used to obtain accurate measurements of the hearth voltage of smelting furnaces. The method uses three measuring leads in order to cancel induction errors using destructive interference when transferring the hearth voltage from the bottom of the furnace to the top of the electrodes. This paper presents an investigation of the Bøckman system's reliability, limitations, and background using finite-element-method simulations. A 3D model of an industrial-scale smelting furnace for Mn-alloy production is developed and used to examine the induction caused by balanced and unbalanced electrical conditions and material distributions.

Keywords

Submerged-arc furnace, electrode, induction, Bøckman method, finite-element method, mathematical modelling

Introduction

To ensure optimal operation of a large three-phase electric smelting furnace, accurate measurements of electrode loads are necessary (Magnussen, 2018). Typically, the electrode powers are calculated based on measurements of the electrode currents and the voltage drop between the top of the electrodes and the hearth of the furnace. For this purpose, the hearth of the furnace has to be electrically connected to transfer its potential to a measurement device in the control room. However, this poses significant problems as induced voltages due to the large magnetic field around the furnace lead to faulty readings (Stewart, 1980). Gerritsen et al. (2015) estimated that a furnace operating at 120 kA could see a 16 V error due to the induction when using a single measurement lead.

To circumvent this problem, Bøckman (1973a) proposed a method that uses three measuring leads. All leads are connected to the same point beneath the furnace, and each lead is drawn up to the top of the furnace directly outside one of the three electrodes. These three leads are connected in an area of low magnetic flux located above the furnace. The induced voltages in the leads interfere destructively; thus the voltage at the connection of the three leads replicates the voltage in the hearth. In the industry, it is widely believed that this method of measuring voltage between an electrode and the furnace hearth is, in principle, accurate. However, practical considerations often prevent a symmetric placement of the leads as described in the original patents (Bøckman, 1973a, 1973b). Moreover, it is unclear how well a method that depends on destructive interference of the induced voltages works for furnaces with asymmetrical electrical conditions.

There is no public survey available that analyses the background of the Bøckman approach and that discusses its reliability and limitations. To address this gap in the literature, this paper analyses different lead arrangements and their susceptibility to induction errors through computational investigations. Moreover, the effect of the electrical state of the furnace on the accuracy of the readings is examined. A finite-element-method (FEM) model (Zienkiewicz, Morgan, 2006) of an industrial-scale furnace for the production of ferromanganese was implemented to this end. The model builds on previous work on three-dimensional (3D) case studies of large submerged arc furnaces (Herland et al., 2018, 2019; Fromreide et al., 2021, 2023; Sparta, Varagnolo, Stråbø, et al., 2021; Sparta, Varagnolo, Martens, et al., 2021).

The use of 3D models for submerged-arc furnaces (SAF) has been discussed by several authors. For example, Dhainaut (2004) employed a DC model to examine the distribution of current and power when the current enters one electrode and evenly distributes to the other two electrodes. Halvorsen et al. (2016) demonstrated that, as long as electromagnetic induction can be disregarded, combining the results from two DC computations can determine the conditions at any point in the AC cycle or the time-averaged distribution of power and current. Bezuidenhout et al. (2009) developed a 3D computational fluid dynamics model to investigate the internal dynamics of an electrical furnace used for smelting platinum group metal concentrates. Scheepers et al. (2010) modelled and optimised a SAF for the production of phosphorus. Toh et al. (2005) utilised Maxwell's equations along with a finite-volume-method approach to model the steel-making process. Darmana et al. (2012) developed a multiphysics model incorporating thermodynamics, electricity, hydrodynamics, heat radiation, and chemical reactions for a SAF. Karalis et al. (2016) and Karalis et al. (2021) investigated the impact of slag properties, electrode shape and immersion depth on furnace heating in ferronickel processing. Yu et al. (2021) and Yu et al. (2023) developed a transient multiphysics model to predict the complex smelting state in a ferrochrome SAF. Finally, researchers at Reykjavík University simulated the effects of electrode shape, pitch circle diameter, and frequency on the current distribution in submerged arc furnaces for silicon production (Tesfahunegn, Magnússon, et al., 2018a, 2018b, 2020b, 2020a, 2021; Tesfahunegn, Sævarsdóttir, et al., 2018).

The paper is organised as follows: Section 2 presents a FEM model of a submerged arc furnace and outlines the approach to computing the inductive terms in the leads. Section 3 discusses the general properties of the induced terms. Section 4 investigates the phenomenon of destructive interference of the induced terms on symmetrically arranged leads under ideal furnace conditions, as well as the impact of breaking the lead symmetry. Finally, Sections 5 and 6 extends the analysis to the case of an unbalanced furnace.

Finite-element model

As shown in Figure 1 (left panel), the furnace model is 12.3 m in diameter and approximately 9 m high to the top of the roof and includes three electrodes, each with a diameter of 1.8 m spaced at 4.2 m apart (center-to-center distance). The furnace is composed of a steel roof and shell with a thickness of 25 mm, as well as non-conductive insulation layers (200 mm), conductive carbon materials (ranging from 660 mm to 850 mm thickness and extending up to 5 m above the alloy layer), charge banks between the electrodes with varying electrical properties (resistivity ranging from 10 mΩ·m to 300 mΩ·m), and coke beds. The coke beds have a range of diameters, from 4.86 m at the bottom to 2.16 m at the top, and a height of 1.53 m measured from the alloy layer. The shape of the coke beds can be controlled using a shape parameter, and their resistivity ranges between 4.12 mΩ·m and 7.20 mΩ·m. The model is coupled with an electrical circuit model that serves as the power supply, tracking the true power for each phase. However, structural elements surrounding the furnace are not incorporated in this model.

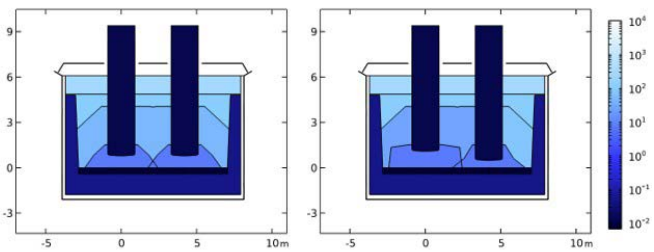

Figure 1—Cross section through the centres of electrode 3 and 1. The ideal case (left) and the unbalanced (right). Resistivity (mΩ·m) of the material is color coded, the darker the more conductive

The model is implemented in COMSOL Multiphysics (COMSOL Inc., 2024b) and Maxwell's equations are solved in the frequency domain using the magnetic and electric fields (mef) interface (COMSOL Inc., 2024a).

To study the Bøckman leads under different conditions, three reference cases have been considered, and the different parameters are listed in Table 1. In the "ideal" case, the electrode tips are equidistant from the alloy pool, and the shape factors and material properties of the coke beds are equal across all three electrodes. The left panel of Figure 1 illustrates the ideal case by showing the cross section passing through electrodes 3 and 1. For the "unbalanced" case, the electrodes have different heights within the coke beds, and these beds possess distinct characteristics such as shape, material properties, and surrounding conditions (right panel in Figure 1). In the "balanced" case, the properties of the coke beds and charges remain the same as in the unbalanced case, while electrode tip positions and the transformer voltages have been adjusted to achieve balanced electrical conditions and the correct power level.

The Bøckman method

The time-varying magnetic fields existing in the vicinity of the furnace due to the electrode currents give rise to induced voltages in the Bøckman leads. The voltage V_f^L at the end of the L-th lead can be calculated as the sum of the voltage at the starting point (V_i) and the induced term:

$$V_f^L = V_i + \int_L \frac{\partial \vec{A}}{\partial t} \cdot d\vec{l}, \qquad [1]$$

where $\partial \vec{A}/\partial t$ is the induced electric field, the integral is calculated as a path integral over L, and $(\partial \vec{A}/\partial t)\cdot\vec{l}$ is the component of the induced electric field tangential to the path L. The Bøckman

Table 1

Parameters defining the three cases

Case	Ideal	Unbalanced	Balanced
Root-mean-square transformer voltage (V)	250.00	250.00	246.00
Electrode 1 tip position (m)	0.80	0.50	0.74
Electrode 2 tip position (m)	0.80	0.80	1.04
Electrode 3 tip position (m)	0.80	1.10	1.13
Resistivity coke bed 1 (mΩ·m)	7.20	7.10	7.10
Resistivity coke bed 2 (mΩ·m)	7.20	6.50	6.50
Resistivity coke bed 3 (mΩ·m)	7.20	4.12	4.12
Coke bed 1 shape (1)	0.50	0.30	0.30
Coke bed 2 and 3 shape (1)	0.50	0.98	0.98
Resistivity charge el. 1 and 2 (mΩ·m)	47.00	72.08	72.08
Resistivity charge el. 2 and 3 (mΩ·m)	47.00	26.54	26.54
Resistivity charge el. 3 and 1 (mΩ·m)	47.00	26.54	26.54

method uses three measuring leads (L, M, and N). The voltage at the point at which these leads are connected is the average of the three lead voltages (V_f^L, V_f^M, and V_f^N):

$$V_f^{(LMN)} = \frac{1}{3}\left(V_f^L + V_f^M + V_f^N\right) = V_i + \frac{1}{3}\left(\int_L \frac{\partial \vec{A}}{\partial t}\cdot d\vec{l} + \int_M \frac{\partial \vec{A}}{\partial t}\cdot d\vec{l} + \int_N \frac{\partial \vec{A}}{\partial t}\cdot d\vec{l}\right).$$

In the ideal case, the induced voltages cancel and $V_f^{(LMN)}=V_i$.

The voltage induced in the Bøckman leads has the same frequency as the original time-varying magnetic field. Therefore, the voltage in the L-th lead can also be written as

$$V_f^L - V_i = A(L,P)\sin[\omega t + \phi(L,P)], \quad [2]$$

where the amplitude $A(L,P)$ and phase $\phi(L,P)$ of the signal depend on the path of the lead (L) and the paths of the electric currents that generate the magnetic field in the first place (P). Regardless of the amplitude and phase, the sum of two or more sinusoidal waves with the same frequency ω is again a sinusoidal wave with frequency ω:

$$V_f^L - V_i = A_L\sin(\omega t + \phi_L),\quad V_f^M - V_i = A_M\sin(\omega t + \phi_M),\quad V_f^N - V_i = A_N\sin(\omega t + \phi_N)$$
$$3\left(V_f^{(LMN)} - V_i\right) = \sum_{i\in\{L,M,N\}} A_i\sin(\omega t + \phi_i) = A_{(LMN)}\sin\left(\omega t + \phi_{(LMN)}\right) \quad [3]$$

where we have written A_i=$A(i,P)$ and ϕ_i=$\phi(i,P)$ for simplicity, and $A_{(LMN)}$ and $\phi_{(LMN)}$ satisfy

$$A_{(LMN)}^2 = \sum_{i,j} A_i A_j\cos(\phi_i - \phi_j),\quad \tan\phi_{(LMN)} = \frac{\sum_i A_i \sin\phi_i}{\sum_i A_i \cos\phi_i}, \quad [4]$$

for $i \in \{L,M,N\}$ and $j \in \{L,M,N\}$. In real-world implementations of the Bøckman measurement, the positioning of leads in an industrial environment often involves negotiating obstacles and other equipment, resulting in a tortuous path. On the other hand, when conducting modelling investigations, ideal implementations tend to use straight segments for simplicity. Despite these differences, Equation 2 shows that both scenarios result in an induced voltage with a sinusoidal waveform and Equations. 3 and 4 show that values of the amplitudes A_i and phases ϕ_i exist for which $V_f(LMN) = V_i$.

The left panel of Figure 2 demonstrates two lead implementations: one that is curvilinear and another that is idealised and consists of four straight segments. Both paths originate beneath the alloy bath in the conductive carbon lining (this point will be referred to as the "hearth" in the remainder of the article) and terminate at the furnace's central axis 16 m above the alloy level. For reference, the straight path descends to a depth of 2 m below the furnace base and it remains 5 m away from the vertical wall of the steel shell. The segmented and curvilinear path lengths are 46.3 m and 57.5 m, respectively. These paths are colour-coded based on the tangential component of the electric field (V/m), which integrates to yield the total induced voltage (Equation 1). The right panel of the figure illustrates the sinusoidal waveforms of the induced voltages over one cycle of the current. Interestingly, even for an overly tortuous path, the induced voltage can be well approximated by analysing the induced voltage in an ideal lead placed in the same general area. For this reason, the remainder of this work will focus on simplified straight paths.

Figure 3 shows the inner workings of the Bøckman system as intended in the original patent. The left panel shows the relationship between the time-resolved voltages during one current cycle, whereas the right panel shows the corresponding phasors. With the leads being symmetrically placed around the furnace, the phasors of the induced voltages point to the vertexes of an equilateral triangle centred at the origin. Consequently, the phasor sum cancels and the voltage at the common connection of the Bøckman leads is equal to the voltage in the hearth. (The deviation from zero in Figure 3 is a numerical artifact arising from asymmetries in the computational mesh.)

Ideal case

This section focuses on the ideal case, as outlined in Table 1. In the ideal case, the material distribution within the furnace has a three-fold rotational symmetry. Additionally, the electric circuit energising the system applies equal voltages to all electrodes. Under these conditions, the furnace exhibits a total active power of 38.9 MW and reactive power of 42.3 MVA. The electrode resistance is measured at 0.74 mΩ with a root-mean-square (RMS) current of 132.5 kA.

Symmetric lead placement

To investigate an idealised Bøckman system, the furnace model has been surrounded by 36 instances of the previously discussed idealised lead, spaced at intervals of 10°. Figure 4 shows a representation of these leads, colour-coded based on the tangential component of the electric field, at a specific moment within the current cycle. The FEM calculation shows that the contributions from each of the segments, constituting one lead, are in phase. Furthermore, owing to its length, the vertical segment is responsible for approximately 50% of the total induced voltage while the top section, where the lead returns toward the center, accounts for around 40%. The bottom horizontal section only contributes about 10% to the total signal, and the vertical section from the hearth downward has no contribution because it coincides with the symmetry axis of the furnace. Due to the idealised nature of these leads (only vertical and radial segments) the tangential component

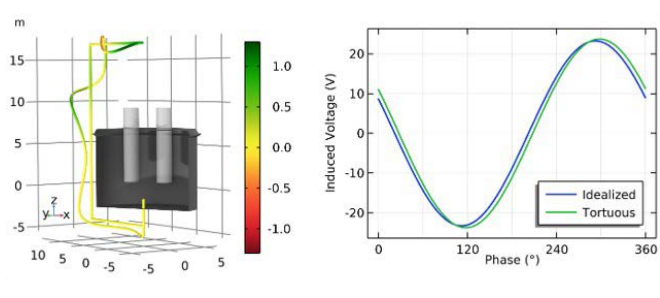

Figure 2—Left: A tortuous vs. an idealised lead color coded with the instantaneous amplitude of the tangential electric field (V/m). Right: corresponding sinusoidal signal of the induced voltage during a current cycle

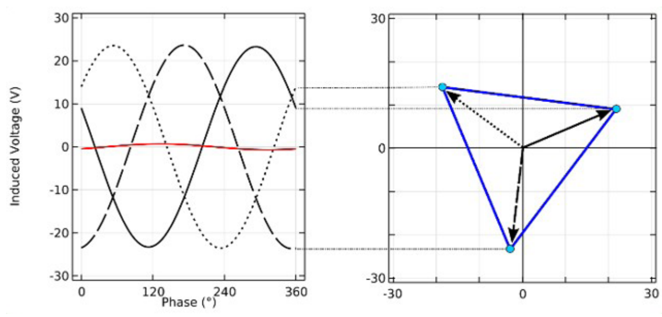

Figure 3—Time resolved and phasor diagram of the induced voltages in a three-leads symmetric Bøckman system in the eclipsed configuration. The combined signal of the three leads in red

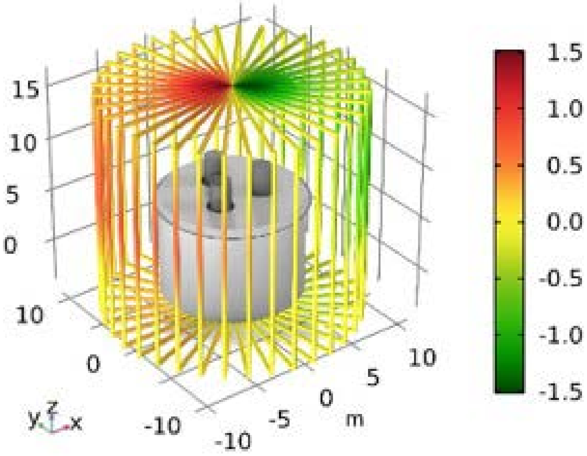

Figure 4—Symmetric furnace: 36 leads colour coded with the instantaneous amplitude of the tangential electric field (V/m)

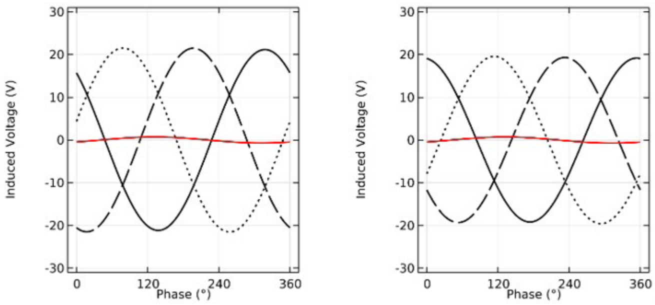

Figure 5—Two distinct implementations of the Bøckman method, based on leads in the staggered configuration (right) and a configuration that is intermediate between the fully eclipsed and staggered configurations (left). Both implementations give the same cancellation of the induced voltages (red lines)

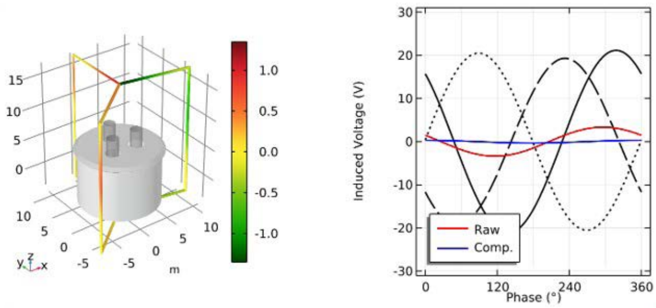

Figure 6—Asymmetry in the placement of the leads. Effect on the partial destructive interference (red) and compensated sum (blue)

of the electric field appears as a dipole structure rotating at the frequency of the current. The dipole symmetry can be understood by considering the analogy between the three-phase current in the three furnace electrodes and the current in a three-phase slot-wound dipole electric motor (Pyrhonen et al., 2014).

Supplementary Figure S-1 displays the time-resolved induced voltage for the 36 leads depicted in Figure 4. Due to the harmonic nature of the electromagnetic field surrounding the furnace, a geometric rotation of the leads around the furnace's center corresponds to a phase shift of a comparable angle. The amplitude of the induced signal depends on the positioning of the lead relative to the electrodes. For example, leads in an eclipsed configuration (positioned directly behind the electrodes) experience a larger induction compared to leads in a staggered configuration (positioned between the electrodes). The induced voltages are approximately 23.5 V and 19.0 V in the two cases.

Since a Bøckman system needs three measuring leads spaced 120° apart, the 36 leads depicted in Figure 4 enable the simulation of 12 unique Bøckman implementations. The induced voltages over one current cycle are shown in Figure 3 for leads in the eclipsed configuration and in Figure 5 for leads in the staggered and an in-between configuration. Symmetry considerations dictate that, in the ideal case, the induced voltages in the three Bøckman leads interfere destructively. The numerical experiments discussed in Figures 3 and 5 demonstrate that the FEM implementation is able to capture these effects with satisfying accuracy.

Asymmetric lead placement and compensation

Achieving perfect symmetry in lead placement is often challenging in an industrial setting. To address this, a strategy for compensating for asymmetric placement was developed as part of the original patent; an adjustable impedance can be used on each of the leads to ensure full cancellation (Bøckman, 1973a, 1973b).

Figure 6 investigates the impact of asymmetric placement of the leads on the implementation result. In this example, the leads are spaced at intervals of 130°, 140°, and 90°, instead of the standard 120°. Consequently, the destructive interference is only partial, and there is a residual induction error present after averaging the lead contributions (red line). In principle, there are an infinite number of possible ways to compensate the three signals so that their sum cancels (Equations 3 and 4).

Figure 7A provides an alternative representation, through a phasor diagram, of the partial destructive interference caused by the asymmetric leads mentioned above. The phasor summation reveals the presence of a residual induction error (depicted as solid red). In the real-world setup, the measurement error will be one third

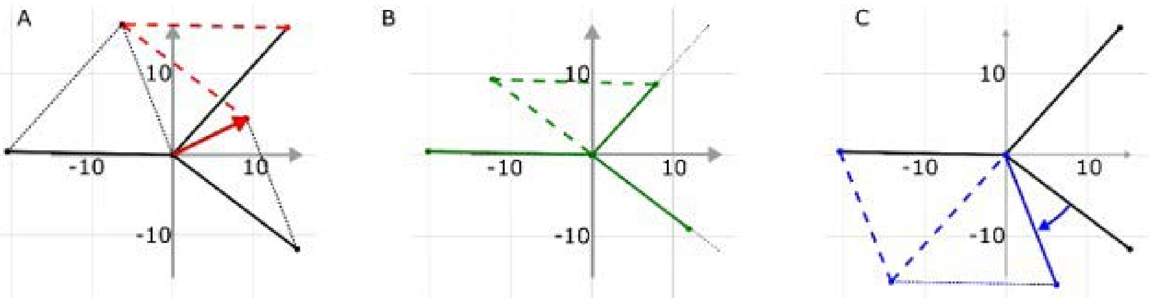

Figure 7—A: Phasor diagram of the induced voltage of a Bøckman system with asymmetric placement of the leads. B: Compensation by two resistances. C: Compensation by one impedance

of the sum due to averaging. Formally, two degrees of freedom are sufficient to bring the induction error to zero, i.e., two resistors or one resistor and one inductor/capacitor. Figure 7B demonstrates the simulation of an appropriate choice of two resistors to achieve compensation by scaling two of the three original phasors by 58% and 80%, respectively. The summation of these compensated phasors leads back to the origin of the coordinate system, indicating complete cancellation. Alternatively, Figure 7C presents another approach where the equivalent effect of a single impedance is applied to one of the leads. In this specific instance, the signal of the second lead is scaled to 89% and rotated by 31.5° (blue arrow).

The real-world compensation procedure has a significant impact on the quality of the hearth-voltage measurement. Errors in the calibration of the Bøckman resistors will affect the resulting measurements of the electrode voltages. Further investigation is needed to identify the optimal approach to compensation.

Unbalanced case

This section extends the analysis of Section 4 to cover the scenario of an unbalanced furnace by focusing on the unbalanced case outlined in Table 1 and Figure 1. In this case, the electrodes are positioned at distances of 50 cm, 80 cm, and 110 cm from the alloy bath. The resulting total active power is 38.8 MW, and the total reactive power is 46.5 MVA. The resistances of the electrodes are calculated to be 0.64 mΩ, 0.64 mΩ, and 0.70 mΩ, with RMS currents of 138.0 kA, 144.5 kA, and 137.2 kA, respectively.

Symmetric lead placement

With this furnace configuration, the three induced voltages have different amplitudes, and their phases are not spaced 120° apart. Consequently, there is only a partial destructive interference and a residual induction error is present in addition to the actual hearth voltage, as shown in Figure 8 for two different implementations. The left panels show leads in an eclipsed configuration, whereas the right panel show staggered leads. The similarities between the two implementations suggests that the residual inductive signal is independent of the lead path. In fact, the inductive error is identical across all 12 Bøckman implementations to an accuracy of 0.01 V of amplitude and 0.1° of phase. To conclude, despite the symmetric lead placement as described in the original patent, a residual inductive voltage persists in the unbalanced case. The residual induction error is more or less in phase with the true hearth voltage.

Asymmetric lead placement and compensation

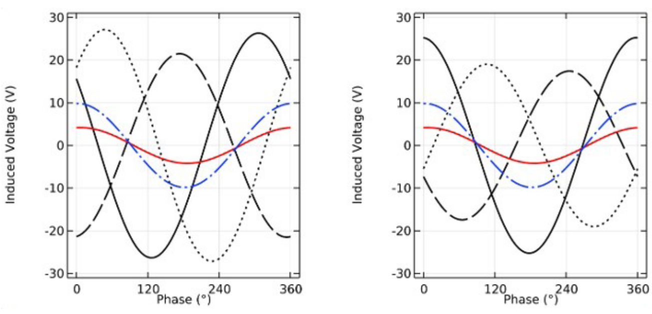

Figure 8—Unbalanced case with symmetric lead placement. Two distinct implementations of the Bøckman method, based on eclipsed (left) or staggered (right) leads. The combination of the three leads (black lines) gives partial cancellation of induced voltages (red lines). Voltage in the hearth of the furnace for reference (blue)

As demonstrated in Section 4, scaling and rotating a single phasor can effectively compensate for the effects of asymmetric lead placement in the ideal case. However, it remains to be determined if this compensation strategy retains its validity in non-ideal furnace environments. Figure 9 illustrates a Bøckman system with asymmetric lead placement in the unbalanced case. Asymmetric lead placement leads to a larger residual inductive error, and one that is phase shifted with respect to the case with symmetric leads. However, applying the same compensation as for the ideal case almost brings the inductive error back to the value seen for symmetric leads. To conclude, compensation for asymmetric lead placement works for unbalanced as well as ideal furnaces.

Balanced case

In the unbalanced case, there are significant differences among the three electrode resistances. This section considers the balanced case in Table 1, in which the electrodes' penetration into the burden has been changed to return all three electrode resistances to the interval 0.734 mΩ –0.737 mΩ, with RMS currents of 132.3 kA – 132.7 kA. Furthermore, the transformer voltage has been adjusted to achieve the same active power as in the previous cases (38.9 MW).

Despite achieving electrical balance, different voltages are still induced in the Bøckman leads due to the asymmetric distribution of materials in the furnace, which again leads to an asymmetric distribution of current within the furnace volume. Consequently, a residual inductive error persists. As shown in Figure 10, this error remains in phase with the voltage in the hearth. A comparison between Figure 8 and Figure 10 demonstrates that an electrical rebalancing of the furnace reduces both the residual inductive error in the Bøckman leads (from 4.2 V to 2.9 V), as well as the voltage in the furnace hearth (from 9.8 V to 4.6 V).

Conclusion

A 3D FEM model for the electrical conditions of a FeMn furnace has been implemented to study the induction in the leads used in the Bøckman system. In the scenario where the electrical state of the furnace is balanced, and the material distributions are

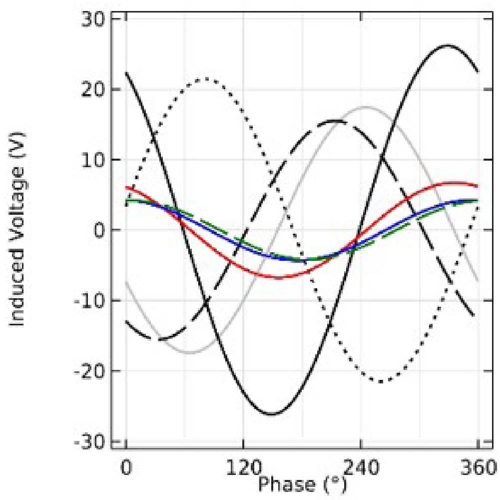

Figure 9—Unbalanced case with asymmetric lead placement. The uncompensated voltages in the leads are shown as gray (solid) and black (solid and dotted) lines. The compensated voltage in one of the leads is shown as a black dashed line. The uncompensated induction error is shown in red. The compensated induction error is shown in blue, to be compared with a symmetric lead placement (green)

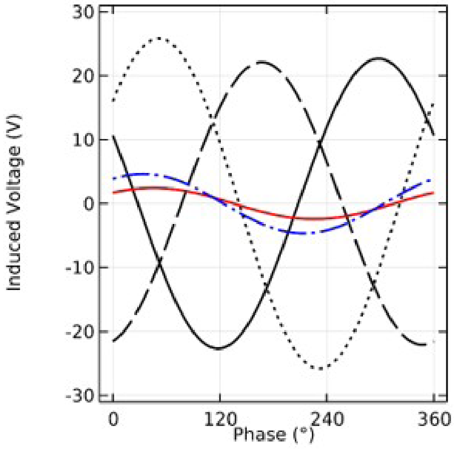

Figure 10—Balanced case with symmetric lead placement. The combination of the three Bøckman leads (black lines) gives partial cancellation of induced voltages (red line). Voltage in the hearth of the furnace for reference (blue)

symmetric, placing the leads symmetrically around the furnace permits complete destructive interference of the induced voltage. Conversely, in a situation with material imbalances in the furnace, only partial cancellation of signals occurs, leading to a residual induction error. Notably, the residual voltage is in phase with the voltage in the hearth, thus not interfering with the electrode controllers. Rebalancing the electrodes of a furnace with an asymmetric material distribution reduces the residual induced voltage, but cannot eliminate it entirely.

An asymmetric placement of the Bøckman leads must be compensated for to achieve a cancellation of the induced voltages. Compensation can be achieved using at least two resistors or one resistor and one inductor/capacitor, and the compensation remains valid irrespective of the furnace state.

Acknowledgements

This paper is published as part of the project "Electrical Conditions in Submerged Arc Furnaces—Identification and Improvement" (SAFECI), with financial support from the Research Council of Norway (project number 326802) and the companies Elkem, Eramet Norway, Finnfjord and Wacker Chemicals Norway.

Author statement

MS: Conceptualisation, methodology, software, investigation, formal analysis, writing – original draft preparation, visualisation, project administration, funding acquisition.

VKR: Conceptualisation, methodology, formal analysis, writing – original draft preparation, writing – review and editing preparation.

UT: Methodology, formal analysis, writing – original draft preparation.

Conflict of interest

The authors declare that they have no conflict of interest.

Bibliography

Bezuidenhout, J.J., Eksteen, J.J., Bradshaw, S.M. 2009. Computational fluid dynamic modelling of an electric furnace used in the smelting of PGM containing concentrates. Minerals Engineering, vol. 22, no. 11, pp. 995–1006. Available at: https://doi.org/10.1016/j.mineng.2009.03.009

Bøckman, O.C. 1973a. Anordning for måling av kraterspenningene i en trefase smelteovn med elektrodene i trekant. Available at: https://patents.google.com/patent/NO126288B/en

Bøckman, O.C. 1973b. Arrangement for measuring the crater voltages in a three-phase electric furnace with electrodes arranged in a delta. Available at: https://patents.google.com/patent/US3757021/en

COMSOL Inc. 2024a. AC/DC module user's guide. v6.2. Available at: https://doc.comsol.com/6.2/doc/com.comsol.help.acdc/ACDCModuleUsersGuide.pdf

COMSOL Inc. 2024b. COMSOL multiphysics reference manual. v6.2. Available at: https://doc.comsol.com/6.2/doc/com.comsol.help.comsol/COMSOL_ReferenceManual.pdf

Darmana, D., Olsen, J.E., Tang, K., Ringdalen, E. 2012. Modeling concept for submerged-arc furnaces. *Proceedings of the 9th International Conference on CFD in the Minerals and Process Industries. CSIRO, Melbourne, Australia*. Available at: https://www.cfd.com.au/cfd_conf12/PDFs/062DAR.pdf

Dhainaut, M. 2004. Simulation of the electric field in a submerged arc furnace. *Proceedings of the 10th International Ferro-Alloys Congress (INFACON X). South African Institute of Mining and Metallurgy, Cape Town, South Africa*, pp. 605–613. Available at: https://www.pyrometallurgy.co.za/InfaconX/079.pdf

Fromreide, M., Gómez, D., Halvorsen, S.A., Salgado, P. 2023. Induced currents in the lining and steel shell of submerged arc furnaces. *Journal of Sustainable Metallurgy*, vol. 9, no. 1, pp. 375–385. Available at: https://doi.org/10.1007/s40831-022-00625-6

Fromreide, M., Halvorsen, S.A., Sparta, M., Risinggård, V.K., Salgado, P., Gómez, D., Herland, E.V. 2021. Effects of alternating currents in the hearth of submerged arc furnaces. *Proceedings of the 16th International Ferro-Alloys Congress (INFACON XVI). Social Science Research Network, Trondheim, Norway.* Available at: https://doi.org/10.2139/ssrn.3926716

Gerritsen, T., Tracy, P., Saber, F. 2015. Electrode voltage measurement in electric furnaces: Analysis of error in measurement and calculation. *Proceedings of the 14th International Ferro-Alloys Congress (INFACON XIV). International Committee on Ferro-Alloys, Kyiv, Ukraine*, pp. 338–348. Available at: https://www.pyrometallurgy.co.za/InfaconXIV/338-Gerritsen.pdf

Halvorsen, S.A., Olsen, H.A.H., Fromreide, M. 2016. An efficient simulation method for current and power distribution in 3-phase electrical smelting furnaces. *IFAC-PapersOnLine*, vol. 49, no. 20, pp. 167–172. Available at: https://doi.org/10.1016/j.ifacol.2016.10.115

Herland, E.V., Sparta, M., Halvorsen, S.A. 2018. 3D models of proximity effects in large FeSi and FeMn furnaces. Journal of the Southern African Institute of Mining and Metallurgy, vol. 118, no. 6, pp. 607–618. Available at: https://doi.org/10.17159/2411-9717/2018/v118n6a8

Herland, E.V., Sparta, M., Halvorsen, S.A. 2019. Skin and proximity effects in electrodes and furnace shells. Metallurgical and Materials Transactions B, vol. 50, no. 6, pp. 2884–2897. Available at: https://doi.org/10.1007/s11663-019-01651-8

Karalis, K., Karalis, N., Karkalos, N., Ntallis, N., Antipas, G.S.E., Xenidis, A. 2021. Three-dimensional computational fluid dynamics analysis of an electric submerged arc furnace. *Scientific Reports*, vol. 11, no. 1, pp. 17637. Available at: https://doi.org/10.1038/s41598-021-96085-1

Karalis, K.T., Karkalos, N., Cheimarios, N., Antipas, G.S.E., Xenidis, A., Boudouvis, A.G. 2016. A CFD analysis of slag properties, electrode shape and immersion depth effects on electric submerged arc furnace heating in ferronickel processing. *Applied Mathematical Modelling*, vol. 40, no. 21–22, pp. 9052–9066. Available at: https://doi.org/10.1016/j.apm.2016.05.045

Magnussen, T.E. 2018. Basic parameters in the operation and design of submerged arc furnaces, with particular reference to production of high-silicon alloys. J*ournal of the Southern African Institute of Mining and Metallurgy*, vol. 118, no. 6. Available at: https://doi.org/10.17159/2411-9717/2018/v118n6a11

Pyrhonen, J., Jokinen, T., Hrabovcová, V. 2014. Design of rotating electrical machines. 2nd ed. Wiley.

Scheepers, E., Yang, Y., Adema, A.T., Boom, R., Reuter, M.A. 2010. Process modeling and optimization of a submerged arc furnace for phosphorus production. *Metallurgical and Materials Transactions B*, vol. 41, no. 5, pp. 990–1005. Available at: https://doi.org/10.1007/s11663-010-9403-3

Sparta, M., Varagnolo, D., Martens, H., Halvorsen, S.A. 2021. Metamodeling of the electrical conditions in submerged arc furnaces. Proceedings of the 16th International Ferro-Alloys Congress (INFACON XVI). Social Science Research Network, *Trondheim*. Available at: https://doi.org/10.2139/ssrn.3926715

Sparta, M., Varagnolo, D., Stråbø, K., Halvorsen, S.A., Herland, E.V., Martens, H. 2021. Metamodeling of the electrical conditions in submerged-arc furnaces. Metallurgical and Materials Transactions B, vol. 52, pp. 1267–1278. Available at: https://doi.org/10.1007/s11663-021-02089-7

Stewart, A.B. 1980. An analysis of the electrical circuit of submerged-arc furnaces. PhD thesis. University of Cape Town. Available at: http://hdl.handle.net/11427/14048

Tesfahunegn, Y.A., Magnússon, Þ., Tangstad, M., Sævarsdóttir, G.A. 2018a. Effect of electrode shape on the current distribution in submerged arc furnaces for silicon production – a modelling approach. *Journal of the Southern African Institute of Mining and Metallurgy*, vol. 118, no. 6, pp. 595–600. Available at: https://doi.org/10.17159/2411-9717/2018/v118n6a6

Tesfahunegn, Y.A., Magnússon, Þ., Tangstad, M., Sævarsdóttir, G.A. 2018b. The effect of pitch circle diameter of electrodes on current distributions in submerged arc furnace. 2018 *IEEE MTT-S International Conference on Numerical Electromagnetic and Multiphysics Modeling and Optimization (NEMO). IEEE, Reykjavík, Iceland.* Available at: https://doi.org/10.1109/NEMO.2018.8503177

Tesfahunegn, Y.A., Magnússon, Þ., Tangstad, M., Sævarsdóttir, G.A. 2020a. Comparative study of AC and DC solvers based on current and power distributions in a submerged arc furnace. *Metallurgical and Materials Transactions* B, vol. 51, no. 2, pp. 510–518. Available at: https://doi.org/10.1007/s11663-020-01794-z

Tesfahunegn, Y.A., Magnússon, Þ., Tangstad, M., Sævarsdóttir, G.A. 2020b. The effect of side arcs on current distributions in a submerged arc furnace for silicon production. J. Lee, S. Wagstaff, G. Lambotte, A. Allanore, and F. Tesfaye (eds.). Materials Processing Fundamentals 2020. *The Minerals, Metals & Materials Series, Springer International Publishing*, pp. 177–188. Available at: https://doi.org/10.1007/978-3-030-36556-1_16

Tesfahunegn, Y.A., Magnússon, Þ., Tangstad, M., Sævarsdóttir, G.A. 2021. The effect of electrode movements on electrical characteristics of a submerged arc furnace. JOM, vol. 73, no. 10, pp. 2963–2972. Available at: https://doi.org/10.1007/s11837-021-04818-4

Tesfahunegn, Y.A., Sævarsdóttir, G.A., Magnússon, Þ., Tangstad, M. 2018. The effect of frequency on current distributions inside submerged arc furnace. *2018 IEEE MTT-S International Conference on Numerical Electromagnetic and Multiphysics Modeling and Optimization (NEMO)*. IEEE, Reykjavík, Iceland. Available at: https://doi.org/10.1109/NEMO.2018.8503083

Toh, T., Yamasaki, N., Seki, T., Tanaka, J. 2005. Magnetohydrodynamic simulation in steelmaking process by 3D finite volume method. *Proceeding of the 4th International Conference on CFD in the Minerals and Process Industries. SINTEF Academic Press, Trondheim*, Norway. Available at: https://www.sintef.no/globalassets/project/cfd2008/cfd2005_papers/21_toh_yamasaki_seki_tanaka.pdf

Yu, Y., Li, B., Liu, Z., Qi, F., Liu, C., Rong, W., Kuang, S. 2023. Simulation of ferrochrome settling behavior in a submerged arc furnace using a multiphysics and multiphase model. *Metallurgical and Materials Transactions B*, vol. 54, no. 4, pp. 2080–2094. Available at: https://doi.org/10.1007/s11663-023-02817-1

Yu, Y., Li, B., Yun, C., Qi, F., Liu, Z. 2021. Modeling on reduction reaction of metal oxides for submerged arc furnace in ferrochrome pellets smelting process. *Metallurgical and Materials Transactions B*, vol. 52, no. 6, pp. 3907–3919. Available at: https://doi.org/10.1007/s11663-021-02304-5

Zienkiewicz, O.C., Morgan, K. 2006. Finite elements and approximation. Dover Publications. ◆

Lessons from the pillar wrapping monitoring programme at New Afton

by Y. Yanagimura[1], J. Hadjigeorgiou[2]

Affiliation:
[1] Coeur Mining Inc., Kamloops, Canada
[2] University of Toronto, Toronto, Canada

Correspondence to:
J. Hadjigeorgiou

Email:
john.hadjigeorgiou@utoronto.ca

Dates:
Received: 18 Feb. 2026
Revised: 17 Jun. 2026
Accepted: 02 Jul. 2026
Published: Aug. 2026

How to cite:
Yanagimura Y. Hadjigeorgiou J. 2026. Lessons from the pillar wrapping monitoring program at New Afton. *Journal of the Southern African Institute of Mining and Metallurgy*, vol. 126, no. 8, pp. 483 – 490

DOI ID:
https://doi.org/10.17159/2411-9717/3910/2026

ORCiD:
Y. Yanagimura
https://orcid.org/0009-0009-8935-211X
J. Hadjigeorgiou
https://orcid.org/0000-0002-6047-3964

Abstract

Pillar wrapping refers to a ground support system that uses rope or cable slings. It is commonly used to support the drawpoint pillars in the extraction level of block cave mines. An instrumentation study was conducted at New Afton mine to quantitatively assess the field performance of pillar wrapping used in the B3 extraction level. Instrumented cable slings were installed at two drawpoints to capture the behaviour of the support system through cave initiation and early stages of propagation. Key factors that influence the performance of cable slings during early stages of the caving process were determined through the analysis and interpretation of the field data. A series of practical recommendations have been provided for designing and implementing cable slings.

Keywords

Cave mining, extraction level, pillar wrapping, instrumented cable slings

Introduction

In block caving operations, a major challenge is ensuring that the extraction level remains serviceable throughout the life of the cave block. Consequently, ground support systems need to be selected and designed to ensure their long-term performance for the working life of the extraction level. This requires careful consideration of the evolving stress conditions induced from cave initiation through to maturity—conditions that are often complex and difficult to predict. To address these challenges, yielding ground support systems that incorporate deep anchorage and robust lateral restraint are advantageous, as they can accommodate substantial stress changes and large ground deformations.

Pillar wrapping, which uses rope or cable slings to strengthen pillars where production drives and drawpoints meet, is considered an effective ground support method for difficult extraction level conditions. This method enhances confinement and helps preserve the self-supporting capacity of the pillars. Empirical observations indicate that cable slings, due to their superior elongation capacity, outperform conventional reinforcement elements in controlling large deformations. However, their installation is relatively labour-intensive and costly compared to conventional support systems. There is consequently a need to justify the use of pillar wrapping by quantifying the added value to an operation. A template for an improved decision process has been provided by Stacey and Hadjigeorgiou (2022) through the quantified value created process (QVP). In this context the use of pillar wrapping may result in short-term value destruction (labour-intensive, higher costs) but the medium- and long-term value can be substantial, thus, justifying their use.

This paper presents the results of a comprehensive instrumentation programme conducted at the New Afton mine to monitor the performance of cable slings during the early stages of cave development. Building on an initial instrumentation trial, a broader monitoring initiative was implemented at the B3 extraction level at New Afton, enabling a quantitative assessment of the pillar wrapping system. The findings inform a set of practical recommendations aimed at optimising the use and effectiveness of cable slings in block cave environments.

History of pillar wrapping using cable slings

Cable slings for pillar support were introduced to the cave mining industry in the 1970s by D.H. Laubscher, who first tested the concept at the Shabanie asbestos mine in Zimbabwe. When introduced, 70-tonne Koepp ropes were successfully used to stabilise areas on the verge of collapse (Laubscher, 2000). It was recognised that controlling, rather than preventing, deformation in the rock mass was a more effective philosophy for ground support design.

Since then, pillar wrapping with cable slings has been trialed and implemented at several block cave mines to manage large deformation although their use is not well documented in the technical literature. In the 1990s, refinements to installation methods and performance were documented at the Cassiar mine in British Columbia (Jakubec, 1992). Yanagimura and Hadjigeorgiou (2022) summarised the results of a benchmarking study noting pillar wrapping applications at Finsch, Argyle, Palabora, Northparkes, New Afton, El Teniente, and Oyu Tolgoi mines. Key insights into the design and performance of pillar wrapping systems, drawn from these applications, are summarised in the following.

Application:

Cable slings are most used to support drawpoint corners, particularly the bullnose pillar. They can also be applied to the excavation back where large deformations are anticipated.

Support mechanism:

Across various sites, a consensus has emerged that cable sling pillar wrapping provides high support resistance and yielding capacity, allowing the rock mass to relax without collapsing. The confinement effect of the cable slings helps retain the self-supporting capability of the pillar by preserving the internal cohesion and friction of the rock mass surrounding the pillar core. However, to date, the performance of cable slings has primarily been supported by anecdotal evidence rather than quantitative measurements.

Installation methods:

The standard installation technique involves connecting and tensioning the cables using connector blocks and grips, with one tail end anchored in the rock mass, as per Figure 1. This method allows precise tensioning, typically in the range of 5 to 8 tonnes, using a cablebolt tensioner to remove slack while avoiding overstressing the cables. Maintaining appropriate tension is critical for providing lateral restraint during pillar relaxation. An alternative technique, Figure 2, uses friction rock stabilisers (split sets) to drive cable slings directly into the rock mass. While effective in rehabilitation scenarios, such as at the Cassiar mine, this method does not allow for direct tension measurement during installation, which limits control. Consequently, it is less widely employed.

Cable restraint:

Cable slings are secured to the excavation surface using either short reinforcement elements (e.g., resin rebar bolts) or long reinforcement (e.g., cablebolts), typically equipped with guide washer plates. These fixtures hold the cable slings tightly against the rock surface while allowing relative movement beneath the plates.

Timing of installation:

Pillar wrapping may be installed as part of the initial ground support during development of production drives and drawpoints or later for rehabilitation of damaged pillars. However, its effectiveness is generally reduced when applied post-failure, as the rock mass has already entered a post-peak state. In such cases, excessive loading can result in failure at the connector blocks or, in some instances, cable breakage.

Interaction with shotcrete:

Application of shotcrete over the cable slings can cause point loading or seizure of connector blocks as deformation occurs, potentially leading to premature failure of the support system. To mitigate these effects, some mine sites use protective pipe covers over exposed cable segments or apply grease to connector blocks prior to shotcrete application.

Site overview

The instrumented pillar wrapping case studies were at the New Afton mine, located approximately 10 km west of Kamloops, British Columbia. This is a block caving operation with three mining blocks at various stages (Figure 3). Current production is mainly from the B3 zone, with the B3 extraction level situated about 760 m below surface—160 m below and immediately west of Lift 1—operating at roughly 8,000 tonnes per day.

The B3 extraction level follows the El Teniente layout, featuring four main production drives spaced 27 m apart, intersected by drawpoint drifts every 16.5 m at a 56° angle. This level contains 65 drawbells, including 24 one-sided bells, with production drives and drawpoint crosscuts designed to be 4.5 m by 4.3 m.

Located 18 m above the extraction level, the B3 undercut level comprises five parallel drifts separated by 13.5 m-wide pillars. A

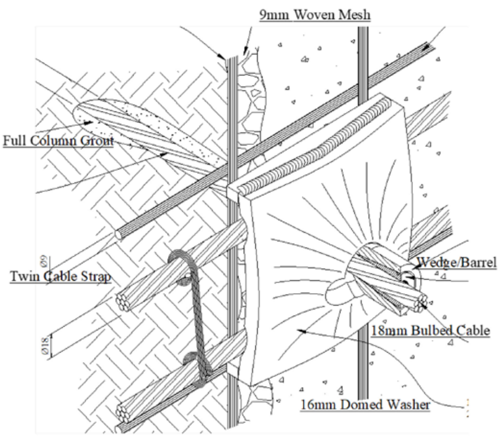

Figure 1—Pillar wrapping cable slings (after Wilson and Talu, 2004)

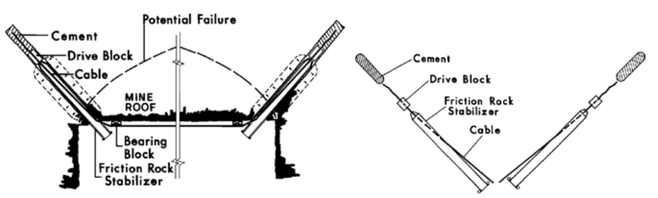

Figure 2—Schematic of Scott-system cable slings (after Castle and Scott, 1982)

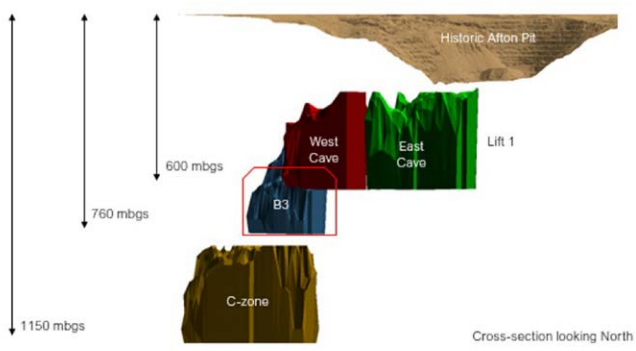

Figure 3—Overview of the New Afton block cave mine

half apex level, 12 m above the undercut, was developed to monitor undercut performance and reduce risks of remnant pillars that could jeopardise early drawpoint stability. Undercutting began in December 2020 and was completed by June 2022, progressing east to west via ring blasts spaced at 1.5 m intervals. After each blast, mucking removed swell, and confirmed connectivity to the apex level.

To mitigate damage from abutment stresses on the extraction level, an advanced undercutting technique was employed. At B3, only the production drives were constructed before undercutting began, so drawbells could be created at least 45° behind the undercut front within destressed rock. Mucking from blasted drawbells was minimised until all were blasted, ensuring even draw and maintaining cave health during initiation.

Geologically, the B3 extraction level is primarily composed of volcanic fragmental breccia (BXF), with monzonite and diorite intrusions to the southwest and picrite to the south (Figure 4). The Kamloops sedimentary domain is absent at this level. Face mapping during development indicated fair to poor rock mass quality, with RMR89 ratings between 47 and 56 (Bieniawski, 1989), largely due to fault structures intersecting the level. Regional structures parallel the production drives along the extraction level's boundaries, while local extensional features cut some drawbells obliquely.

Ground support in the B3 zone was a critical component of development and early production. Primary ground support included a first pass of 50 mm – 75 mm fibre-reinforced shotcrete, 6-gauge welded wire mesh pinned with 2.4 m D-bolts, 2.4 m MD bolts, or 2.1 m hybrid bolts (46 mm split sets with #7 rebar), effectively spaced at 1 m. Following the completion of primary support, drawpoint construction proceeded.

Secondary support comprised three rows of modified geometry cablebolts in the walls and back at 1.4 m – 1.5 m ring spacing, with self-drilling anchors (SDA) installed at the sill to control low-wall deformation. OSRO straps were applied along cablebolts, oriented parallel to the drift. OSRO straps are high-energy absorption elements made of a series of longitudinal, parallel, round, smooth bars attached together with strapping crossbars. The crossbars are loosely twisted around the longitudinal bars, as opposed to welded, allowing for a free rotational movement of the longitudinal bars. Where cable slings were used, three rows of double strand cable slings were installed over OSRO straps at drawpoint corners, bullnose, and camelback pillars (Figure 5). They were secured to the wall with cablebolts fitted with guide washer plates. Finally, a second pass of fibre-reinforced shotcrete was sprayed to protect support from equipment damage.

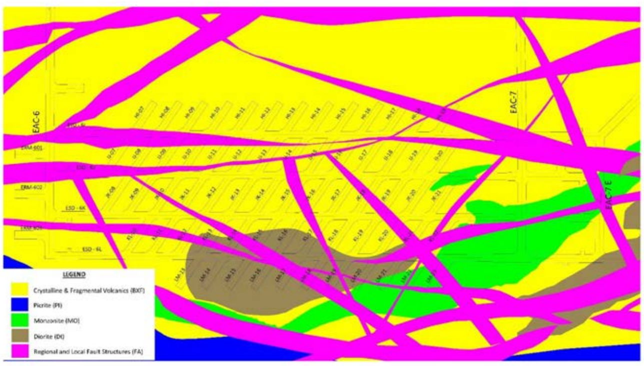

Figure 4—Lithology at the B3 extraction level

Instrumentation strategy

To monitor strain and load in the cable slings installed on New Afton's B3 extraction level, it was proposed to replace selected cable slings with instrumented cablebolts. Stretch measurement to assess reinforcement technology (SMART) cablebolts, commercially available from Mine Design Technologies (MDT), were selected for the instrumentation programme. SMART cablebolts incorporate a miniature multi-point borehole extensometer (MPBX) recessed within the king wire of a seven-wire strand. By combining the load-carrying capacity of a conventional seven-wire cable with the displacement-monitoring capability of an MPBX, SMART cablebolts enable direct measurement of strain and load distribution along the cable length. The instrument measures displacement at up to six anchor points distributed along the cable as it elongates under tensile loading. SMART cablebolt performance has been demonstrated through laboratory and field trials since 1998 (Hyett et al., 1997; De Graaf et al., 1999). Laboratory testing reported accuracy better than 1.4% (as a percentage of full-scale reading) and a high degree of repeatability (De Graaf et al., 1999).

Instrumented cablebolts are widely used in the mining industry to assess ground support performance (Gauthier et al., 2000; Hyett et al., 1997; De Graaf et al., 1999; Bawden, 2024). However, to the authors' knowledge, they have not previously been applied as part of a monitoring strategy to evaluate the performance of pillar-wrapping cable slings. The SMART cablebolts used in this study were designed to align with the ground support layout and the design specifications of the pillar-wrapping cable slings used in the B3 extraction level.

A prototype configuration was first implemented at K12N (the southern drawpoint of the JK-12 drawbell) and assessed through a trial to confirm instrument functionality and refine the installation methodology (Yanagimura, Hadjigeorgiou, 2022). The prototype was subsequently modified for a comprehensive instrumentation programme at the JK-16 drawpoints (J16S and K16N), which is reported in this paper.

B3 EXT pillar wrapping instrumentation programme

As part of the instrumentation trial at the K12N, the cable slings in the middle row, located 2.2 m from the sill installed in the bullnose

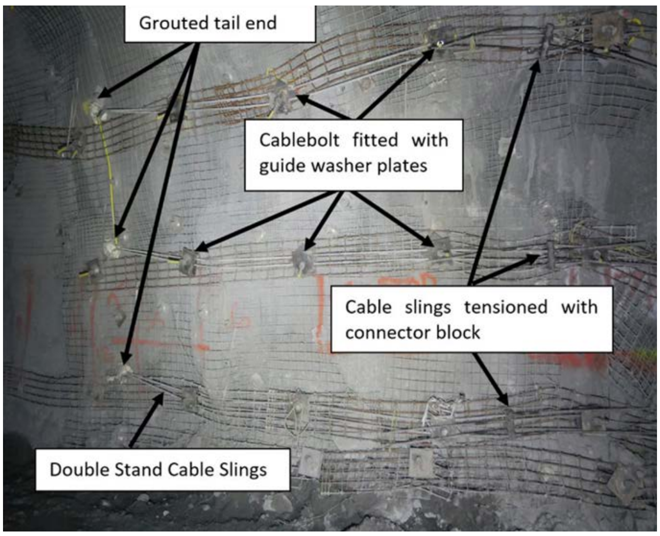

Figure 5—Pillar wrapping cable slings installed in B3 extraction level

and camelback pillar of the K12N drawpoint were instrumented (Yanagimura, Hadjigeorgiou, 2022). Modifications to the instrument length and anchor node locations were made so that the connector block (Figure 6) was better placed on the bullnose to protect from equipment damage and anchor nodes were equidistantly spaced around the bullnose corner (Figure 7).

At JK-16, every row of the double-strand cable slings was instrumented. Installation of both instrumented and non-instrumented cable slings at the J16S drawpoint commenced on March 29, 2022, and the system was fully tensioned by April 7, 2022.

To confirm the final instrument layout relative to the drawpoint pillars, survey pickups of the drillhole collars, anchor nodes, and connector block locations were completed after installation. These pickups provided an important compliance check, verifying that the installation was executed in accordance with the design. Figure 8 shows the layout of the instrumented cables and the corresponding anchor locations along the pillar surface at the J16S drawpoint. Each anchor location was assigned an identifier (e.g., A1.3) based on its distance from the anchor closest to the connector block (A0). Figure 9 shows the completed installation at the J16S drawpoint.

Data analysis and interpretation

This section presents the analysis and interpretation of data collected from the instrumented cable slings installed at the JK-16 drawpoints, covering the period from installation in April 2022 through 1 October 2022. During this interval, advanced undercutting was completed in June 2022, while cave initiation for the B3 mining block remained in progress with ongoing drawbell construction.

Figure 6—Connector block used to tension pillar wrap cable slings at the New Afton mine

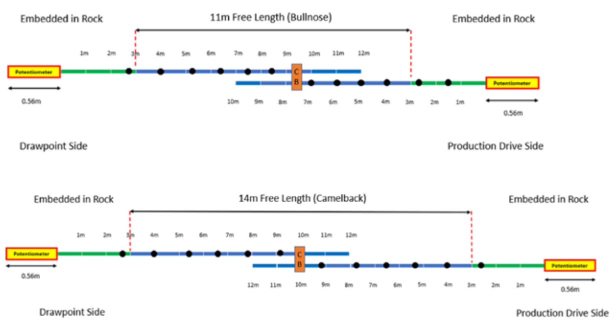

Figure 7—Schematic of SMART cablebolts used to instrument cable slings for the JK-16 instrumentation study: Note that "CB" denotes the planned location of the connector block

Load on instrumented cable slings

Using the relative displacement measured at A0.0—the anchor node farthest from the potentiometer and closest to the connector block—it is possible to estimate the average load mobilised along the full length of each instrumented cable sling. The resulting load estimates for the instrumented cable slings installed in the camelback and bullnose are shown in Figure 10.

At the J16S drawpoint, the cable slings were initially tensioned on 1 April 2022 and re-tensioned on 7 April 2022, after slack was observed in several slings (green arrows in Figure 10). The drawbell blast was fired on 29 April 2022 (red arrow in Figure 11).

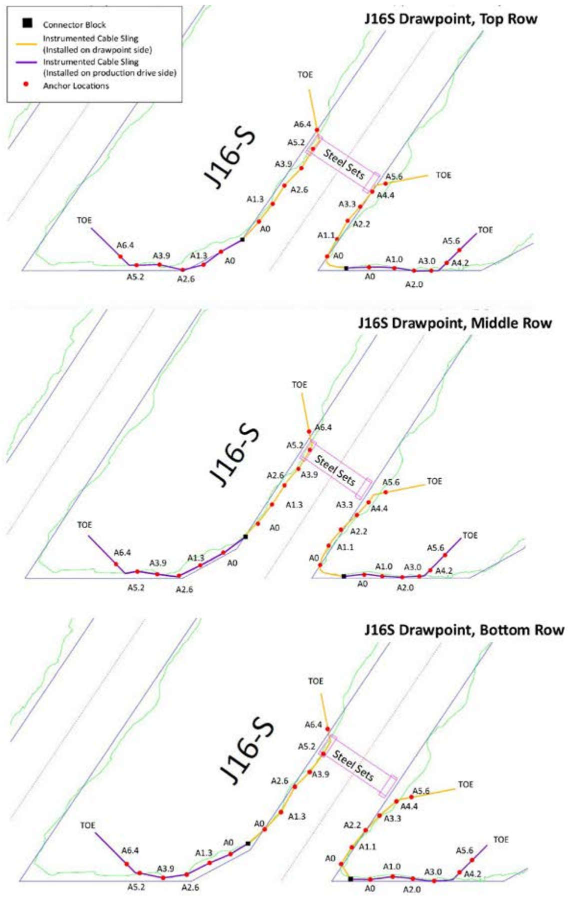

Figure 8—Configuration of SMART cablebolts Installed at J16S drawpoint

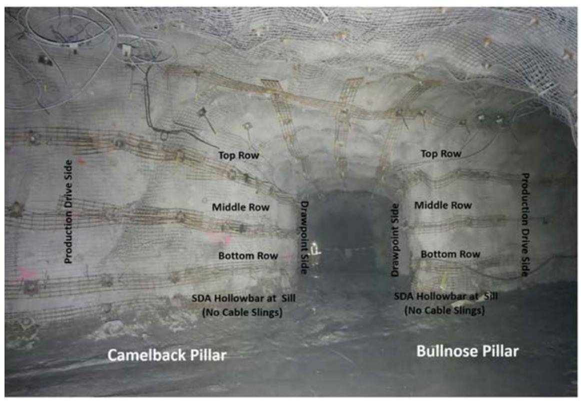

Figure 9—Instrumented cable slings at the J16S drawpoint

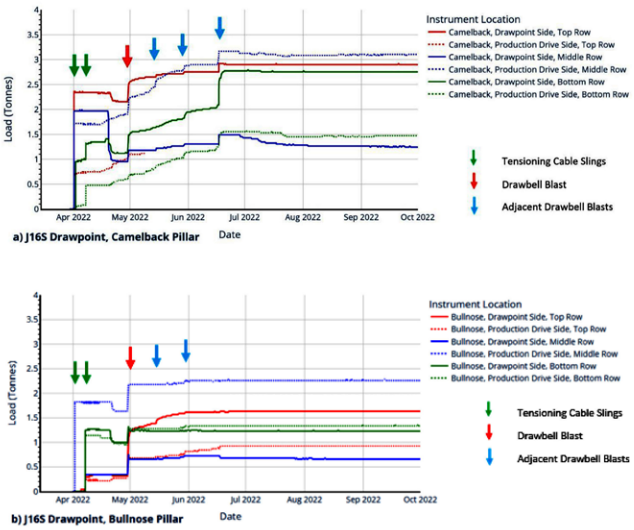

Figure 10—Average load in the J16S cable slings

Table 1

Blast Dates for Drawbells around JK-16

Blast location	Blast date
IJ-15	21 April 2022 day shift
JK-16	29 April 2022 night shift
KL-17	14 May 2022 day shift
IJ-16	29 May 2022 day shift
KL-18	15 June 2022 night shift
JK-17	16 June 2022 night shift

Mining activity, drawbell blasts near the installations, non-intentional contact on cable slings and potentially the heavy use of fibrecrete for steel sets and cover can influence the performance of pillar wrapping cable slings. Table 1 provides the dates of drawbell blasts between April and June 2022, that triggered a response in the JK-16 drawpoints.

A closer review of the load–time history in Figure 10 indicates that several cable slings experienced pronounced unloading between 20 April and 21 April, 2022. Unloading initiated on 20 April at approximately 15:30 and continued progressively until about 21:00 for the camelback (drawpoint side; top and bottom rows) and the bullnose (drawpoint side; bottom row) instrumented cables. For the camelback (drawpoint side; middle row), the unloading response began earlier—on 19 April at approximately 14:30—and continued steadily until approximately 21:00 on 20 April. For the remaining instruments (bullnose, production-drive side; middle and bottom rows), unloading initiated on 21 April at approximately 17:00.

These unloading responses appear to reflect the cables' sensitivity to mining activities in the vicinity of the drawpoint, including work associated with steel-set installation. The unloading observed on 21 April is attributed to the IJ-15 drawbell blast, with the bullnose cable slings at the J16S drawpoint being closest to the blast location.

Relative displacement of the grouted cable tail end

The instrumentation was designed such that the anchor node(s) closest to the potentiometer toe were embedded within the grouted tail end of the cable. Referring to Figure 7, these correspond to A6.4 for the camelback instruments, A5.6 for the bullnose instrument on the production-drive side, and A5.6 and A4.2 for the bullnose instruments on the drawpoint side. The relative displacement time histories (Figure 11) were used to examine the behaviour of the anchor nodes located within the grouted tail relative to those along the free cable length.

The results indicate that the grouted tail at the J16S drawpoint performed as intended. For a well-bonded cable, the shear stiffness of the grout–cable interface is expected to restrict displacement within the cable tail as tensile load is transferred from the free length back into the rock mass. Consistent with this behaviour, displacements measured at the grouted anchor nodes were very small compared with those measured along the free length following sling tensioning and the drawbell blast. At the time of tensioning, displacement at the grouted anchors remained near zero, reflecting the relatively low initial tensile load applied to the sling and the effective restraint provided by the grouted section.

In effect, when the grouted tail is functioning properly, the available interface shear resistance exceeds the shear demand induced by tensile loading and any pull-out forces mobilised within the pillar-wrapping system. This limits displacement in the grouted tail and enables the tensile load carried by the sling to be mobilised primarily within the free length and transferred back into the rock mass through the grout–cable interface.

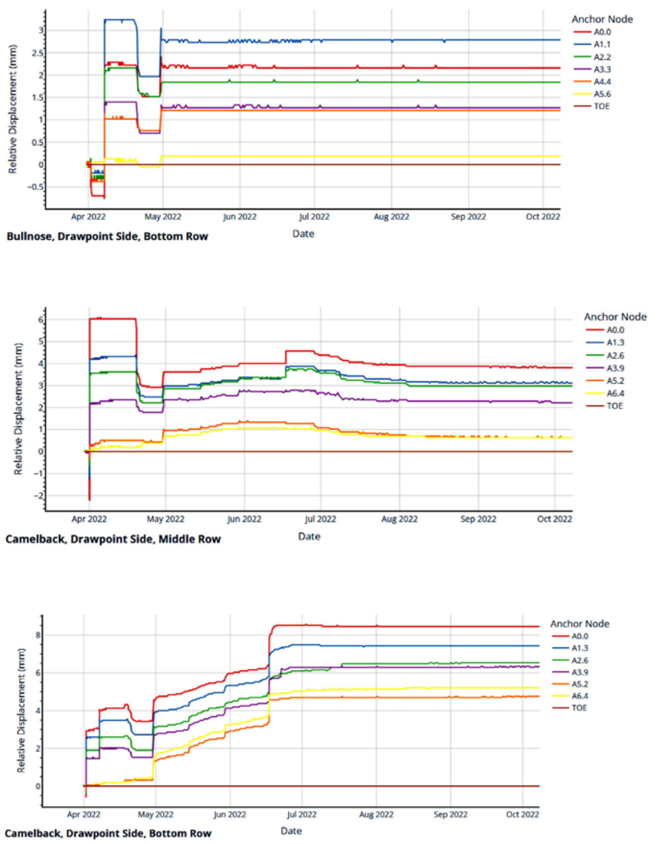

Figure 11—Instrumented cable slings from J16S drawpoint showing limited displacement at grouted tail end. Note that the instruments have one anchor node, A5.6 or A6.4, in the grouted tail end

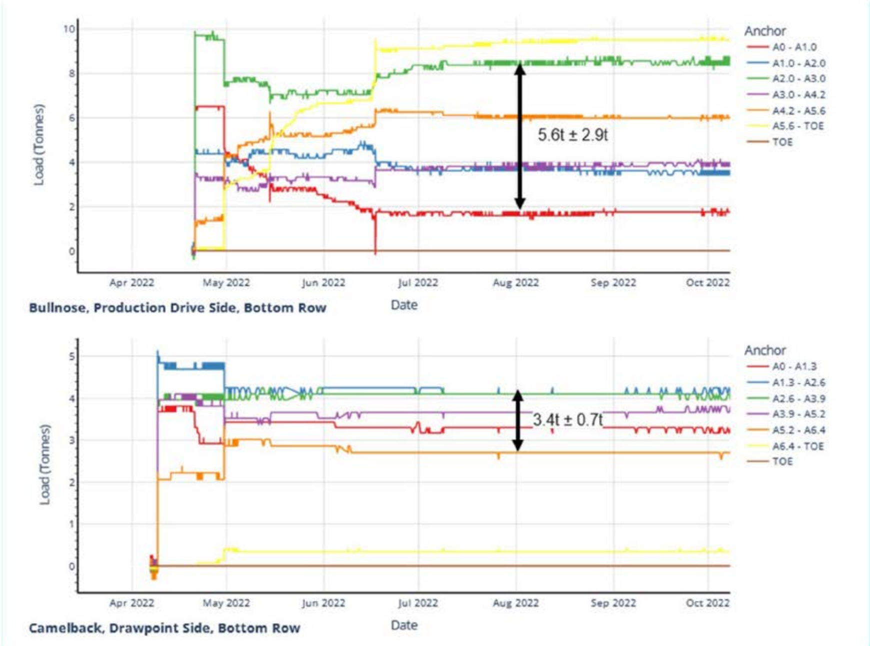

Figure 12—Load distribution along the pillar wrapping cablebolts at JK-16

Load distribution along cable slings

A review of the instrumentation data indicates that load distribution along the pillar-wrapping cablebolts can vary substantially during the early stages of installation. As shown in Figure 12, drawbell blasts can trigger a redistribution of load along the cable free length when the loads retained in the cable slings are still relatively low. In some cases, the cable slings exhibited the desired convergent loading response following the drawbell blast, which is beneficial for long-term performance. However, cablebolts that displayed a divergent loading response are a concern, as this behaviour can concentrate load over a short segment and increase the potential for premature, localised failure.

Divergent loading can be partially attributed to pinching or shear loading at the guide washer plates, adhesion between the cable and the shotcrete cover spray, and irregular excavation surface profiles. These conditions can promote load concentration and inhibit efficient load transfer along the cablebolt free length, thereby limiting the development of a more uniform load distribution. Overall, these observations underscore the need for strict installation quality control to facilitate effective load transfer and achieve consistent cablebolt performance.

Recommendations for pillar wrapping

The comprehensive instrumentation programme complemented the routine field observations at the B3 extraction level and identified early stages of installation factors that can influence the long-term performance of pillar wrapping cable slings. A review of instrumentation data during the early caving process facilitated the development of practical design and implementation recommendations.

Cable sling design

Bond stiffness at the grouted tail end is critical to the long-term performance of pillar-wrapping cable slings. Insufficient shear stiffness at the tail can lead to premature failure under blast-induced loading. Performance can be improved through the following measures:

- ➤ **Use modified-geometry cables:** Modified-geometry strands can achieve higher bond capacity than plain strand cables, reducing sensitivity to grout quality and improving load transfer.
- ➤ **Increase embedment length:** Greater embedment improves confinement and bond performance, helping to ensure anchorage within the confined pillar core. Extensometer data can be used to estimate the depth of rock-mass fracturing so that embedment extends beyond the disturbed zone.
- ➤ **Avoid mechanical anchors unless necessary:** Expansion shells (e.g., CL65) can provide mechanical anchorage but are costly and tend to perform poorly in weak or deteriorated ground. Modified geometry cables are typically more practical and cost-effective.
- ➤ **Maintain rigorous quality control**: This includes confirming borehole length and inclination to achieve the specified embedment, visually inspecting cables to ensure they are free of contaminants (rust, grease, dust, paint), and sampling grout to verify strength and water-to-cement ratio meet specification.

By improving cable geometry, ensuring adequate embedment, and enforcing strong quality control, cable slings are more likely to withstand blast impacts and provide reliable long-term performance, reducing reliance on contingency installations intended to compensate for early-life failures.

Shotcrete spray and tensioning cable slings

Instrumentation data indicate that load transfer along the cable slings is initially limited but improves as loading increases. Early-stage load-transfer efficiency can be reduced by irregular excavation wall profiles, suboptimal guide washer design, interaction with adjacent support elements, and adhesion between the cable and shotcrete.

Table 2
Standard of quality for installing cable slings for pillar wrapping

Quality/design requirements	Example quality control measures	Consequence of Not Correcting Defective Work
Cable are tails installed to the design embedment length.	Routine checks of drilled borehole length.	Insufficient bond strength or anchorage into pillar core may cause premature failure of cable sling at the cable-grout interface.
Drill angle at 45° to 60°	Routine checks of drilled borehole angle.	Unintended shear loading of cable sling at the borehole collar. Shear loading can reduce the overall capacity of the cable.
Bolts with custom guide washer plates are installed along the design row and ring spacing.	Check mark up of bolt location and after it has been drilled.	Unintended shear loading on cable sling along the free length by guide washer plates if the bolt deviates from row spacing. Widely spaced bolts may cause cable slings to not be pinned tightly to wall once tensioned.
Grout strength meets minimum target (e.g., 40 MPa) and mixed at specified water to cement ratio.	Sample grout mixtures for density and strength testing. Job task observation with the grouting crew.	Insufficient bond strength or anchorage into pillar core may cause premature failure of cable sling at the cable-grout interface.
No binding or pinching of cable slings under the guide washer plates.	Visual inspection of the cable sling along the free length. Job task observation with the tensioning crew.	Load transfer efficiency is diminished along the free length of the cable.
Excavation surface is devoid of sharp corners; ensure regular profile.	Visual inspection of the excavation surface before drilling.	Unintended point loading on the cable sling, can diminish load transfer efficiency and/or reduce the overall capacity of the cable.
Cable surface is clean before installation into boreholes.	Routine checks of cable surface in storage and during install.	Insufficient bond strength. Less sensitive if bulbs are on the cable tail end.
Cable slings are tensioned to design jack load.	Routine check of slack on cable slings. Job task observation with the tensioning crew.	Cable slings act as passive support systems. Pillar movement is required for the cable slings to commence work.
No rotation in the connector block once the cable slings are tensioned.	Visual observation of the connector block. Job task observation with the tensioning crew.	Some of the cable slings that are part of the same system may have become unloaded during the tensioning of one of the other cable slings.
Connector blocks are positioned to a location least impacted by equipment damage.	Visual observation of the connector block. Job task observation with the tensioning crew.	Equipment damage to the connector block may cause sudden loss of tension on the cable slings as the cable slips through the wedge.
Secondary shotcrete spray provides full coverage over cable slings.	Visual observation of the shotcrete cover.	Equipment damage to exposed cable slings may cause irreparable damage.

Covering exposed cables with shotcrete is beneficial for protecting the slings from equipment damage; however, adhesion between shotcrete and the cable can inhibit cable movement and reduce load-transfer efficiency. Laubscher (2000) suggested using polypipes to prevent bonding, but this approach was found to be time-consuming and offered limited benefit. A more practical alternative is to apply a thick, inert grease to exposed cable sections prior to shotcrete spraying. At New Afton, this practice has improved load transfer, although additional testing is required to quantify the magnitude of the benefit.

Cable tensioning should also account for significant losses between the applied jack load and the residual load retained in the sling—often on the order of 30% to 90%—largely due to the jack configuration and installation setup. At New Afton, cables are tensioned using a hollow rod to avoid interference with wall-mounted equipment. To achieve target residual loads, it is therefore critical to quantify these losses as part of installation. While instrumented cablebolts provide detailed insight, a simpler field test using a load cell can be used to estimate jack-to-residual load losses and confirm that slack has been fully removed following tensioning.

Quality control

Given the number of steps involved in installing pillar-wrapping cable slings, rigorous quality control is essential to identify and correct defects early. The most effective approach is to develop a quality management plan and review it with the construction crew and key stakeholders prior to commencing work. Implementing the plan provides a structured framework for maintaining consistent quality throughout installation.

Table 2 summarises baseline quality standards to consider when establishing quality control measures for pillar-wrapping cable sling installation. Job task observations are a critical component, as they verify that operators are following standard procedures in the field. Any deficiencies or non-conformances identified should be documented and addressed promptly through corrective actions.

Operational factors

Preliminary trials and the full-scale trial reported in this paper indicate that ground support interaction during drilling is more common than anticipated. In block caving, pillar-wrapping cable slings frequently intersect previously installed cablebolts that are installed at systematic spacings. Because cable slings are not always drilled perpendicular to the excavation wall, the tail sections can intersect or interfere with existing reinforcement elements. If the installation sequence is not optimised to minimise drilling-related damage, the load-bearing capacity of the slings may be reduced. Unfortunately, drilling-related damage to reinforcement is often difficult to detect in the field.

Field inspections also indicated that repetitive impacts—particularly from LHDs constructing berms at drawpoints to manage mud rush and hang-ups—frequently damaged cable slings along the upper walls and shoulders. Applying a shotcrete cover in these areas is therefore essential to protect the cable slings from equipment-related damage.

Conclusions

Pillar wrapping using cable slings is a surface support system employed at block cave operations worldwide to reinforce drawpoint pillars on the extraction level. In poor-quality, highly fractured ground, overstressing of the extraction-level rock mass can drive significant deformation and convergence, increasing safety risk and potentially causing production delays and/or reserve losses.

Cable slings are designed to provide high yielding capacity, allowing them to accommodate large ground movements while continuing to confine the rock mass as it transitions into, and progresses through, post-peak behaviour. Despite their widespread application in cave mining, a technical review of pillar-wrapping cable slings identified a limited body of published information describing their design basis and field performance.

An instrumentation study conducted on New Afton's B3 extraction level was undertaken to quantify the performance of cable slings installed in drawpoint corners during the early stages of caving. The programme focused on the cave initiation and early propagation phases of the B3 cave life cycle, with particular emphasis on sling response to undercutting activities and drawbell blasting. Data from the instrumented cables provided valuable insight into load transfer and deformation behaviour, demonstrated the QVP of deploying pillar-wrapping cable slings at New Afton—by linking installation quality and system performance to tangible operational risk reduction—and informed practical recommendations to improve installation quality and maximise the performance benefits of cable slings in the field.

Acknowledgements

The authors acknowledge the financial support from New Gold Inc (now Coeur Mining Inc.) This project would not have been possible without the continued support of mine operations (rehabilitation/construction), automation. The geotechnical team at New Afton mine made significant contributions to the instrumentation project. Corey Kamp (New Gold Inc.), Peter Lausch (MDT), Professor Will Bawden and Sami Talu (Rio Tinto) have provided additional background and useful suggestions.

References

Bawden W.F. 2024. Forgotten critical limitations on cablebolt reinforcement design and guidelines for instrumentation deployment to monitor support behaviour and capacity consumption. Deep Mining 2024, Montreal, P. Andrieux & D. Cumming-Potvin (eds). Australian Centre for Geomechanics.

Bieniawski, Z.T. 1989. Engineering rock mass classifications: a complete manual for engineers and geologists in mining, civil, and petroleum engineering. John Wiley & Sons, New York.

Castle, B.R., Scott, J.J. 1982. Cable slings - A versatile 'band-aid' for providing safety in underground mining. Proceedings of 1st AIME-SME International Conference on Stability in Underground Mining, pp. 978 – 993.

De Graaf, P.J., Hyett, A.J., Lausch, P, Bawden, W.F., Yao, M. 1999. Hudson Bay Mining and Smelting Co.'s field trials using 'SMART' technology–successful ground support design through in situ cablebolt performance evaluation. Proceedings of the 101st Annual General Meeting of the Canadian Institute of Mining, Metallurgy and Petroleum, Calgary.

Gauthier, P. 2000. Cablebolt optimization at Mine Bousquet. Proceedings of the 15th Ground Control Colloque, Quebec Mining Association.

Hyett, A.J., Bawden, W.F., Lausch, P., Ruest, M., Henning, J., Baillargeon, M. 1997. The SMART Cablebolt: An Instrument for the determination of tension in 7-wire strand cablebolts. Proceedings of the 1st Asian Rock Mechanics Symposium, Balkema, Seoul, pp. 883 – 889.

Jakubec, J. 1992. Support at Cassiar Underground Mine. MASSMIN 92, H.W. Glen (ed), SAIMM, Johannesburg, pp. 111-123.

Laubscher, D.H. 2000. Block Caving Manual. Prepared for International Caving Study, JKMRC and Itasca Consulting Group, Inc, Brisbane.

Stacey, T.R., Hadjigeorgiou, J. 2022. Quantified value-created process (QVP) – a value-based criterion for mine design and operating decisions. *Journal of the Southern African Institute of Mining and Metallurgy*, vol. 122, no. 2, pp. 73–82.

Wilson, A.D., Talu, M.S. 2004. A Review of the Support Systems Being Applied to the Block 4 Cave Project of De Beers Finsch Mine', South Africa. MASSMIN 2004, A Karzulovic & MA Alfaro (eds), Instituto de Ingenieros de Chile, Santiago.

Yanagimura, Y., Hadjigeorgiou, J. 2022. A monitoring strategy to assess the effectiveness of pillar wrapping. Fifth International Conference on Block and Sublevel Caving. Caving 2022, Y. Potvin (Ed). Australian Centre for Geomechanics, pp. 501 – 516. ◆

Accelerated corrosion investigations on mechanical hybrid rockbolt steel

by F.D. Agrensa[1], J. Hadjigeorgiou[1], S.J. Thorpe[1]

Affiliation:
[1] University of Toronto, Toronto, Ontario, Canada

Correspondence to:
J. Hadjigeorgiou

Email:
john.hadjigeorgiou@utoronto.ca

Dates:
Received: 09 Dec. 2025
Revised: .13 Jul. 2026
Accepted: 28 Jul. 2026
Published: Aug. 2026

How to cite:
Agrensa, F.D., Hadjigeorgiou, J., Thorpe, S.J. 2026. Accelerated corrosion investigations on mechanical hybrid rockbolt steel. *Journal of the Southern African Institute of Mining and Metallurgy*, vol. 126, no. 8, pp. 491 – 502

DOI ID:
https://doi.org/10.17159/2411-9717/3868/2026

ORCiD:
F.D. Agrensa
https://orcid.org/0009-0007-1625-2308
J. Hadjigeorgiou
https://orcid.org/0000-0002-6047-3964
S.J. Thorpe
https://orcid.org/0000-0001-8263-2498

Abstract

The recent introduction in underground mines of mechanical hybrid rockbolts has been driven by efforts to eliminate the use of resin in heavily fractured ground. Mechanical hybrid rockbolts consists of a steel tendon mechanically anchored within a friction unit. Installation of mechanical hybrid rockbolts is percussion-driven by the rock drill and the mechanical anchor is subsequently activated using rotation. The bolt configuration and installation process overcome issues associated with hole closures and the use of resin.
Recent work has focused on understanding the behaviour of the rockbolts under quasi-static and dynamic conditions but there is scant information on the anticipated performance in corrosive underground environments. This paper reports the results of a comprehensive accelerated corrosion investigation of the principal components of mechanical hybrid rockbolt. This can aid in establishing the long-term suitability of mechanical hybrid rockbolt in corrosive environments.

Keywords

Mechanical hybrid rockbolts (MHR), steel tendon and friction unit, steel properties, accelerated corrosion, long-term performance

Introduction

The selection of rock reinforcement for underground excavations in rock requires matching the anticipated capacity and deformation for the anticipated loads. To achieve the design capacity of a particular rockbolt is the ability for it to be installed under adverse conditions such as highly stressed, friable, and fractured ground. An additional challenge is ensuring the long-term performance of installed ground support elements over time. Corrosion is one of the contributing factors that can result in degradation and possible failure of a rock reinforcement element.

In highly stressed, friable, and fractured rock the effectiveness of resin-grouted rockbolts can be limited. This is associated with resin migration into joints that can result in gaps or voids along the rockbolt bar, not attaining the full column and partially mixed resin grout penetrating the rock mass. Another concern is that borehole closures can prevent the installation of resin cartridges. These scenarios can result in a poorly installed resin grouted rockbolt not reaching its design capacity.

Mechanical hybrid rockbolts (MHR) are a relatively recent addition to rock reinforcement options for difficult installation conditions. MHR employs a specifically designed mechanical point anchor bolt installed inside a friction rock stabiliser. Limited tests at Mount Charlotte suggested that the configuration of a specially designed mechanical anchor installed in a friction rock stabiliser provided good static capacity (Carlton et al., 2013). Andrews (2019) reported that MHR have been successfully implemented in highly stressed and fractured rock mass conditions at mine sites in Australia and South Africa.

There are two fundamental concerns for the widespread application of MHR. The first is the absence of supporting quantifiable data on the performance of the mechanical friction bolts under a range of loading conditions and their potential susceptibility to corrosion making them not a good option for long term applications in corrosive environments.

Recent work by Knox and Hadjigeorgiou (2024a) provided the first significant data on the load displacement behaviour of MHR under different loading configurations ranging from 0^0 (axial load) to 30^0 (a combination of axial and shear with the axial load being dominant), to 60^0 (where the shear component becomes dominant over the axial load), and pure shear (90^0).

There is surprisingly more information on the behaviour of different MHR under impact testing using the continuous tube configuration, as reported by Darlington et al. (2019), Vallati et al. (2022), Evans (2022), and more recently by Knox and Hadjigeorgiou (2024b). The justification for the use of the continuous tube configuration is based on the design and energy dissipation function of the rockbolt. The tendon anchored within the friction unit of an MHR is assumed to be loaded independently, consequently, the direct loading of the tendons is justifiable.

This paper aims to address a knowledge gap specific to the susceptibility to corrosion of MHR. A deep and high stress underground mine was exploring the use of MHR in areas that were potentially susceptible to corrosion. As part of a comprehensive investigation of new products, the mine investigated the susceptibility to corrosion of two commercially available MHRs, the MD rockbolt (Sandvik, 2025) and the Vulcan rockbolt (Epiroc, 2025).

As illustrated in Figure 1, both MHR employ a solid bar/rebar inside a friction unit with an anchor near or at the distal end. The mechanical dynamic (MD) bolt head comprises a ring welded onto the friction unit, a nut, and another ring attached to the rebar. This allows both the friction unit and the rebar to directly sustain any axial load induced by the movement of the rock mass. In the Vulcan bolt, the plate is attached to the bar connected through the spherical seat, the load indicator, and the nut. Consequently, the bar will predominantly sustain an induced axial load due to a rock mass movement near the bolt head. In both cases, the reinforcement mechanism can only be achieved if the anchor is successfully activated.

In the absence of long-term exposure data, there is a significant knowledge gap on the susceptibility to corrosion of MHR. Determining the susceptibility of rockbolts to corrosion of ground support requires a knowledge of the steel properties, rockbolt configuration, and the exposure time and severity of the environment. This investigation focused on the steel properties of the main components of the rockbolts in a succession of accelerated corrosion experiments. The influence of the chemical composition and the steel microstructures was also discussed.

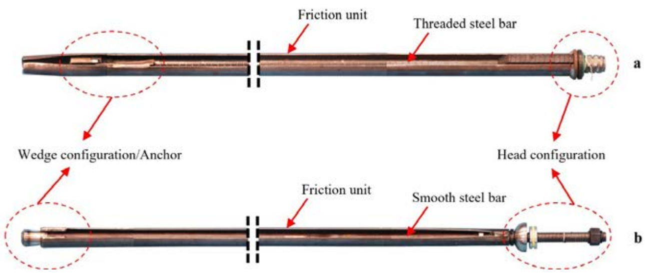

Figure 1—Configuration of two MHR: a. MD bolt b. Vulcan bolt

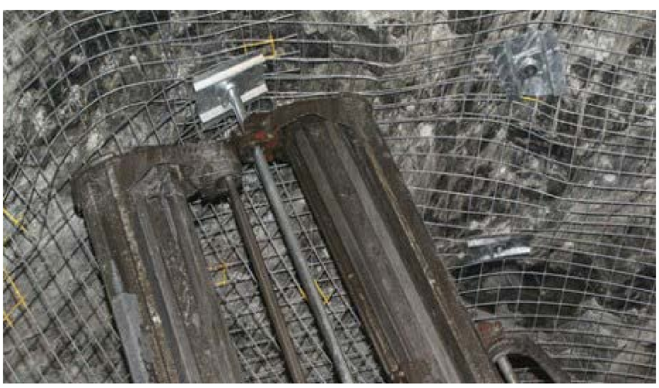
Figure 2—MHR installation using a twin boom drill rig, (Knox, Hadjigeorgiou, 2024b)

Installation considerations

MHR can be installed using a range of equipment including platform bolters, specialised bolters, and twin boom drill rigs, as per Figure 2. The MHR used in this investigation employs similar installation procedures, illustrated in Figure 3.

A borehole is drilled with a bit diameter smaller than the outer diameter of the friction unit component. The rockbolt, with a faceplate attached, is then driven into the borehole through the percussive force of the bolter. After the rockbolt is fully inserted, a torque is applied to the nut on the bolt head. Consequently, the anchor is pulled toward the bolt head, leading to an expansion of the wedge. The wedge expansion can reach up to 52 mm for the MD bolt, while the anchor of the Vulcan bolt with a 39 mm friction unit diameter can be expanded to approximately 43 mm in diameter. When the anchor is successfully activated, tension stress is induced along the rebar/bar component. As a result, an immediate reinforcing action is exerted on the rock mass.

Susceptibility to corrosion

The majority of rockbolts installed at underground mines are manufactured using low-carbon steels containing a variety of alloying elements. The chemical composition of steel controls its strength, hardenability, formability, weldability, ductility, and susceptibility to corrosion. In practice, multiple combinations of

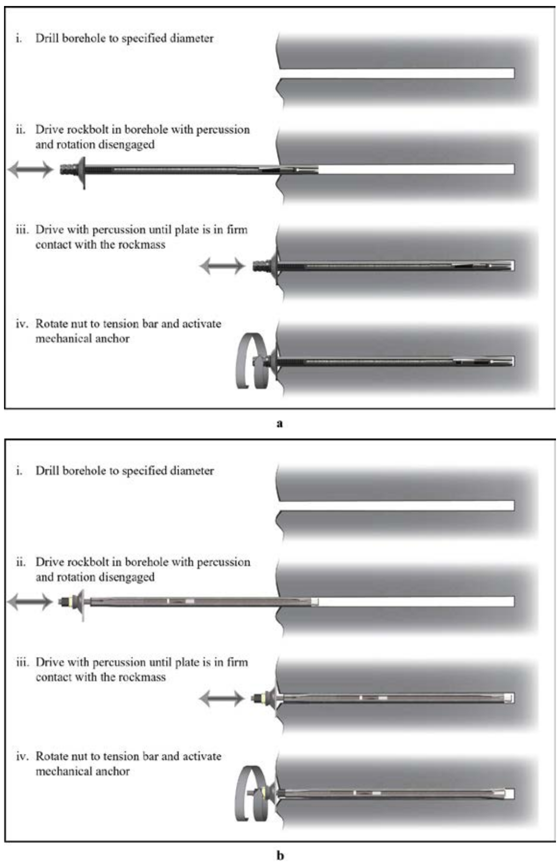

Figure 3—Installation steps for: a. MD bolt b. Vulcan bolt (Knox, Hadjigeorgiou, 2023)

alloying elements can be used to meet the mechanical performance requirements of steel and rockbolts.

In underground mining environments, rockbolts are exposed to a range of corrosive environments. Atmospheric corrosion is controlled by factors such as temperature, relative humidity, airflow, and the presence of pollutants (Hadjigeorgiou et al., 2008). As the water vapour condenses onto the rockbolt, it triggers an electrochemical reaction. Aqueous corrosion occurs due to exposure to underground mine water. Rockbolts exposed to an aqueous environment are generally more susceptible to corrosion than those undergoing atmospheric corrosion.

Along with the water temperature, various parameters that indicate the presence of chemical species exacerbating the corrosion rate can be used to characterise the environment, such as pH, conductivity, total dissolved solids (TDS), the dissolved oxygen (DO) level, and concentration of aggressive anions (Cl^-, SO_4^{-2}, etc.). In addition, microorganisms present in the water can facilitate or inhibit the corrosion of rockbolts (Craig et al., 2016; Dorion, Hadjigeorgiou, 2020).The pH measures the concentration of H^+-ions in the solution, which also indicates the acidity/alkalinity of the solution. A solution with a higher concentration of H^+ will lead to a lower pH level. The dissolved oxygen (DO) is a measure of oxygen, a strong oxidising agent in the solution. The rate of mass transfer for chemical species is temperature-dependent. As the corrosion reaction involves an electron transfer step, the rate of electricity passing through a solution (conductivity) can also be an indicator. The total dissolved solid (TDS) measures the concentration of the dissolved substance in the solution. As the previously mentioned parameters increase, the corrosivity of the environment will consequently increase, resulting in an elevated corrosion rate. The influence of aggressive anions, e.g., Cl^- and SO_4^{-2}, affect not only the general corrosion rate but are also associated with localised forms of attack such as pitting corrosion. Since pitting corrosion rates may be orders of magnitude greater than general corrosion rates, the latter may not be a representative indicator for long-term bolt integrity. The lowered rate is due to the decreased solubility of oxygen in the presence of the dissolved NaCl. A significant mass loss occurring at the pit will negatively affect the structural integrity of the metal by acting as a point of stress concentration and crack nucleation.

The susceptibility of any rockbolt to corrosion is a complex process influenced by multiple parameters, including the corrosive environment, the rockbolt configuration, and the material properties. The corrosion rate of rockbolt steel depends on various factors when the rockbolts are exposed to an aqueous corrosive environment. The influencing factors can be generally divided into two: the corrosivity of the aqueous environment or the solution and the corrosion resistance of the steel. The corrosivity of the aqueous environment, or the external factors to the rockbolt material, is associated with the presence of chemical species and microbacteria or temperatures that affect the kinetics behaviour of the corrosion reaction. The corrosion resistance of the steel material is attributed to the presence of a protective coating, the alloying elements, and the resultant microstructure upon fabrication.

Dorion and Hadjigeorgiou (2014) provided a high-level comparison between ground support elements and their susceptibility to corrosion. Although these guidelines are used at mine sites to select appropriate rockbolts in a range of corrosive environments it is limited in that it does not include MHR. Given the short history of MHR there are no empirical data at this time to assess their corrosion susceptibility. This is of concern given that they employ a two-component system (friction unit and rebar/rod) that, in the absence of a resin, is likely to be susceptible to corrosion. This may limit the application of mechanical hybrid rockbolts to relatively short-term applications in corrosive environments, thus, the driving force for ongoing work at the University of Toronto on the long-term performance of MHR in corrosive environments. The present work reports on the results of a research programme focused on the influence of the chemical composition and the resultant steel microstructure of the main components of MHR using accelerated corrosion experiments.

Experimental investigations

The objective of this investigation was to provide a first set of data on the potential corrosion susceptibility of the recently developed MHR. To this end, two MHR from different suppliers have been subjected to a series of electrochemical tests. Of interest is that mechanical hybrid rockbolts comprise two distinct main components, the rebar/rod and the friction unit, which use different

Table 1

Chemical composition of steels for MHR (in weight%)

Element		**C (%)**	**Mn (%)**	**P (%)**	**S (%)**	**Si (%)**	**Cu (%)**	**Ni (%)**	**Cr (%)**
MHR #1	Tendon/bar	0.229	1.44	0.024	0.025	0.59	0.02	0.01	0.04
	Friction unit	0.188	0.83	0.025	0.021	0.34	0.02	0.01	0.03
MHR #2	Tendon/bar	0.230	1.46	0.013	0.004	0.62	0.10	0.07	0.10
	Friction unit	0.091	1.14	0.008	0.003	0.20	0.01	0.01	0.02
Element		V (%)	Mo (%)	Al (%)	Co (%)	Ti (%)	Pb (%)	Nb (%)	Fe (%)
MHR #1	Tendon/bar	0.05	<0.01	<0.01	<0.01	<0.01	<0.01	0.01	Balance
	Friction unit	0.02	<0.01	<0.01	0.01	<0.01	<0.01	0.02	Balance
MHR #2	Tendon/bar	0.07	0.02	<0.01	<0.01	<0.01	<0.01	0.01	Balance
	Friction unit	<0.01	<0.01	0.04	<0.01	0.02	<0.01	0.03	Balance

steels. The concern was whether there was significant variation between the corrosion behaviour of the two components and between different products.

Although both commercially available rockbolt types are also available with a protective galvanisation coating, this investigation aimed to quantify the anticipated corrosion rate of the core steel when exposed to an aggressive environment. This investigation established the chemical composition of the different steel components, the resulting material hardness, and the susceptibility of the employed steel components to corrosion when exposed to an aggressive environment. The paper reports the results of these investigations with reference to MHR #1 and MHR #2.

Chemical composition of the mechanical hybrid rockbolts

The chemical composition of steel for each rockbolt component was determined through inductively coupled plasma atomic emission spectroscopy/optical emission spectroscopy (ICP-AES/ICP-OES) and carbon and sulphur analysis as per ASTM E1479-16 and ASTM E1019-11, respectively. The chemical composition of each component is summarised in Table 1. The reported value is the average value out of three samples. The variance among samples prepared from the same component of a specific rockbolt tested was negligible.

A comparison of the chemical composition between the bar and friction unit steels indicates that the bar/tendon component has a higher concentration of C, Mn, Si, Cr, and V than the friction unit component on the same MHR product. This is reasonable as the bar component is the primary component of the rockbolt that is expected to sustain most of the imposed load. Furthermore, these elements are associated with increased strength through either precipitation of carbides, or interstitial and substitutional solid solution hardening.

From a corrosion perspective, the corrosion resistance of the bar steel of MHR #2 was expected to be lower than that of the friction unit component due to a higher difference in the mass fraction of C and P. However, this should be ameliorated with higher Si and Cr contents. Based on the S content, MHR #2 has the cleanest steel chemistry. The presence of S will increase the probability of MnS inclusion formation, adversely affecting the mechanical and corrosion resistance. MHR #1 also has an appreciably higher P content, potentially leading to poor corrosion performance. There is no significant difference in the mass fraction of the elements associated with enhancing the protective nature of the oxide layer among the rockbolts.

Material hardness of steel for MHR

To investigate the mechanical properties of steel materials for MHR, Rockwell hardness B tests were performed in accordance with ASTM E18-22. The HRBW value was determined by measuring the depth of indentation induced by pushing a 1.588 mm tungsten carbide ball indenter at 100 kgf of total test force into the steel sample. Prior to the test, the surface of the steel sample was ground by using 1200-grit SiC paper. Conversion from HRBW to the approximate tensile strength was made based on the conversion table provided by ISO 18265:2013. Minimum tensile strength values suggested by ASTM F432-19 and ASTM A1011/A1011M-23 were determined for comparison purposes. It should be noted that the difference in the minimum tensile strength is attributed to the different components and steel grades specified by suppliers.

All steel materials complied with the requirements stated in the ASTM (Table 2). In both MHR, the rebar/bar steel has a higher hardness than the friction unit steel on the same product. Moreover, the difference in the hardness of both bars was significant, while the friction unit of both products had similar hardness.

Steel microstructure

In addition to the chemical composition of the steel, understanding the microstructural constituents in an MHR can help interpret the corrosion performance by focusing on the role of grain size, stable phases and their volume fraction, grain boundaries, etc. Based on this information, the specific role of some alloying elements can be further investigated, particularly in terms of their association with the variation in corrosion performance. While the final microstructure is fundamentally a function of the chemical composition of steel and the heat treatment, the discussion is focused on the stable phases and their effects on the corrosion resistance of steel.

To obtain the microstructural information of each component from both MHR products, a sample was first prepared by sectioning the main component of the rockbolt. The sample surface was then progressively ground using 400-, 600-, and 1200-grit SiC paper before being subjected to a 2-step polishing process. In this stage, a mirror-like surface was obtained using two consecutive polishing steps with 3 μm and 1 μm diamond paste. The microstructure was revealed by etching the surface with Nital (2.5 vol% HNO_3 in ethanol). Scanning electron microscopy (SEM/EDX) was used for imaging and phase identification (Hitachi SU3500).

Figure 4 summarises the micrographs of each sample. In general, the bar and the friction unit of the MHR #1 and the bar for the MHR #2 were identified as a mixture of pearlite and primary alpha ferrite, where the α-ferrite is the matrix phase. The steel for MHR #2 friction unit has the least amount of pearlitic phase in its ferrite matrix. A trace of inclusions was also seen on both mechanical hybrid rockbolt samples, and these were more

Table 2

Rockwell B hardness and approximate tensile strength of steel material for MHR

Hardness test	MHR #1		MHR #2	
	Bar	Friction unit	Bar	Friction unit
Rockwell B Hardness (HRBW)	92.3 ± 1.5	90.4 ± 0.2	95.9 ± 0.6	90.3 ± 0.3
Approximate tensile strength (ISO 18265:2013)	655 ± 24 MPa	624 ± 4 MPa	721 ± 14 MPa	622 ± 4 MPa
Minimum tensile strength (ASTM F432-19 and ASTM A1011/A1011M-23)	620 MPa	480 MPa	690 MPa	480 MPa

apparent on the MHR #1 components. Image analysis using ImageJ software was performed on three micrographs of each steel sample to quantify the volume fraction of the pearlite phase and inclusions. Comparison of the volume fraction of these microconstituents among steel samples is summarised in Table 3. In general, the steel for the bar component has a higher pearlitic volume fraction than the friction unit steel on the same MHR sample, consistent with the higher carbon content as reported in Table 1. A significantly higher volume fraction of inclusions was identified on the friction unit steel of the MHR #1.

The electrochemical properties of microconstituents and the associated volume fraction present in the steel will influence the susceptibility to corrosion. Variations in the corrosion rate of carbon steel as a function of various microstructures were reported by Clover et al. (2005), where an increased corrosion resistance of predominantly very fine ferrite microstructure was observed compared to a banded ferrite-pearlite microstructure. Cementite (Fe_3C) in an acidic chloride solution is more noble and corrosion-resistant than ferrite (Kadowaki et al., 2019). When the cementite and ferrite are coupled and exposed to a corrosive solution, galvanic corrosion will occur, accelerating the corrosion rate as the cementite will serve as a cathodic site. Although the cementite in pearlitic steel is inert due to the galvanic coupling, preferential corrosion of the ferrite-cementite interface will eventually cause the ejection of the cementite phase (Hayden et al., 2022). As a consequence, more steel surfaces will be exposed to the solution. Similar effects of sulphide inclusion, e.g., MnS, on the overall corrosion performance of steel

Table 3

Volume fractions of pearlitic phase and inclusion on steel for MHR based on image analysis

	Component	$V_{pearlite}$ (%)	$V_{inclusion}$ (%)
MHR #1	Bar	34.14 ± 6.55	0.07 ± 0.05
	Friction unit	20.64 ± 6.03	0.28 ± 0.03
MHR #2	Bar	37.24 ± 1.56	0.02 ± 0.01
	Friction unit	0.85 ± 0.65	0.07 ± 0.02

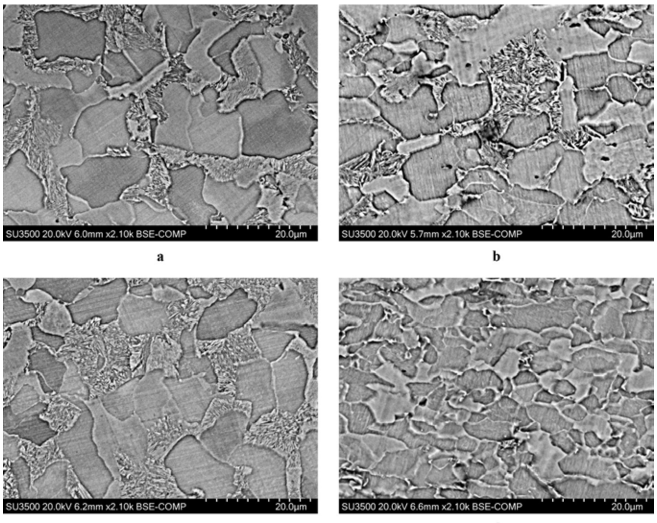

Figure 4—Microstructures of steels for: a. Bar of MHR #1 b. Friction unit of MHR #1 c. Bar of MHR #2 d. Friction Unit of MHR #2

can also be interpreted since the inclusion is more noble than the Fe matrix (Janik-Czachor et al., 1972).

Based on the image analysis results (Table 3), the steel for MHR #1 (bar and friction unit) and MHR #2 bar were expected to have a relatively higher corrosion rate. The high-volume fraction of the pearlite phase is indicative of a high amount of cementite due to the lamellar structure of pearlite. This will enable galvanic corrosion, leading to an elevated corrosion rate. The corrosion resistance of the friction unit steel for MHR #1 is further exacerbated by the comparatively higher fraction of inclusions.

Accelerated corrosion testing

In the absence of long-term data on the susceptibility to corrosion of the new generation of MHR, accelerated corrosion tests can provide some preliminary insight into their behaviour. Accelerated corrosion tests have been used in the past to highlight variations in the performance of expandable rockbolts (Hadjigeorgiou et al., 2020), friction rock stabilisers (Hadjigeorgiou et al., 2023), and welded mesh and straps (Hadjigeorgiou et al., 2024). These results demonstrated that the chemical composition of the steel chosen by a given supplier could have a significant impact on corrosion performance when exposed to aggressive environments. Given that MHR do not employ resin it is reasonable to anticipate that they would also be susceptible to corrosion.

Investigating electrochemical properties associated with the corrosion reaction of rockbolt steel can assist in characterising the in situ corrosion performance in a specific corrosive environment. The electrochemical properties are obtained from a plurality of accelerated corrosion tests, of which the results are considered indicative of the actual corrosion performance. Nevertheless, accelerated corrosion testing can provide fundamental corrosion properties that are useful in various phases of the ground support design process, especially when corrosion is one of the concerns. Moreover, accelerated corrosion testing is generally faster than the conventional immersion testing of the ground support elements.

Accelerated corrosion tests on steel materials used for MHR were performed to characterise the corrosion performance of each rockbolt steel. For the MHR, the experiment focuses on the main components, the steel tendon and the friction unit, as both components play essential roles in establishing the reinforcement

Table 4

Chemical composition of the synthetic mine water as the lixiviate for the accelerated corrosion test (Hadjigeorgiou et al., 2020)

Chemical compound	Formula	g/L
Chemical compound	Formula	g/L
Magnesium sulphate heptahydrate	$MgSO_4.7H_2O$	31.44
Calcium sulphate dihydrate	$CaSO_4.2H_2O$	1.76
Ferrous sulphate heptahydrate	$FeSO_4.7H_2O$	1.24
Aluminum sulphate octa decahydrate	$Al_2(SO_4)_3.18H_2O$	10.49
Zinc sulphate heptahydrate	$ZnSO_4.7H_2O$	3.87
Sodium sulphate anhydrite	Na_2SO_4	0.12
Sodium chloride	NaCl	0.41

action of the rockbolt. The non-galvanised (black) rockbolts were obtained from different suppliers. The same lixiviate, or synthetic mine water used in Hadjigeorgiou et al. (2020), Hadjigeorgiou et al. (2023), and Hadjigeorgiou et al. (2024) was employed as the electrolyte in the experiment. It was prepared by dissolving chemical compounds (salts) listed in Table 4 in de-ionised (DI) water. The final pH of the lixiviate was adjusted to 2.7 using diluted sulphuric acid (H_2SO_4). Based on the low pH and high concentration of aqueous chemical species, the lixiviate represents an aggressive mine environment.

Electrochemical techniques for accelerated corrosion test and analysis

Each rockbolt steel sample was subjected to accelerated corrosion tests comprising three (3) electrochemical techniques: open-circuit potential (OCP), linear polarisation resistance (LPR), and potentiodynamic polarisation. The sequence, potential window, and scan rate for the electrochemical techniques are provided in Figure 5. During the OCP measurement, no current was allowed to pass between the counter and working electrodes and the potential was measured as a function of time until the steel was equilibrated with the electrolyte. This is followed by the LPR technique, following the procedure outlined in ASTM G59 – 97 using the conditions noted in Figure 5. With a small potential window about the E_{OCP}, the LPR is considered a non-destructive technique, thus allowing further techniques to be performed in sequence for the investigation. Lastly, the potentiodynamic anodic polarisation technique was carried out by adapting the procedure in ASTM G5 – 14, as noted in Figure 5.

Polarisation resistance (R_p) resulting from the LPR measurement will be used to determine the corrosion current density by using the equation proposed by Stern and Geary (1957):

$$i_{corr} = \frac{\beta_a \beta_c}{2.303\, R_p(\beta_a + \beta_c)} \quad [1]$$

where; βa: anodic Tafel slope; β_c: cathodic Tafel slope; R_p: polarisation resistance; i_{corr}: corrosion current density. By using Faraday's law, the corrosion rate (r), in mm/year, can be calculated from the corrosion current density (i_{corr}) (Dean Jr. et al., 1971):

$$r = 0.00327\, \frac{i_{corr}}{\rho}\, EW \quad [2]$$

where; ρ: density of sample; *EW*: equivalent weight. The equivalent weight, which is perceived as the mass of metal/alloy in grams that will be oxidised as a result of one Faraday (96,489 C) electric charge, is calculated in accordance with ASTM G102 – 89.

Sample preparation and experimental set-up

For the accelerated corrosion test, three (3) replicates were prepared from the steel material of each sample/rockbolt component to ensure the repeatability of the result. The procedure for preparing the replicates is summarised in Figure 6. Generally, the preparation involves soldering a Cu-wire to the replicate and grinding the surface of interest to a 600-grit final surface using SiC paper. Due to the small size of the bar replicate and irregular edges resulting from sectioning, an epoxy resin encapsulation is used to protect against localised corrosion/pitting. Moreover, the order of soldering and grinding to the 600-grit final surface of the bar component also differs from that of the friction unit component. The last step of the replicate preparation is masking the area of interest using Amercoat 90HSTM epoxy with three (3) coating layers. Once the coating had been fully cured, a high-resolution optical image was taken, and the area of the surface was determined by using ImageJ software.

The experimental setup for the accelerated corrosion test is shown in Figure 7. A three-electrode setup similar to that of Hadjigeorgiou et al. (2020), Hadjigeorgiou et al. (2023), and Hadjigeorgiou et al. (2024) was applied in this work. A three-electrode cell consisting of a working, counter, and reference electrode was used. The working electrode is the replicate of the rockbolt steel, while the counter electrode is a fine platinum mesh. An Ag/AgCl electrode filled with 3M KCl was used as the reference electrode that was calibrated before each test. Each test was carried out in a minimum of 500 ml lixiviate and purged with Argon gas at around 150 ml/min for 60 minutes to ensure complete deaeration before the electrochemical techniques were initiated. The temperature of the lixiviate is kept at 30oC during the purging and the accelerated corrosion test using a water bath.

Corrosion morphology and electrochemical properties of rockbolt steel

Based on the electrochemical techniques employed, electrochemical properties obtained include the open-circuit potential (E_{OCP}),

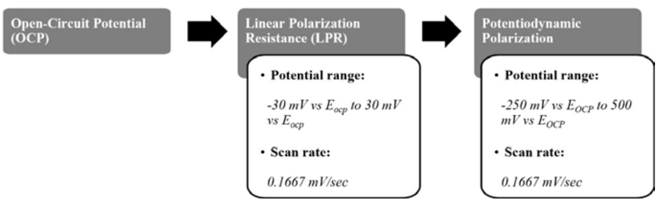

Figure 5—Sequences, the potential range of applied bias, and scan rate for electrochemical techniques for accelerated corrosion test

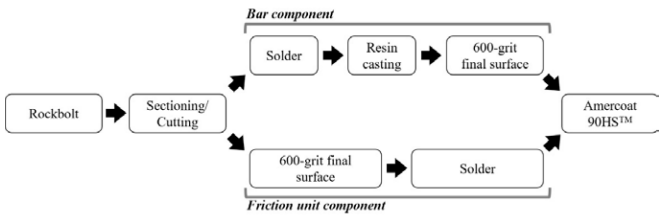

Figure 6—Schematic diagram of the procedure to prepare replicates for the accelerated corrosion test

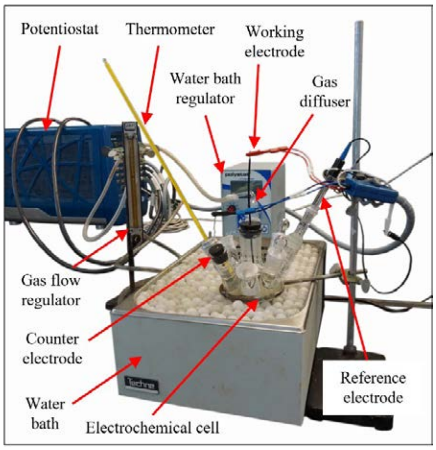

Figure 7—Experimental setup for the accelerated corrosion test

polarisation resistance (R_p), Tafel slopes, corrosion potential (E_{corr}), and corrosion current density ($i_{corr\ PP}$). Measured potentials are converted to the saturated calomel electrode (SCE) scale. Further analysis was performed to determine the corrosion rate from linear polarisation resistance (LPR) and potentiodynamic polarisation results. A high-resolution optical image was taken right after the acceleration corrosion test to examine the surface condition of every replicate.

Corrosion morphology

A comparison of the sample surface before and after the accelerated corrosion tests is summarised in Figures 8 and 9. Based on visual observations, the corrosion morphology of all samples was relatively uniform. The morphology is characterised as general corrosion with the formation of an oxide layer. Pitting or crevice corrosion was not found on the sample surface.

Open-circuit potential (OCP) measurements

In the OCP test, the working electrode is unbiased and equilibrates with the solution over time. The open-circuit potential was measured after the working electrode had equilibrated for 60 minutes. The open-circuit potentials for all samples range from -0.673 V to -0.648 V vs SCE (-0.432 V to -0.407 V vs SHE). In this electrochemical system, based on the open-circuit potential of which the magnitude is situated between the most feasible oxidation and reduction reactions (Bard et al., 2022), the corrosion reactions on all rockbolt samples involved the dissolution of iron as the anodic reaction (E_{red}^o = -0.44 V vs SHE) and the hydrogen evolution reaction as the cathodic reaction (E_{red}^o = 0.00 V vs SHE).

The measurement of open-circuit potential for all samples over the first 60 minutes of immersion is shown in Figure 10. The MHR #1 bar/tendon steel is the most active steel with the lowest open-circuit potential. In contrast, the friction unit steel of the MHR #2 has the most noble open-circuit potential. The difference in the open-circuit potential between those two steel materials is 35 mV. It is also interesting to note that the steel used for both bar components is more active than the steel used for both friction unit components of the MHR. A comparison between the components of both products shows that the steel material for MHR #1 is more active than that of MHR #2.

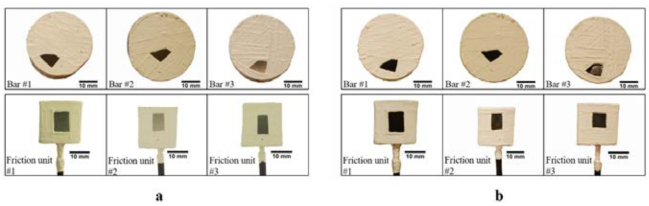

Figure 8—Corrosion morphology on MHR #1 sample: a. Before accelerated corrosion test b. After the test

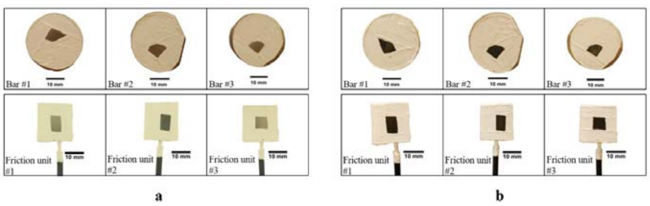

Figure 9—Corrosion morphology on MHR #2 sample: a. Before accelerated corrosion test b. After the test

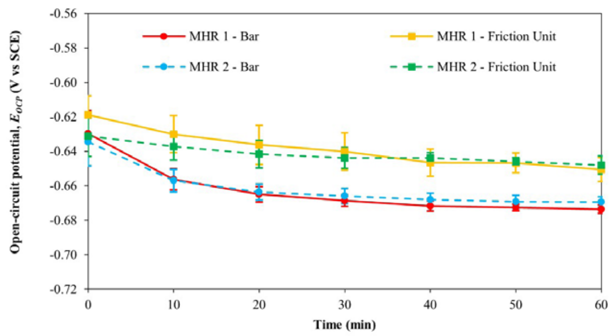

Figure 10—Open-circuit potential measurements of steels from two MHRs

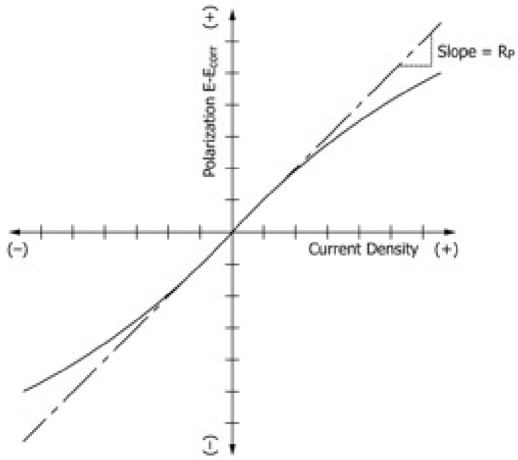

Figure 11—Hypothetical linear polarisation plot and measurement of polarisation (ASTM G3 – 14)

Linear Polarization Resistance (LPR)

The polarization resistance was measured as the slope of the potential–current density behaviour of the sample within an apparent linear region about the origin (Figure 11). The polarization plot was established by applying a small cathodic and anodic bias (± 30 mV) about the open-circuit potential at a constant sweep rate while recording the current density response of the working electrode. As the polarization resistance is inversely proportional to the corrosion rate, the more current generated due to a small magnitude of polarisation, the higher the corrosion rate of the metal/alloy will be. The linear polarisation plot resulting from the LPR measurement of all rockbolt samples is shown in Figures 12 and 13.

The corrosion rate of rockbolt samples estimated from the LPR results is summarised in Table 5. The results in Figure 12 and Figure 13 illustrate three separate runs on each of the rockbolt specimens and demonstrate good reproducibility between samples. It should be noted that the corrosion rate calculation requires Tafel slopes to be measured during the potentiodynamic polarisation test. Based on the LPR measurement, the corrosion rate of the bar components of both MHR is statistically equivalent. The corrosion rate of the MHR #1 is substantially greater than for the friction unit of MHR #2. For the MHR #1, the friction unit had a higher corrosion rate compared to the bar, while the reverse trend was observed in MHR #2. Overall, the steel for the friction unit component of MHR #1 has the highest corrosion rate for all the materials tested by LPR, and the lowest corrosion rate was observed for the friction unit of MHR #2.

Anodic potentiodynamic polarisation (AP)

In the potentiodynamic polarisation technique, the current response of the rockbolt sample was recorded as the electrode potential was polarised both cathodically and anodically. The magnitude of the applied voltage is significantly higher than that of the LPR technique, and the measurement is initiated by a cathodic polarisation followed by an anodic polarisation. A hypothetical potential-current density behaviour of metal, along with the interpretation of electrochemical properties resulting from the potentiodynamic polarisation technique, is shown in Figure 14. The corrosion current density and the corrosion potential are determined by the intersection of the extended Tafel behaviour observed at a relatively higher overpotential. The slopes of these two linear regimes defined as the anodic Tafel slope (βa) and cathodic Tafel slope (βc), which characterise the kinetics of the metal dissolution reaction and the hydrogen evolution reaction, respectively.

The polarisation plots recorded in the potentiodynamic technique for rockbolt samples are presented in Figures 16 and 17. The plots indicate a good reproducibility of the potential - current behaviour among steel replicates of the same bolt component. Compared to the hypothetical polarisation plot in Figure 14, the polarisation plots of the rockbolt steel are all unsymmetrical about the corrosion potential as the axis of symmetry. This indicates that within the potential window applied for the potentiodynamic polarisation technique, the redox reactions and the rate of reactions occurring at a higher anodic and cathodic overpotential are not the same. The cathodic current is produced from the hydrogen evolution reaction, whereas the anodic current is most likely associated with the Fe dissolving into Fe^{2+}.

The results of potentiodynamic polarisation measurements are presented in Table 6. The variance of results among replicates of the same rockbolt component is statistically negligible. Regarding the corrosion potential, the steel for the MHR #1 bar is the most active, while the most noble steel is of the friction unit for the MHR #2. Using this electrochemical technique, the corrosion rate of the bar of MHR #1 is greater than MHR #2. Similarly, the corrosion rate for the friction unit of MHR #1 is greater than that of the friction unit of MHR #2. The highest corrosion rate was observed on the steel for the MHR #1 friction unit. It is interesting to note that the estimated corrosion rates of the friction unit steels are slightly higher than the bar steels on the same product. A very high cathodic Tafel slope, which was also observed in Hadjigeorgiou et al.

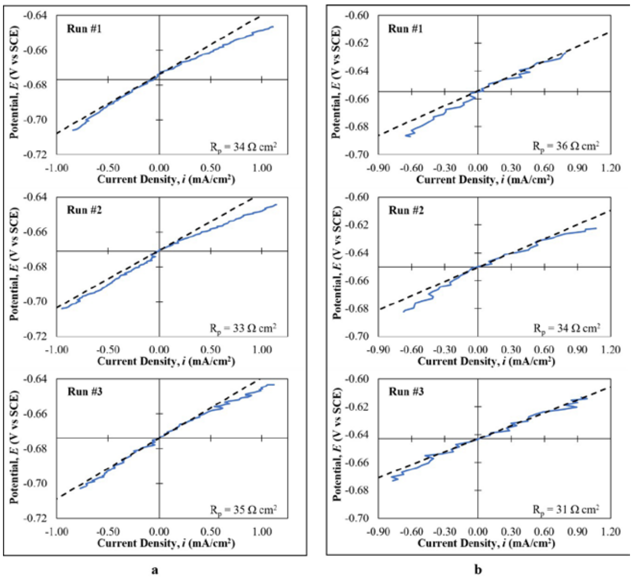

Figure 12—Linear polarisation resistance results for MHR #1: a. Bar steel b. Friction unit steel

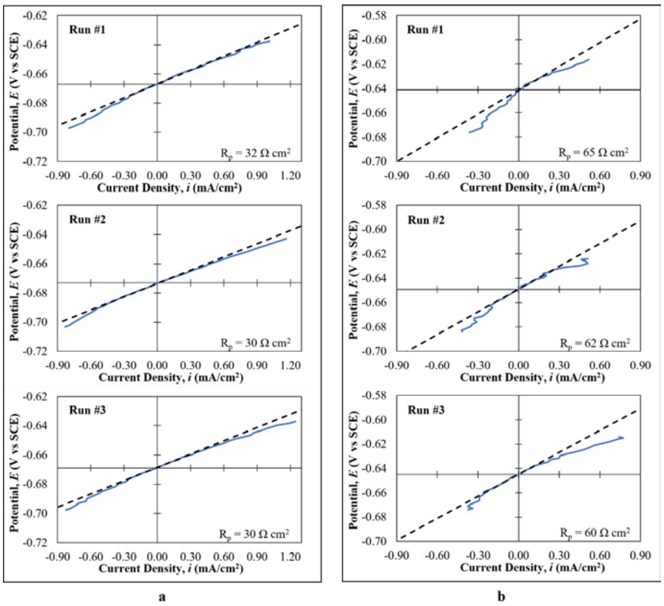

Figure 13—Linear polarisation resistance results of MHR #2: a. Bar steel b. Friction unit steel

Rockbolt	Component	Rp (Ω cm²)	$i_{corr,Rp}$ (mA cm^{-2})	r_{Rp} (mm yr^{-1})
Table 5 **Summary of results and analyses of LPR measurement for all rockbolt samples**				
MHR #1	Bar	34.0 ± 1.0	0.95 ± 0.04	11.12 ± 0.48
	Friction unit	33.7 ± 2.5	1.21 ± 0.08	14.24 ± 0.92
MHR #2	Bar	30.7 ± 1.2	1.03 ± 0.03	12.08 ± 0.31
	Friction unit	62.3 ± 2.5	0.56 ± 0.02	6.56 ± 0.27

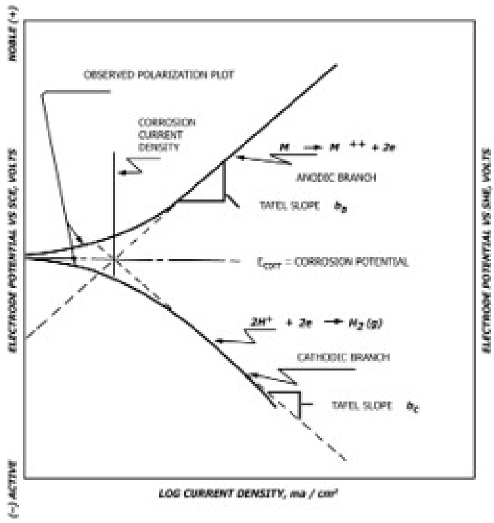

Figure 14—Hypothetical cathodic and anodic Tafel polarisation plot (ASTM G3 - 14)

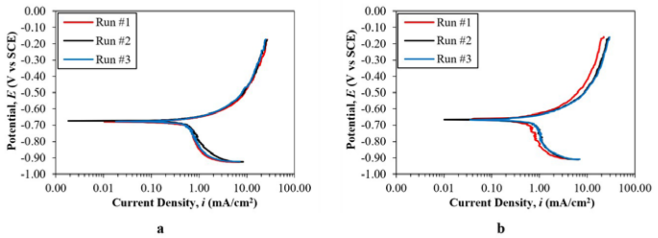

Figure 15—Potentiodynamic polarisation plot for MHR #1: a. Bar b. Friction unit

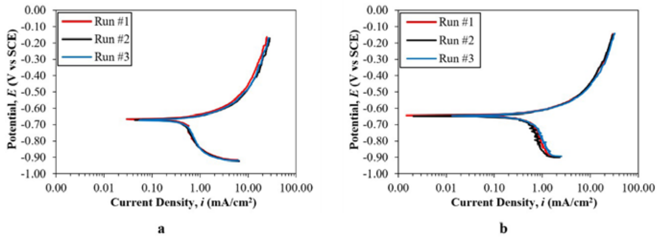

Figure 16—Potentiodynamic polarisation plot for MHR #2: a. Bar b. Friction unit

(2020), Hadjigeorgiou et al. (2023), and Hadjigeorgiou et al. (2024a, 2024b) was measured in this experiment. The high cathodic Tafel slope is a characteristic of a mixed electrochemical mechanism on the electrode surface and indicates that the cathodic reaction is not purely a hydrogen evolution reaction (HER).

Discussion

The potential and corrosion rates resulting from the accelerated corrosion test are summarised in Table 7. The open-circuit potential of the same rockbolt sample agrees well with the corrosion potential measured during potentiodynamic polarisation measurements. The slight variance in both open-circuit and corrosion potential indicates that all rockbolt steels are similar in thermodynamic behaviour.

Comparing the corrosion rate obtained from LPR and potentiodynamic measurements for the bar components, LPR measurements showed a similar trend in corrosion rate, with the exception of the bar component of MHR #2. A slightly higher corrosion rate was statistically measured for all of the LPR measurements compared to AP measurements. The corrosion rate from AP may appear lower because they are more influenced by factors such as the formation of passive or barrier type films and the rate of accumulation of metal ions near the surface because of the higher anodic potentials reached during the test. The corrosion rate of the friction unit steel for MHR #1 was substantially higher than all other components, regardless of the technique employed.

The extent of variation in the electrochemical properties in Table 7 is most likely attributable to the variation in the exact chemical composition of each rockbolt steel. By using mixed potential theory to explain the variation in the open-circuit potential and the corrosion potential, the most active (lowest) potential of the MHR #1 bar steel can be associated with the highest total mass fraction of alloying elements that are more active than Fe such as Mn and Si. The presence of alloying elements such as C, S, Cu, Ni, Mo, Co, and P from atomic or microscale perspectives can potentially lead to more noble open-circuit or corrosion potentials. However, quantifying how these elements influence the E_{OCP} and E_{CORR} is complex. This is due to the formation of the chemical compounds, i.e., carbides and sulphide inclusions, that also play essential roles in the magnitude of the potentials, not only due to the presence of substitutional alloying elements. The same case was encountered while investigating the relationship between the chemical compositions and the corrosion rate. Nevertheless, the magnitude of the corrosion rate may be attributed to two electrochemical mechanisms. The first is the formation of stable, protective oxide film, most likely contributed by Si, Cu, Ni, Cr, Mo, Al, Co, Ti, and Nb. The underlying assumption for this mechanism is that one or more of these elements are partitioned into or stabilise the resultant oxide film; thus, the corrosion rate is reduced. The second is micro-galvanic corrosion due to chemical compounds formed by C and S, leading to an elevated corrosion rate.

When carbon is added to the steel within the hypoeutectoid composition, where the heat treatment process only involves heating the steel to the upper critical temperature and then cooling it at a slow rate to room temperature, a large portion of the C content will react with Fe to form cementite and is precipitated in the form of pearlite. Comparing the corrosion rate based on the

Table 6

Summary of electrochemical properties of steel samples obtained from the potentiodynamic polarisation measurements

Rockbolt	Component	E_{corr} (V vs SCE)	$i_{corr,PP}$ (mA cm^{-2})	r_{PP} (mm yr^{-1})	βa (mV dec^{-1})	βc (mV dec^{-1})
MHR #1	Bar	-0.678 ± 0.003	0.533 ± 0.023	6.26 ± 0.27	86 ± 4	516 ± 20
	Friction unit	-0.665 ± 0.003	0.653 ± 0.098	7.72 ± 1.16	115 ± 4	488 ± 7
MHR #2	Bar	-0.668 ± 0.003	0.458 ± 0.014	5.40 ± 0.17	82 ± 2	598 ± 2
	Friction unit	-0.645 ± 0.001	0.473 ± 0.042	5.53 ± 0.49	96 ± 1	490 ± 4

Table 7

Comparison of potentials and corrosion rates estimated from different electrochemical techniques

Rockbolt	Component	E_{OCP} (V vs SCE)	E_{corr} (V vs SCE)	r_{Rp} (mm yr^{-1})	r_{PP} (mm yr^{-1})
MHR #1	Bar	-0.673 ± 0.002	-0.678 ± 0.003	11.12 ± 0.48	6.26 ± 0.27
	Friction unit	-0.651 ± 0.007	-0.665 ± 0.003	14.24 ± 0.92	7.72 ± 1.16
MHR #2	Bar	-0.669 ± 0.003	-0.668 ± 0.003	12.08 ± 0.31	5.40 ± 0.17
	Friction unit	-0.648 ± 0.005	-0.645 ± 0.001	6.56 ± 0.27	5.53 ± 0.49

LPR technique and the volume fraction of pearlite shows that the steel with a high pearlite volume fraction (bar and friction unit of MHR #1 and bar of MHR #2) has a higher corrosion rate (r_{LPR}). With the micro-galvanic coupling between the pearlite and ferrite phases, where the carbide phase acts as a cathodic site, the anodic dissolution of the boundary between both phases and/or the ferrite phase is accelerated, leading to a higher corrosion rate. An interesting condition was seen on the friction unit steel of MHR #1, indicating a significant influence of the presence of inclusions on the corrosion performance. Even though the steel does not have the highest volume fraction of the pearlite phase, the highest corrosion rate is most likely attributed to the significantly high-volume fraction of inclusions.

The long-term behaviour of MHR may be affected by the overall and relative corrosion rates of their various components. On MHR #1, the corrosion rate of the steel for the bar is slightly lower than that of the friction unit. The opposite condition is identified on MHR # 2 in LPR tests. The comparison also shows that the corrosion rates of the bar components from different suppliers are similar. This may indicate that the reduction of the ultimate capacity of the bar between both MHR will not differ significantly. On the other hand, a significant variation in the corrosion rate between the friction unit components is observed. For an MHR product of which the friction unit will also sustain a relatively greater portion of the axial load, a significant loss in the cross-sectional area in extreme conditions may also lead to a loss of capacity. A heavily corroded friction unit will negatively impact the anchoring performance of the bolt to achieve its designed ultimate capacity.

Conclusion

Mechanical hybrid rockbolts are a relatively recent addition to the reinforcement toolbox to support underground excavations in rock. A major impetus for their use is that the installation process improves the rockbolt resilience to hole closures and avoids issues associated with the use of resin. Recent experimental data, as reported in Carlton et al. (2013) and Knox and Hadjigeorgiou (2024), demonstrated that the higher yielding capacity of MHR would also make them suitable for squeezing and rock burst prone conditions.

A potential limitation of MHR is their long-term performance in corrosive environments. Currently there are no empirical data capturing the long-term performance of MHR in corrosive environments. This is a major shortcoming to assess the consequences of using MHR. This paper is part of a multi-year research project on MHR aiming to quantify their mechanical behaviour and susceptibility to corrosion. This involves mechanical quasi-static and impact tests, accelerated corrosion tests, long-term laboratory immersion tests, and field trials in a selected mine site.

An investigation of the corrosion performance of the steel used in two types of MHR has been conducted to understand the corrosion resistance between rockbolt components and the variability among the two products. Accelerated corrosion techniques, where each component is uniformly exposed to the same corrosive synthetic mine water, revealed that each MHR had different corrosion resistance.

Overall MHR #2 performed better than MHR #1 in this phase of the investigation that included material testing and accelerated corrosion. The results are more instructive when considering separately the performance of the rebar/bar steel the friction unit steel.

In both MHR, the rebar/bar steel had a higher hardness than the friction unit steel on the same product. This is attributed to the higher concentration of C, Mn, Si, Cr, and V than the friction unit component for the same MHR product. These elements are associated with increased strength through either precipitation of carbides, or interstitial and substitutional solid solution hardening. A significant variation, however, was observed between the tensile strength of the bar for MHR #2 (721 ± 14 MPa) and MHR #1 (655 ± 24 MPa).

MHR #1 is more susceptible to corrosion compared to MHR #2. Although the steel bar from both products has similar corrosion resistance, a significant variation was observed in the friction unit components.

The corrosion rate using linear polarisation resistance and potentiodynamic polarisation measurements for the friction unit steel for MHR #1 was substantially higher than that observed for MHR #2. This was explained by the chemical composition of the steel. A contributing factor to the higher corrosion rate for the friction unit steel of MHR #1, is the significantly high-volume fraction of inclusion determined by image analysis of SEM images of the rockbolt steel (based on ASTM E1245-03).

For an MHR of which the friction unit will also sustain a relatively greater portion of the axial load, a significant loss in the cross-sectional area in extreme conditions may also lead to a loss of capacity. A heavily corroded friction unit will negatively impact the anchoring performance of the bolt to achieve its designed ultimate capacity. This is consistent with previous work by Dorion and Hadjigeorgiou (2014), whereby the residual capacity of friction rock stabilisers was shown to be a function of the design capacity and the corrosion rate.

A further practical implication is that there can be significant variation in the corrosion resistance between different MHR products. This underscores the need to establish strict criteria on corrosion performance of these new MHRs. This can have significant implications in selecting a particular MHR for long-term applications.

Acknowledgements

The authors would like to acknowledge the financial support of Vale Base Metals and the Natural Science and Engineering Research Council of Canada. The authors would also like to acknowledge the collaboration from Sandvik and Epiroc who provided the rockbolt samples used in these investigations.

References

Andrews, P. 2019. Ground support selection rationale: a Gold Fields perspective. Australian Centre for Geomechanics. 15–28 p.

ASTM A1011/A1011M-23. 2023. Standard Specification for Steel, Sheet and Strip, Hot-Rolled, Carbon, Structural, High-Strength Low-Alloy, High-Strength Low-Alloy with Improved Formability, and Ultra-High Strength. West Conshohocken (PA): ASTM International, 100 Barr Harbor Drive, PO Box C700, West Conshohocken, PA 19428-2959. US.

ASTM E1245-03. 2023. Standard Practice for Determining the Inclusion or Second-Phase Constituent Content of Metals by Automatic Image Analysis. West Conshohocken (PA): ASTM International, 100 Barr Harbor Drive, PO Box C700, West Conshohocken, PA 19428-2959. US.

ASTM E18-22. 2022. Standard test methods for Rockwell hardness of metallic materials. West Conshohocken (PA): ASTM International, 100 Barr Harbor Drive, PO Box C700, West Conshohocken, PA 19428-2959. US.

ASTM E1019-11. 2011. Standard Test Methods for Determination of Carbon, Sulfur, Nitrogen, and Oxygen in Steel, Iron, Nickel, and Cobalt Alloys by Various Combustion and Fusion Techniques. West Conshohocken (PA): ASTM International, 100 Barr Harbor Drive, PO Box C700, West Conshohocken, PA 19428-2959. US.

ASTM E1479-16. 2016. Standard Practice for Describing and Specifying Inductively Coupled Plasma Atomic Emission Spectrometers. West Conshohocken (PA): ASTM International, 100 Barr Harbor Drive, PO Box C700, West Conshohocken, PA 19428-2959. US.

ASTM F432-19. 2019. Standard Specification for Roof and Rock Bolts and Accessories.

ASTM G3 - 14. 2019. Standard Practice for Conventions Applicable to Electrochemical Measurements in Corrosion Testing. West Conshohocken (PA): ASTM International, 100 Barr Harbor Drive, PO Box C700, West Conshohocken, PA 19428-2959. US.

ASTM G5 - 14. 2021. Standard Reference Test Method for Making Potentiodynamic Anodic Polarization Measurements. West Conshohocken (PA): ASTM International, 100 Barr Harbor Drive, PO Box C700, West Conshohocken, PA 19428-2959. US.

ASTM G59 - 97. 2020. Standard Test Method for Conducting Potentiodynamic Polarization Resistance Measurements. West Conshohocken (PA): ASTM International, 100 Barr Harbor Drive, PO Box C700, West Conshohocken, PA 19428-2959. US.

ASTM G102 - 89. 2015. Standard Practice for Calculation of Corrosion Rates and Related Information from Electrochemical Measurements. West Conshohocken (PA): ASTM International, 100 Barr Harbor Drive, PO Box C700, West Conshohocken, PA 19428-2959. US.

Bard, A.J., Faulkner, L.R., White, H.S. 2022. Electrochemical Methods Fundamentals and Applications. 3rd ed. John Wiley & Sons, Ltd: Hoboken, NJ.

Carlton, R., Darlington, B., Mikula, P. 2013. In situ dynamic drop testing of the MD bolt at Mt Charlotte Gold Mine. Australian Centre for Geomechanics. pp. 207–219.

Clover, D., Kinsella, B., Pejcic, B., De Marco, R. 2005. The Influence of Microstructure on the Corrosion Rate of Various Carbon Steels. Journal of Applied Electrochemistry vol. 35 (no. 2): pp. 139–149.

Craig, P., Serkan, S., Hagan, P., Hebblewhite, B., Vandermaat, A., Crosky, A., Elias, E. 2016. Investigations into the corrosive environments contributing to premature failure of Australian coal mine rock bolts. *International Journal of Mining Science and Technology* vol. 26, no. 1: pp. 59–64.

Darlington, B., Rataj, M., Roach, W. 2019. A new method to evaluate dynamic bolts and the development of a new dynamic rock bolt. *The Southern Africa Institute of Mining and Metallurgy*. Proceedings of the Ninth International Conference on Deep and High Stress Mining 2019: pp. 205–216.

Dean Jr., S.W., France Jr., W.D., Ketcham, S.J. 1971. Electrochemical methods. In W.H. Ailor (ed.), *Handbook on Corrosion Testing and Evaluation*, pp. 173–174. New York.

Dorion, J.F., Hadjigeorgiou, J. 2014. Corrosion considerations in the design and operation of rock support systems. *Mining Technology* vol. 123, no. 2, pp. 59–68.

Dorion, J.F., Hadjigeorgiou, J. 2020. Microbiologically Influenced Corrosion (MIC) of ground support. *Geotechnical and Geological Engineering* vol. 38, no. 1, pp. 375–387.

Epiroc. 2025. 'Vulcan Bolt' Online at https://www.epiroc.com/en-ba/products/rock-drilling-tools/ground-support/energy-absorbing-rockbolts/vulcan-bolt (accessed 13 January 2025).

Evans, D.W. 2022. Data cross validation for a newly commissioned dynamic drop test facility. The Australasian Institute of Mining and Metallurgy: Melbourne. pp. 320–328 .

Hadjigeorgiou, J., Dorion, J.F., Ghali, E. 2008. Support System Performance under Different Corrosion Conditions. *Journal of the Southern African Institute of Mining and Metallurgy* vol. 108, pp. 359–365.

Hadjigeorgiou, J., Savguira, Y., Thorpe, S.J. 2020. Impact of steel properties on the corrosion of expandable rock bolts. *Rock Mechanics and Rock Engineering* vol. 53, no.2, 705–721.

Hadjigeorgiou J., S.J. Thorpe and K.M. Cole 2023. Quality Assurance Considerations for Friction Rock Stabilizers. *Mining Technology (TIMM A)*. vol. 132, no. 1, pp. 17–29.

Hadjigeorgiou, J., Thorpe, S.J., Storimans, E., Agrensa, F.D. 2024. Impact of steel properties on the susceptibility to corrosion of weld mesh and mesh straps. *The Journal of the Southern African Institute of Mining and Metallurgy* vol 124, no. 9, pp. 517–526.

Hayden, S.C., Chisholm, C., Eichmann, S.L., Grudt, R., Frankel, G.S., Hanna, B., Headrick, T., Jungjohann, K.L. 2022. Genesis of Nanogalvanic Corrosion Revealed in Pearlitic Steel. Nano Letters vol. 22, no. 17, pp. 7087–7093.

ISO 18265:2013. 2013. Metallic materials - Conversion of hardness values. Geneva: International Organization for Standardization (ISO).

Janik-Czachor, M., Szummer, A., Szklarska-Smialowska, Z. 1972. Effect of Sulphur and Manganese on Nucleation of Corrosion Pits in Iron. *British Corrosion Journal* vol. 7, no. 2, pp. 90–93.

Kadowaki, M., Muto, I., Takahashi, K., Doi, T., Masuda, H., Katayama, H., Kawano, K., Sugawara, Y., Hara, N. 2019. Anodic Polarization Characteristics and Electrochemical Properties of Fe3C in Chloride Solutions. *Journal of The Electrochemical Society* vol. 166, no, 12, C345–C351.

Knox & Hadjigeorgiou 2024a. Behaviour of Yielding Mechanical Hybrid Rockbolts under Complex Loading Conditions. International *Journal of Rock Mechanics and Mining Sciences* vol. 182.

Knox & Hadjigeorgiou 2024b. Direct impact load tests on mechanical hybrid rockbolts. *Australian Centre for Geomechanics: Montreal, Canada*. pp. 467–478.

Knox, G., Hadjigeorgiou, J. 2023. Performance in Shear of Mechanical Hybrid Rockbolts. Australian Centre for Geomechanics, Perth. pp. 495–506.

Sandvik. 2025. 'MD/MDX Bolt' Online at https://www.rocktechnology.sandvik/en/products/ground-support/bolts-and-cables/friction-bolts/md--mdx-bolt/ (accessed 13 January 2025).

Stern, M., Geary, A.L. 1957. Electrochemical polarization: a theoretical analysis of polarization curves. *Journal Electrochemical Society* vol. 104, no. 1, pp. 56–63.

Vallati, O., Darlington, B., Sandberg, L. 2022. Dynamic drop testing of Sandvik's D47 and D39 MDX bolts at the Swerim's testing facility. *The Australasian Institute of Mining and Metallurgy: Melbourne*. pp. 428–440. ◆

YOUNG PROFESSIONALS COUNCIL

SAIMM
THE SOUTHERN AFRICAN INSTITUTE OF MINING AND METALLURGY

7TH YOUNG PROFESSIONALS CONFERENCE

29-30 SEPTEMBER 2026
MINTEK, RANDBURG, JOHANNESBURG

ECSA and SACNASP Validated CPD ActivityCredits = 0.1 per hour attended

The role of youth and young professionals in Future Proofing African Mining, Today

The conference promises to be an engaging and informative event that will explore the latest trends, ideas, and innovations in the minerals industry. This conference offers young professionals the opportunity to network with peers and industry experts, establish professional relationships, and collaborate on future projects. A conference dedicated to young professionals emphasises the importance of empowering young professionals to lead the way in driving innovation and sustainability in the South African minerals industry.

OBJECTIVES

- During the conference, attendees can expect to participate in engaging sessions, informative talks, and interactive workshops covering a broad range of topics. These sessions will explore innovative technologies, sustainable mining practices, and the role of young professionals in driving positive change in the industry.
- In addition to the informative sessions, there will be ample opportunities to network with peers and industry experts, share ideas, and collaborate on projects. The conference will provide a platform for attendees to showcase their work, gain feedback, and receive recognition for their contributions.
- To promote diversity and inclusion in the mining industry by creating an environment that supports and celebrates individuals from all backgrounds.

Overall, the conference is a must-attend event for young professionals in the minerals industry. Whether you are an early-career professional or an experienced industry expert, this conference is an excellent opportunity to learn, network, and contribute to the future of the minerals industry in South Africa.

Key Dates:

4 May 2026 - Submission of abstracts

22 June 2026 - Submission of papers

29-30 September 2026 - Conference

FOR FURTHER INFORMATION, CONTACT:

Gugu Charlie,
Conferences and
Events Coordinator

E-mail: gugu@saimm.co.za
Tel: +27 11 538 0238
Web: www.saimm.co.za

NATIONAL & INTERNATIONAL ACTIVITIES

2026

7-11 September 2026 — Electra Mining Africa 2026
Expo Centre, Nasrec, Johannesburg
Contact: Gugu Charlie
Contact: Camielah Jardine
Tel: 011 538-0237
Website: http://www.saimm.co.za

21-24 September 2026 — XIX 2026 International Society for Mine Surveying Congress
Century City, Cape Town
Contact: Gugu Charlie
Tel: 011 538-0238
Website: http://www.saimm.co.za

29-30 September 2026 — 7TH Young Professionals Conference 2026
Mintek, Randburg, Johannesburg
Contact: Gugu Charlie
Tel: 011 538-0238
E-mail: gugu@saimm.co.za
Website: http://www.saimm.co.za

1-2 October 2026 — Mintek SCi- (Science Convention for Innovators in Science, Engineering and Technology)
Mintek, Randburg, Johannesburg
https://seismix2026.co.za/

5-9 October 2026 — The 21st International Symposium
Deep Seismic Profiling of the Continents and their Margin
Skukuza, Kruger National Park
Website: http://www.saimm.co.za

12-16 October 2026 — 19TH South African Geophysical Association Conference 2026
Lagoon Beach Hotel & Spa, Cape Town
Website: https://sagaconference.co.za/

18-22 October 2026 — IMPC 2026 XXXII International Mineral Processing Congress
Empowering a future-fit mineral processing industry
Cape Town, South Africa
Contact: Camielah Jardine
Tel: 011 538-0237
E-mail: camielah@saimm.co.za
Website: http://www.saimm.co.za

11-13 November 2026 — MineSafe 2026 Mine Health and Safety Conference
Engineering Health & Safety For Sustainable Future-Ready Mines
Gallagher Convention Centre, Johannesburg, South Africa
Contact: Gugu Charlie
Tel: 011 538-0238
E-mail: gugu@saimm.co.za
Website: http://www.saimm.co.za

15-18 November 2026 — Southern African Mine Water Conference 2026
Let's Connect
Glenburn Lodge, Muldersdrift
Contact: Gugu Charlie
Tel: 011 538-0238
E-mail: gugu@saimm.co.za
Website: http://www.saimm.co.za

GMG's 2026 Mid-Year Report
For more information
https://gmggroup.org/wp-content/uploads/2026/07/GMG-Mid-Year-Report-2026.pdf

28 February -3 March 2027 — MINEXCHANGE 2027
Denver, Colorado Colorado Convention Center
MINEXCHANGE 2027 SME Annual Conference and Expo

5-9 April 2027 — Hoist and Haul 2027
Century City, Cape Town
Contact: Gugu Charlie
Tel: 011 538-0238
E-mail: gugu@saimm.co.za
Website: http://www.saimm.co.za

Company affiliates

The following organizations have been admitted to the Institute as Company Affiliates

Agreenco Environmental Projects
OPTRON
Wekaba Engineering (Pty) Ltd
Jones & Wagener Pty Ltd
CYMOT (PTY) Ltd
Kelnir Projects (Pty) Ltd
DQS Pty Ltd
M84 Geotech Pty Ltd
Sulzer Pumps (South Africa) (Pty) Ltd
EKATO South Africa
CARBOCRAFT (PTY) LTD
Solenis
Pump and Abrasion Technologies (PTY) Ltd
CIGroup ACE Pty Ltd
Sebotka (Pty) Ltd
Mech-Industries (Pty) Ltd
Anton Paar Southern Africa
Trans-Caledon Tunnel Authority
acQuire Technology Solutions
EHL Consulting Engineers (Pty) Ltd
DDP Specialty Products South Africa (Pty) Ltd
Allied Furnace Consultants
Gravitas Minerals (Pty) Ltd
Mining Projection Concepts (Pty) Ltd
African Pegmatite
Ex Mente Technologies (Pty) Ltd
MLB Investments CC
Micromine Africa (Pty) Ltd
Ingwenya Mineral Processing
Maptek (Pty) Ltd
G H H Mining Machines (Pty) Ltd
OPTRON
Geobrugg Southern Africa (Pty) Ltd
Ivanhoe Mines SA
Weir Minerals Africa
Herrenknecht AG
Becker Mining (Pty) Ltd
Rosond (Pty) Ltd
Sound Mining Solution (Pty) Ltd
Roytec Global (Pty) Ltd
Caledonia Mining South Africa
Elbroc Mining Products (Pty) Ltd
Modular Mining Systems Africa (Pty) Ltd
Paterson & Cooke Consulting Engineers (Pty) Ltd
SENET (Pty) Ltd
Tomra (Pty) Ltd
Ukwazi Mining Solutions (Pty) Ltd
Arcus Gibb (Pty) Ltd
SRK Consulting SA (Pty) Ltd
ZUTARI (Pty) Ltd
Minerals Council of South Africa
Bluhm Burton Engineering Pty Ltd
Hatch (Pty) Ltd
Anglogold Ashanti Ltd
Digby Wells and Associates
AMIRA International Africa (Pty) Ltd
Malvern Panalytical (Pty) Ltd
MineRP Holding (Pty) Ltd
FLSmidth Minerals (Pty) Ltd
Glencore
Murray & Roberts Cementation (Pty) Ltd
Redpath Mining (South Africa) (Pty) Ltd
Sibanye Gold Limited
AECI Mining Chemicals, a division of AECI Mining Ltd
Exxaro Resources Limited
IMS Engineering (Pty) Ltd
Rustenburg Platinum Mines Limited - Union
Impala Platinum Holdings Limited
Mintek

Enaex Africa

Enaex Bright

Turn blasting data into operational intelligence.

FROM DATA TO BETTER BLASTING DECISIONS.
Greater visibility. Better control. Continuous optimisation.

Enaex Bright connects critical information across the blasting lifecycle, giving mining operations greater visibility from drilling and blast preparation through execution, monitoring and post blast analysis.

Through one connected digital ecosystem, Bright helps teams identify deviations, validate execution, analyse outcomes and continuously improve blasting performance.

ONE CONNECTED ECOSYSTEM

BRIGHT SCAN

Drilling and blasting quality assurance

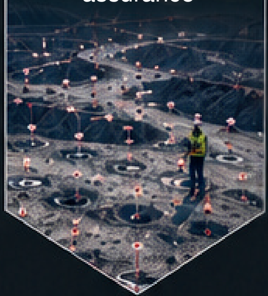

BRIGHT FLEET

Operational and fleet visibility

BRIGHT BLAST

Blast design and performance intelligence

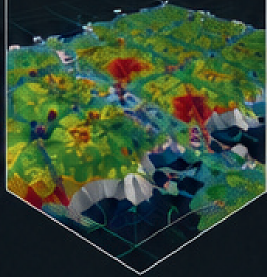

BRIGHT CARE

Environmental and blast impact monitoring

OPTOMISE YOUR BLASTING OPERATIONS TODAY!

011 911 3412

enaex@enaex.com